UNIVERSITEIT GENT

FACULTEIT WETENSCHAPPEN

NUCLEON PROPAGATION INDUCED BY ELECTROWEAK EXCITATION OF ATOMIC NUCLEI

Pascal Lava

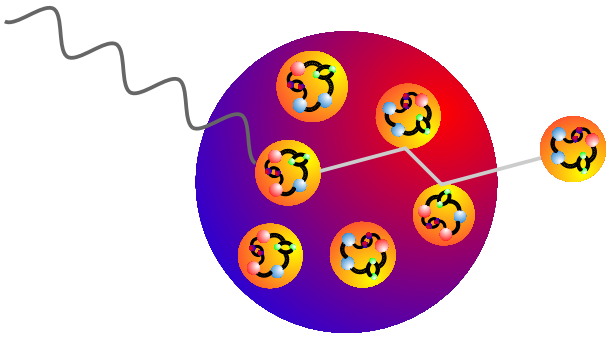

Promotor: Prof. Dr. Jan Ryckebusch

Proefschrift ingediend tot het behalen van de academische graad van
Doctor in de Wetenschappen: Natuurkunde

Universiteit Gent
Faculteit Wetenschappen
Vakgroep Subatomaire en Stralingsfysica
Academiejaar 2005-2006

In this house,
we obey the laws of thermodynamics.

H. Simpson

Dankwoord

Een voorwoord is traditioneel een dankwoord. De volgende personen zijn te belangrijk om met deze traditie te breken.
In de eerste plaats, bedankt Jan, om me vier jaar geleden het nodige vertrouwen te schenken en me gedurende deze periode van de noodzakelijke deskundige begeleiding te voorzien. U was een fijne promotor. Bedankt Natalie, om me mee te sleuren in de boeiende wereld van neutrino's en voor de vele hulp onderweg. Tevens dank voor de toffe discussies en INW-binnenste buiten. U was een fijne collega. Thank you, Cristina. You were of crucial importance for the achievements presented in this thesis. Thanks for the nice atmosphere and your eternal smile. Thanks Jose and Steffen, for the nice collaborations throughout these four years.
Bedankt Dimitri, om me een uiterst handige code na te laten. Bedankt Tim, om altijd mijn koffie leeg te drinken. Jouw fysisch doorzicht en humor werkten vaak verhelderend. U was een fijne bureaugenoot. Bedankt Stijn, om me het eerste jaar tal van tips te geven, en me te steunen bij het doorworstelen van soms moeilijke literatuurmomenten.
Bedankt alle andere collega's, lunchpauzegenoten, en vrienden. Klaas (x2), Bart, Barbara, Tamara, Christophe, Wim, Annelies, Stijn (x2), Veerle, Kris, Bino, Arne (x2), Peter, Klaartje, Andy, Beatrice, Bene, Tony, Katrien, Wouter, Yannick, Liesbeth, de voetbalvrienden, ... Neem het me niet kwalijk als ik iemand vergeet.
Vervolgens de personen die ik allicht het meeste dank verschuldigd ben: ma en pa. Bedankt om me de kans te geven te studeren, om me vrij te laten in mijn keuze, om me steeds weer te steunen! U bent fijne ouders.
Als laatste: mijn lieveling- Sylvie. Bedankt voor je vele geduld, liefde en steun!

Pascal,
mei 2006

Contents

Chapter 1

Introduction

The past century has seen the birth and incredible progress of nuclear and particle physics, ranging from the discovery of the nucleus to the recognition of Quantum Chromodynamics (QCD) as the fundamental theory of the strong interaction. But why studying nuclear physics in the first place? The nucleus, consisting of many baryons (protons and neutrons), provides a unique microscopic laboratory to test the structure of fundamental interactions. Indeed, most of the forces of nature are present in the nucleus - strong, electromagnetic, and weak. Furthermore, the majority of the mass and energy in the visible universe comes from nuclei and nuclear reactions. Accordingly, nuclear physics is crucial for understanding the early universe, the formation of elements, the stellar evolution , ... the substructure of matter.

How do we do nuclear physics? An important way of experimentally exploring the nuclear system is probing it with the aid of scattering processes. Indeed, the key element for understanding the structure and dynamics of hadronic matter is determining its response to an external probe as a function of energy and momentum transfer $(\omega, \vec{q})$. Despite the fact that hadronic probes imply the largest scattering cross sections, they have the clear disadvantage of heavily disturbing the structure of the nuclear target. Leptonic probes, on the other hand, require a larger experimental effort, but frisk the entire nuclear volume since they interact weakly.

Fig. 1.1 gives a qualitative sketch of the target's response to leptonic probes as a function of Q^2=$|\vec{q}|^2 - \omega^2$ and ω. For a single nucleon target, the first peak corresponds to elastic scattering, leaving the internal structure of the nucleon intact. The only energy transfer is the recoil energy of the nucleon. Elastic scattering occurs at

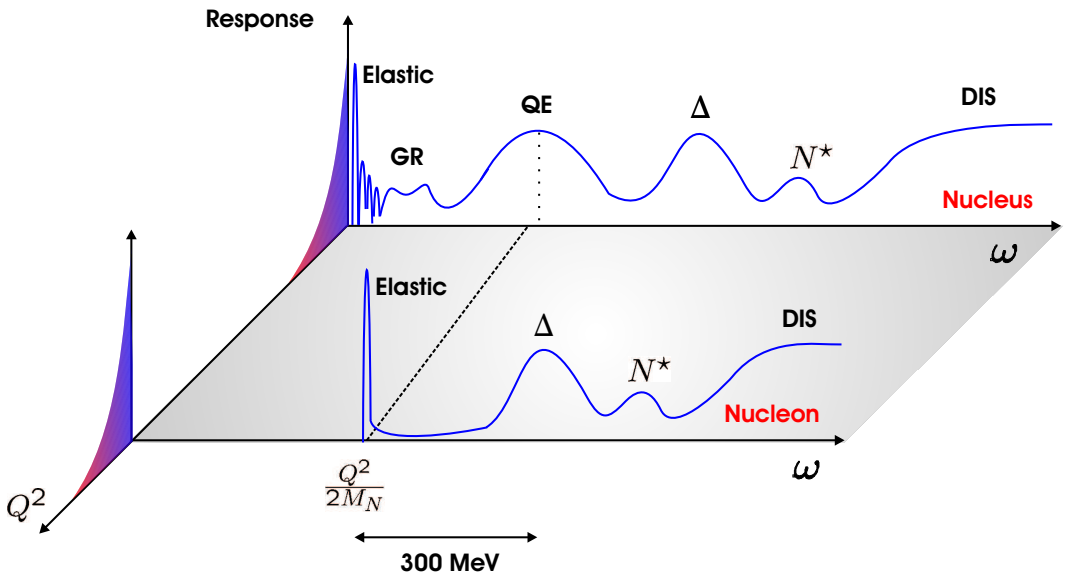

Figure 1.1 Schematic representation of the response to leptonic probes for both nuclei and nucleons, as a function of ω and Q^2.

Bjorken-variable $x \equiv Q^2/2M_N\omega$=1, with M_N the mass of the nucleon. The magnitude of the response asymptotically decreases with Q^2, pointing towards a finite spatial extension of the nucleon. At higher energy losses, inelastic scattering results in the production of nucleon resonances. The first nucleon excitation around 300 MeV corresponds to the Δ-resonance peak. The peaks at higher energies are produced by other overlapping baryon resonances. Pushing the energy and four-momentum transfer to extreme values, one enters the region of deep-inelastic scattering (DIS). In this region, the nucleon's response becomes only function of the Bjorken variable x and is independent of Q^2. This latter indicates that one scatters from the point-like quark constituents of the nucleon.

The response of a nucleus to leptonic probes is remarkably different. Here, elastic scattering occurs at x=A, with A the number of nucleons. Again, the magnitude of the responses decreases with increasing Q^2, reflecting the extended distribution of the target. Next, one observes inelastic scattering leading to the excitation of discrete nuclear levels. Above the particle emission threshold, one first enters the giant resonance region. The resonances stem from collective excitations of the nucleus as a whole. Next, a wide peak occurs at about ω=$Q^2/2M_N$. This is the so-called quasi-

elastic (QE) peak and corresponds to the elastic peak for a free nucleon at x=1. In this region, one expects that the leptonic probe induces the quasi-elastic knockout of a single nucleon. The striking broadening of the peak is due to the Fermi motion of the nucleons in the nucleus, whereas the shift in the peak position finds an explanation in the nucleon binding. At higher energies, one encounters the resonances corresponding to the excitation of the individual nucleons.

Throughout this work, we will focus on electromagnetic and weak lepton-nucleus interactions in the quasi-elastic region.

Electromagnetic interactions

Traditional models of nuclei rely on the shell model, where it is assumed that both protons and neutrons move in a self-consistent mean-field potential. In 1962 Jacob and Maris pointed out that quasi-elastic $(e, e'p)$ scattering had the potential to be a versatile experimental technique to probe the energy levels and structures of the shells of light and complex nuclei [1]. Two years later, pioneering experimental work was performed by U. Amaldi *et al.* at the Frascati synchrotron [2]. They were the first to actually measure the shell structure and binding energies of ^{12}C and ^{27}Al with the aid of quasi-elastic $(e, e'p)$ scattering. The shell model could remarkably explain the experimental results and green light was given for an extensive study of the low-energy part of the nuclear spectral function. Exclusive $A(e, e'p)$ reactions (whereby the residual $A-1$ nucleus is left in the discrete part of its energy spectrum) on a whole range of target nuclei revealed that the momentum distributions of bound low-energy protons in nuclei are in line with the predictions of the nuclear mean-field model. The occupation probabilities for the single-particle levels, on the other hand, turned out to be substantially smaller than what could be expected within the context of a naive mean-field model [3]. This provided sound evidence for the importance of short- and long-range correlations for the properties of nuclei [4, 5].

Nowadays, the availability of continuous-wave electron accelerators and high-resolution and large-acceptance spectrometers has shifted the scope of exclusive $(e, e'p)$ measurements towards higher energies in conjunction with other physics' issues. The role played by relativistic effects in nuclei has been the subject of investigation in [6]. In addition, exclusive processes are essential in studies of the transi-

tion from the non-perturbative to the perturbative QCD region. Searches for the onset of the color transparency phenomenon in $A(e,e'p)$ reactions play a pivotal role in stipulating the relevant degrees of freedom [7]. This genuine QCD phenomenon predicts a significant enhancement of the transmission of protons through nuclei at sufficiently high Q^2. Another fundamental issue concerns the delicate question whether or not nucleons are modified when they are embedded in a dense hadronic medium like the nucleus [8, 9]. In this way, $A(e,e'p)$ reactions serve as a stringent test for hadronic structure models.

In order to extract physical information from exclusive $A(e,e'p)$ measurements, one needs to interpret the obtained observables in terms of a theoretical framework. Basically, modeling $A(e,e'p)$ reactions involves three ingredients:

- The electromagnetic electron-nucleus coupling.
- The structure of the target nucleus.
- The propagation of the struck nucleon through the nuclear medium and its interaction with the residual nucleons.

The issue of nucleon propagation through the nuclear medium has received much attention during the last decades. Traditionally, at lower values of Q^2 most theoretical work was performed in the context of the distorted-wave impulse approximation (DWIA) [10, 11]. In such an approach, one assumes that the electron-nucleus interaction occurs through the individual nucleons. This is the so-called impulse approximation (IA). The target nucleus is usually described in terms of an independent particle model (IPM) picture, and the initial and final A-nucleon wave functions are taken to be Slater determinants. These latter are composed of single-particle wave functions which are solutions to a one-body Schrödinger equation. The final-state interactions (FSI) with the residual nucleons are incorporated in terms of proton optical potentials, containing a real and imaginary part. The parameters for these optical potentials are usually obtained from proton-nucleus elastic scattering experiments.

Relativistic effects in the kinematics of the scattering process, however, are expected to become critical in the GeV energy regime. Accordingly, a concerted research effort which started back in the late eighties has resulted in the development

of a number of relativistic DWIA (RDWIA) models for computing $A(e,e'p)$ observables [12, 13, 14, 15, 16]. In essence, these models adopt similar assumptions as their non-relativistic counterparts. The relativistic bound-state single-particle wave functions are customarily obtained within the framework of the Hartree approximation to the $\sigma-\omega$ model [17]. Scattering states by solving a time-independent Dirac equation with relativistic optical potentials.

The road to high-energy formalisms, however, is paved with obstacles. Indeed, optical potentials are usually not available for proton lab momenta exceeding roughly 1 GeV. Moreover, the use of optical potentials for modeling FSI processes in this region does not seem very natural in view of the highly inelastic character and diffractive nature of the underlying elementary nucleon-nucleon scattering cross sections. At higher energies, the so-called Glauber framework, which is a multiple-scattering extension of the eikonal approximation (EA)[18], provides a valid and economical alternative. The EA was originally introduced in optics by R. Glauber, who was recently awarded with the Nobel prize in physics for his contribution to the quantum theory of optical coherence. In a Glauber model, FSI are described within the approximation of the additivity of phases, acquired in the sequential rescatterings of high-energy projectiles off the target nucleons. The effects of FSI on the $A(e,e'p)$ observables are computed directly from the elementary proton-nucleon scattering data through the introduction of a profile function. The Glauber method postulates linear trajectories and frozen spectator nucleons. In the past, this formalism was successful in describing the data on elastic hadron-nucleus scattering at hadron energies $1 < E_h < 10-15$ GeV [19, 20]. A non-relativistic study of the Glauber formalism in $d(e,e'p)n$ (^{4}He$(e,e'p)$) reactions can be found in Refs. [21, 22] ([23]). For $(e,e'p)$ reactions off nuclei heavier than ^{12}C and nuclear matter, non-relativistic Glauber calculations have e.g. been reported in Refs. [24, 25, 26, 27].

In this work we present a relativistic formulation of Glauber theory for calculating $A(e,e'p)$ observables. The model can be formally applied in a wide Q^2 range. The major assumptions underlying our relativistic and unfactorized model bear a strong resemblance with those adopted in the RDWIA models developed during the last two decades. One of the primary goals of this thesis is to put the assumptions underlying our relativistic Glauber model to stringent tests by comparing our results to calculations of the RDWIA model as implemented by the Madrid-Sevilla

group [15]. In addition, we will confront our results to the world $A(e, e'p)$ -data.

Weak interactions

The neutral lepton family members are called neutrinos, and were postulated by Pauli in 1930 in order to account for the energy and momentum missing in the process of nuclear β-decay. Their experimental verification would take another 26 years. In the standard model, neutrinos are considered as massless, neutral stable particles and as left-handed fields. The mass of the neutrino remains one of the enigmas in elementary particle physics. Recent experiments as SNO and SK [28] convinced the world that neutrinos oscillate between their different flavor states, making the claims of non-zero neutrino masses and extensions of the standard model irrefutable. Nowadays, several experiments are running or proposed in order to address intriguing questions in current neutrino physics [29]: What does the neutrino mass hierarchy look like, and what are the values of the oscillation parameters [28]? What is the role of the vacuum and matter-enhanced oscillations ? Are neutrinos representatives of CP-violation in the leptonic sector ? Is the neutrino a Dirac or a Majorana particle ? Can one detect neutrinoless double-beta decay? Does the neutrino have a magnetic moment ? [30].

The interest in neutrinos goes beyond the study of the particle's intrinsic properties, and extends to a variety of topics in astro-, nuclear and hadronic physics. Typical astrophysical examples include the understanding of the energy production in our sun, neutrino nucleosynthesis and the synthesis of heavy elements during the r-process, the influence of neutrinos on the dynamics of a core-collapse supernova explosion and the cooling of a proto-neutronstar [31, 32]. In many astrophysical situations the neutrinos serve as messengers probing the interior of dense and opaque objects that otherwise remain inaccessible. The influence of neutrinos even extends to cosmological questions such as the role of neutrinos in the matter-antimatter asymmetry in the universe.

In hadronic and nuclear physics, the use of neutrino probes is still scarcely out of the egg. Indeed, despite the fact that neutrinos are ubiquitous, they have an extremely faint interaction strength which makes experiments with them very challenging. The advent of a high-intensity neutrino beam at Fermilab will offer a unique opportunity to gain new information on the structure of the nucleon and

baryonic resonances. Experiments such as MINERνA [30] and FINeSSE [33] will address relevant problems like the extraction of the electroweak form factors, the study of the strange quark content of the nucleon and ν-induced pion production. Nuclei, however, will be used as neutrino detectors, providing relatively large cross sections that offer a broad variety of information.

Once again, theoretical calculations are unavoidable in order to extract physical information from the measured neutrino-nucleus cross sections. As they both belong to the lepton family, neutrinos and electrons can probe comparable bulk and surface parts of the target nucleus. The main differences between neutrino and electron interactions stem from the intrinsic polarization of the neutrino, and the weak interaction. In accordance with $A(e, e'p)$ reactions, theoretical neutrino-nucleus modeling has to deal with three basic ingredients. Identical approaches can be adopted to determine the neutrino-nucleus coupling and the initial and final nucleon wave functions. In this work, we extend our relativistic Glauber formalism -which was initially designed for the description of exclusive electron-nucleus scattering processes- to deal with FSI in quasi-elastic inclusive neutrino-nucleus scattering processes. The extension is rather straightforward, since in our model, the propagation of the struck nucleon depends on its energy, and is independent of the leptonic probe.

Outline

The outline of this work is as follows.

- In Chapter 2, we first sketch the formalism for computing $A(\vec{e}, e'p)$ observables. Next, we focus on the question how to model the electron-nucleus coupling and we briefly shed light on the method employed to determine the bound states. The main part of this chapter, however, is devoted to various methods to deal with final-state interactions. In particular, we scrutinize the eikonal approximation and develop a relativistic formulation of Glauber theory. We end this chapter with a study of the properties of the Dirac-Glauber phase. The latter accounts for the FSI effects when computing $A(e, e'p)$ observables.

- Chapter 3 provides an intensive study of the nuclear transparency, which

gives a measure of the probability that a nucleon of a certain energy escapes from the nucleus without any further interaction. We present results for the target nuclei ^{12}C ,^{56}Fe and ^{208}Pb , and confront them to the world data. We show that, despite the very different model assumptions underlying the treatment of FSI in Glauber ("nucleon-nucleon") and optical potential ("nucleon-nucleus") models, comparable nuclear transparencies are obtained for kinematic regimes where both models are applicable. Finally, we present our results which account for the color transparency phenomenon.

- In Chapter 4, we focus on double-polarization observables. We pay attention to the delicate question whether or not nucleons are modified in the nuclear medium. The predictions with free and various parametrizations for the medium-modified electromagnetic form factors are compared to the world data. Next, we put our relativistic Glauber formalism, and in particular the eikonal approximation, to more stringent tests by focusing on quantities that are really sensitive to the details of the calculation.

- In Chapter 5, we deal with neutrino-nucleus interactions in the relativistic Glauber formalism. Results are presented for quasi-elastic neutrino scattering from ^{12}C and ^{56}Fe. We provide benchmark calculations in the limit of vanishing FSI, and argue that nuclear transparencies extracted from $A(e,e'p)$ measurements can be used to obtain realistic estimates of the effect of FSI mechanisms on quasi-elastic neutrino-nucleus cross sections. Finally, we shed light on various ratios of cross sections that have been proposed in order to probe the strange quark content of the nucleon. Particular attention is paid to the helicity asymmetry and results are shown employing the predictions of various hadronic structure models.

- Our concluding remarks are summarized in Chapter 6. Appendix A gives a brief overview of the adopted notations and conventions.

Chapter 2

$A(\vec{e}, e'\vec{p})$ reactions in a relativistic Glauber approach

More than 50 years of active research have illustrated that electron scattering is a powerful tool for studying the structure of hadronic systems such as atomic nuclei and their constituents. The electromagnetic interaction is well-known from the fundamental theory of quantum electrodynamics (QED) and is weak compared with the interaction strength between hadrons. This property allows electromagnetic probes to penetrate deep into hadrons, in contrast with hadronic ones which are mainly absorbed at the target's surface. When considering electron scattering from nucleons and nuclei, the major uncertainties in the reaction modeling arise in the electron-nucleon (nucleus) coupling and the physics governing the structure and the dynamics of the nucleon (nucleus). The weak fine-structure constant $\alpha \approx 1/137$ gives rise to a first-order perturbation treatment of the interaction. This procedure is usually referred to as the one-photon exchange approximation (OPEA). Dispersive corrections due to higher-order photon exchange contributions were shown to be roughly inversely proportional to the incident electron energy, and are expected to be of no impediment in the intermediate to high energy range [34, 35, 36, 37, 38]. Recent form-factor results from double polarization experiments, however, call these assertions into question, stressing the importance of two-photon exchange processes[39]. Nevertheless, we will impose the OPEA, since it is commonly adopted in most theoretical frameworks. Throughout this work we will rely on the plane-wave Born approximation (PWBA), neglecting Coulomb

distortion effects of the incident and scattered electron wave functions. Coulomb distortions introduce in the components of the nuclear response a dependence on all the kinematic variables of the incoming and outgoing electrons and have been the subject of intensive investigations in the past [10, 13, 15, 40].

In this chapter, we present a relativistic model for describing $A(\vec{e},e'\vec{p})$ processes, in which a polarized electron with helicity h impinges on a nucleus and induces the knockout of a single (polarized) nucleon, leaving the residual nucleus in a specific discrete state. Accordingly, low excitation energies are probed and the proton absorbs the major fraction of the transferred energy. We follow the conventions for the $A(\vec{e},\vec{e}'\vec{p})$ kinematics and observables introduced by Donnelly and Raskin in Refs. [41, 42]. We conform to the conventions of Bjorken and Drell [43] for the γ matrices and the Dirac spinors, and take $\hbar$=c=1.

2.1 Formalism: observables and kinematics

For the time being, we will neglect the polarization of the ejectile in the reaction, and consider the reaction $A(\vec{e},e'p)$ shown in Fig. 2.1. The four-momenta of the incident and scattered electron are denoted as $K^\mu(\varepsilon,\vec{k})$ and $K^\mu(\varepsilon',\vec{k}')$.The electron momenta $\vec{k}$ and $\vec{k}'$ define the scattering plane. The four-momentum transfer is given by $q^\mu=(\omega,\vec{q})=K^\mu-K'^\mu=K^\mu_{A-1}+K^\mu_f-K^\mu_A$, where $K^\mu_A(E_A,\vec{k}_A)$, $K^\mu_{A-1}(E_{A-1},\vec{k}_{A-1})$ and $K^\mu_f(E_f,\vec{k}_f)$ represent the four-momenta of the target nucleus, the residual nucleus and the ejected nucleon. The $z-$axis lies along the momentum transfer $\vec{q}$, the $y-$axis along $\vec{k}\times\vec{k}'$ and the $x-$axis lies in the scattering plane. The hadron reaction plane is defined by $\vec{k}_f$ and $\vec{q}$. The electron charge is denoted by $-e$. For spacelike momentum transfer one has $q^2_\mu\equiv\omega^2-|\vec{q}|^2\leq 0$ and we adopt the standard convention $Q^2\equiv -q_\mu q^\mu$.

2.1.1 The $A(\vec{e},e'p)$ scattering cross section

In the laboratory frame, the exclusive differential cross section for $e+A\rightarrow e'+p+(A-1)$ processes can be written as [41, 42, 43]

$$\begin{aligned} d\sigma &= \frac{1}{\beta}\overline{\sum_{if}}|\mathcal{M}_{fi}|^2\frac{m_e}{\varepsilon}\frac{m_e}{\varepsilon'}d^3\vec{k}'\frac{M_{A-1}}{E_{A-1}}d^3\vec{k}_{A-1}\frac{M_N}{E_f}d^3\vec{k}_f \\ &\times (2\pi)^{-5}\delta^4(K^\mu_e+K^\mu_A-K^\mu_{e'}-K^\mu_{A-1}-K^\mu_f), \end{aligned} \tag{2.1}$$

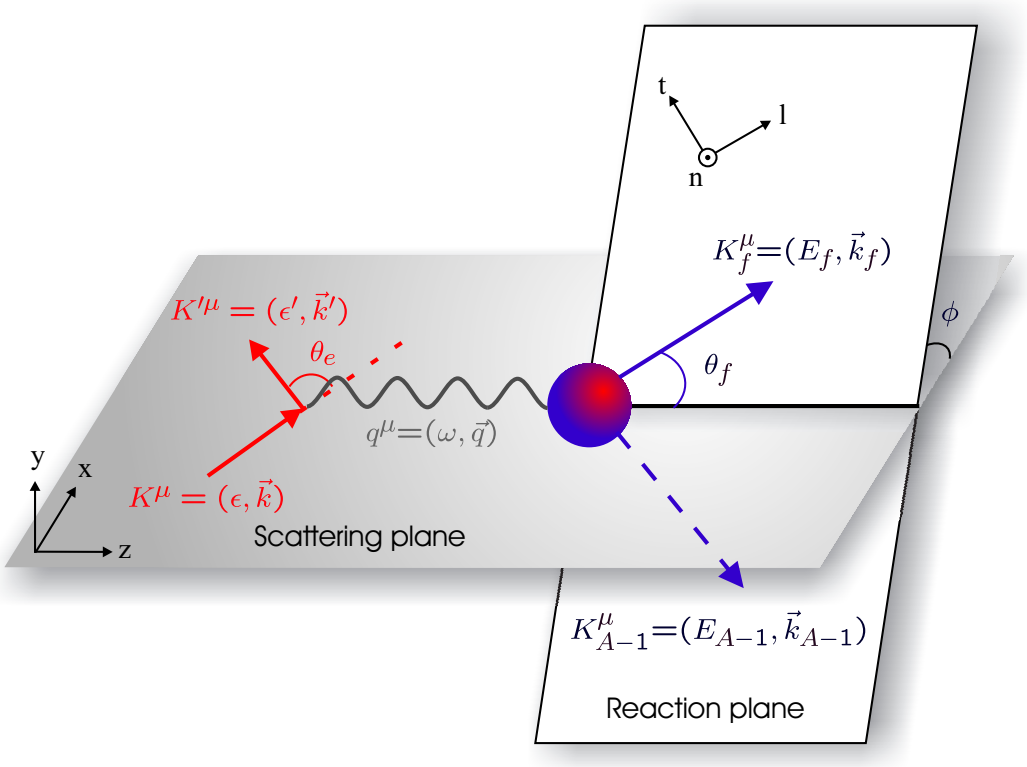

Figure 2.1 Kinematics for the quasi-elastic electron-nucleus scattering process.

where $\overline{\sum}_{if}$ indicates sum and/or average over initial and final spins. In the extreme relativistic limit (ERL, $m_e \ll \varepsilon$), the relative initial velocity β can trivially be put to 1. In this expression, m_e, $M_A(M_{A-1})$ and M_N represents the rest mass of the electron, the target (residual) nucleus and the outgoing proton, respectively. $\mathcal{M}_{fi}$ is the invariant matrix-element which reflects the transition between initial and final states. Hereby, the normalization condition for the Dirac plane-waves, characterized by a four-momentum K^μ and spin-state S^μ, is

$$\overline{u}(K^\mu,S^\mu)u(K^\mu,S^\mu)=1. \tag{2.2}$$

Integrating over the unobserved momentum of the recoiling nucleus $\vec{k}_{A-1}$, as well as over $|\vec{k_f}|$, results in the following five-fold differential cross section

$$\frac{d^5\sigma}{d\varepsilon' d^2\Omega_{e'} d^2\Omega_f}=\frac{m_e^2 M_N M_{A-1}}{(2\pi)^5 M_A \varepsilon'}\frac{k'k_f}{k}f_{rec}^{-1}\overline{\sum_{if}}|\mathcal{M}_{fi}|^2, \tag{2.3}$$

where f_{rec} is the hadronic recoil factor

$$f_{rec} = \frac{E_{A-1}}{M_A}\left|1 + \frac{E_f}{E_{A-1}}\left[1 - \frac{\vec{q}\cdot\vec{k}_f}{k_f^2}\right]\right| . \tag{2.4}$$

Fig. 2.2 shows the lowest order (OPEA) conceptual diagram for the exclusive $A(\vec{e},e'p)$ scattering process. The virtual photon is represented by the propagator $D_F(Q)_{\mu\nu}$=$-g_{\mu\nu}/Q^2$. The corresponding squared invariant matrix element $\mathcal{M}_{fi}$ can be written as

$$\overline{\sum_{if}}|\mathcal{M}_{fi}|^2 = \frac{(4\pi\alpha)^2}{(Q^2)^2}\eta_e(K,S';K,S)_{\mu\nu}W^{\mu\nu} . \tag{2.5}$$

In this equation, the electron tensor $\eta_e(K_{e'},S';K_e,S)_{\mu\nu}$ is defined by

$$\eta_e(K,S';K,S)_{\mu\nu} \equiv \overline{\sum_{if}}\left[\overline{u}_e(K',S')\gamma_\mu u_e(K,S)\right]^\dagger\left[\overline{u}_e(K',S')\gamma_\nu u_e(K,S)\right] . \tag{2.6}$$

The nuclear response tensor $W^{\mu\nu}$ describes the electromagnetic structure of the target and contains all of the dynamics of interest. Recognizing that the response tensors are bilinear in matrix elements of the current operator, it is useful to establish the schematic notation

$$W^{\mu\nu} \equiv \overline{\sum_{if}}\langle J^\mu\rangle^\dagger\langle J^\nu\rangle , \tag{2.7}$$

with

$$\langle J^\mu\rangle = \langle A-1(J_R,M_R),K_f(E_f,\vec{k}_f)m_s|\hat{J}^\mu|A(0^+,g.s.)\rangle . \tag{2.8}$$

Here, $\hat{J}^\mu$ is the electromagnetic current operator, $|A(0^+,g.s.)\rangle$ the ground state of the target even-even nucleus and $|A-1(J_R,M_R)\rangle$ the discrete state in which the residual nucleus is left.

In the most general case, the contraction of the electron tensor $\eta_{\mu\nu}$ with the nuclear one $W^{\mu\nu}$ results in an expression of the form [41]:

$$4m_e^2\eta_e(K_{e'},S';K_e,S)_{\mu\nu}W^{\mu\nu} = v_0\sum_K v_K\mathcal{R}_K , \tag{2.9}$$

where the label K takes on the values L, T, TT, TL, T', TL', $\underline{TT}$, $\underline{TL}$ and $\underline{TL'}$ and refers to the longitudinal and transverse components of the virtual photon polarization. The underlined ones can be safely ignored in the ERL, since they appear

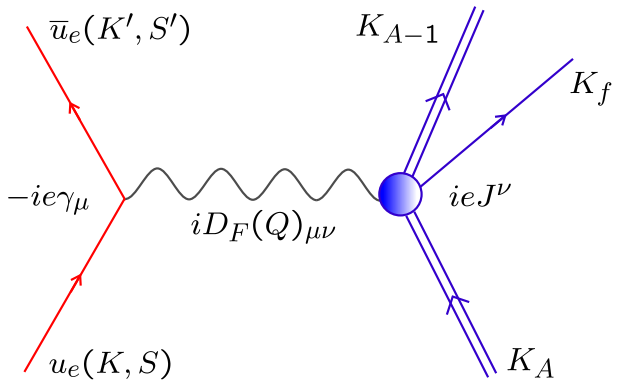

Figure 2.2 Lowest order (OPEA) conceptual diagram corresponding to the exclusive $A(\vec{e}, e'p)$ scattering process.

with a factor m_e/ε. The key element for understanding the structure and dynamics of hadronic matter is its response to an external probe as a function of energy and momentum transfer. This is all contained in the nuclear response functions $\mathcal{R}_K$. Further, $v_0 \equiv (\varepsilon + \varepsilon')^2 - q^2$ and the v_K depend on the electron kinematics.

Combination of the above results leads to the following final expression for the $A(\vec{e}, e'p)$ differential cross section [41, 42]

$$\begin{aligned}
&\left(\frac{d^5\sigma}{d\epsilon' d\Omega_{e'} d\Omega_p}\right)^h_{fi} \\
&= \frac{M_N M_{A-1} k_f}{8\pi^3 M_A} f_{rec}^{-1} \sigma_M \Big[(v_L \mathcal{R}_L + v_T \mathcal{R}_T + v_{TT} \mathcal{R}_{TT} \cos 2\phi + v_{TL} \mathcal{R}_{TL} \cos\phi) \\
&+ h\,(v_{T'} \mathcal{R}_{T'} + v_{TL'} \mathcal{R}_{TL'} \sin\phi) \Big] \\
&\equiv \Sigma_{fi} + h\Delta_{fi}\ .
\end{aligned} \tag{2.10}$$

In this expression, σ_M is the Mott cross section

$$\sigma_M = \left(\frac{\alpha \cos\theta_e/2}{2\varepsilon \sin\theta_e/2^2}\right)^2\ , \tag{2.11}$$

θ_e the angle between the incident and scattered electron and ϕ the azimuthal angle of the plane defined by $\vec{q}$ and $\vec{k}_f$. In the ERL, h reduces to the electron helicity for a longitudinal polarized beam. The first term Σ_{fi} is independent of the electron's polarization. The second term Δ_{fi} only appears when the initial beam is polarized.

The electron kinematics is contained in the kinematical factors

$$v_L = \left(\frac{Q^2}{q^2}\right)^2, \tag{2.12}$$

$$v_T = \tan^2\frac{\theta_e}{2} + \frac{Q^2}{2|\vec{q}|^2}, \tag{2.13}$$

$$v_{TT} = -\frac{Q^2}{2|\vec{q}|^2}, \tag{2.14}$$

$$v_{TL} = -\frac{1}{\sqrt{2}}\left(\frac{Q^2}{|\vec{q}|^2}\right)\sqrt{\tan^2\frac{\theta_e}{2} + \frac{Q^2}{|\vec{q}|^2}}, \tag{2.15}$$

$$v_{T'} = \tan\frac{\theta_e}{2}\sqrt{\tan^2\frac{\theta_e}{2} + \frac{Q^2}{|\vec{q}|^2}}, \tag{2.16}$$

$$v_{TL'} = -\frac{1}{\sqrt{2}}\left(\frac{Q^2}{|\vec{q}|^2}\right)\tan\frac{\theta_e}{2}. \tag{2.17}$$

The corresponding response functions read

$$\mathcal{R}_L = \left|\langle\rho(\vec{q})\rangle\right|^2, \tag{2.18}$$

$$\mathcal{R}_T = \left|\langle J^+(\vec{q})\rangle\right|^2 + \left|\langle J^-(\vec{q})\rangle\right|^2, \tag{2.19}$$

$$\mathcal{R}_{TT}\cos 2\phi = 2\Re\left\{\langle J^+(\vec{q})\rangle^*\langle J^-(\vec{q})\rangle\right\}, \tag{2.20}$$

$$\mathcal{R}_{TL}\cos\phi = -2\Re\left\{\langle\rho(\vec{q})\rangle^*\left(\langle J^+(\vec{q})\rangle - \langle J^-(\vec{q})\rangle\right)\right\}, \tag{2.21}$$

$$\mathcal{R}_{T'} = \left|\langle J^+(\vec{q})\rangle\right|^2 - \left|\langle J^-(\vec{q})\rangle\right|^2, \tag{2.22}$$

$$\mathcal{R}_{TL'}\sin\phi = -2\Re\left\{\langle\rho(\vec{q})\rangle^*\left(\langle J^+(\vec{q})\rangle + \langle J^-(\vec{q})\rangle\right)\right\}. \tag{2.23}$$

In the above expressions , $\langle\rho(\vec{q})\rangle \equiv \langle J^0(\vec{q})\rangle$ denotes the Fourier transform of the transition charge density $\langle f|\hat{\rho}(\vec{r})|i\rangle$, while

$$\langle f|\vec{J}(\vec{q})|i\rangle = \sum_{m=0,\pm1}\langle f|J(\vec{q};m)\vec{e}_m^{\dagger}|i\rangle\ , \tag{2.24}$$

is the expansion of the Fourier transform of the transition three-current in terms of the standard unit spherical vectors defined by

$$\vec{e}_0 = \vec{e}_z, \qquad \vec{e}_{\pm1} = \mp\frac{1}{\sqrt{2}}(\vec{e}_x \pm i\vec{e}_y). \tag{2.25}$$

Furthermore, current conversation imposes that only three components of J^μ are independent:

$$q_\mu J^\mu(\vec{q}) = \omega\rho(\vec{q}) - qJ(\vec{q};0) = 0\ , \tag{2.26}$$

so that $J^\mu = \left(\rho, J_x, J_y, \frac{\omega}{q}\rho\right)$.

Finally, we remark that the transverse response function $R_{T'}$ naturally vanishes when no hadronic polarization is detected [41, 44]. As a result, the fivefold differential cross section for $A(\vec{e}, e'p)$ reactions can be cast in the form

$$\left(\frac{d^5\sigma}{d\epsilon' d\Omega_{e'} d\Omega_p}\right)^h_{fi} = \sigma_0 \frac{1}{2}\left[1 + hA\right], \tag{2.27}$$

where σ_0 is the unpolarized cross section, h the electron helicity and A the "beam analyzing power".

2.1.2 Response functions for ejectile polarization

In this section, the formalism for coincidence reactions with nucleon emission is extended to include spin degrees of freedom of the ejected particle. At present, high-duty electron facilities allow to polarize electron beams in an adequate manner and simultaneously measure the spin orientation of the ejected hadron. Thus, coincidence reactions can be investigated in unprecedent conditions and access to the individual transition amplitudes is made possible by measuring polarization observables. This opens a window to fundamental issues like possible medium modifications of nucleons when they are embedded in a dense hadronic medium like the nucleus [8, 9, 45].

A diagram of the reaction may be found in Fig. 2.1. The polarization of the outgoing nucleon is expressed in the so-called barycentric reference frame that is defined by the following set of unit vectors

$$\vec{l} = \frac{\vec{k}_f}{\mid \vec{k}_f \mid} \quad , \quad \vec{n} = \frac{\vec{q} \times \vec{k}_f}{\mid \vec{q} \times \vec{k}_f \mid} \quad , \quad \vec{t} = \vec{n} \times \vec{l}\,. \tag{2.28}$$

The nuclear response tensor $W^{\mu\nu}$ of Eq. (2.7) transforms as a hermitian Lorentz tensor of rank two, and is at most linear in the ejectile spin. In addition, parity and current conservation must be satisfied. Therefore, introduction of a well defined polarization state for the ejectile, amounts to replace the response functions appearing in the unpolarized Eqs. (2.10,2.18) by the following 18 independent re-

sponse functions[46, 47]:

$$\mathcal{R}_L \equiv \mathcal{R}_L^o + \mathcal{R}_L^n \vec{\sigma}\cdot\vec{n} \tag{2.29}$$

$$\mathcal{R}_T \equiv \mathcal{R}_T^o + \mathcal{R}_T^n \vec{\sigma}\cdot\vec{n} \tag{2.30}$$

$$\mathcal{R}_{TT}\cos 2\phi \equiv (R_{TT}^o + R_{TT}^n \vec{\sigma}\cdot\vec{n})\cos 2\phi + \left(R_{TT}^t \vec{\sigma}\cdot\vec{t} + R_{TT}^l \vec{\sigma}\cdot\vec{l}\right)\sin 2\phi \tag{2.31}$$

$$\mathcal{R}_{TL}\cos\phi \equiv (R_{TL}^o + R_{TL}^n \vec{\sigma}\cdot\vec{n})\cos\phi + \left(R_{TL}^t \vec{\sigma}\cdot\vec{t} + R_{TL}^l \vec{\sigma}\cdot\vec{l}\right)\sin\phi \tag{2.32}$$

$$\mathcal{R}_{T'} \equiv \left(R_{T'}^t \vec{\sigma}\cdot\vec{t} + R_{T'}^l \vec{\sigma}\cdot\vec{l}\right) \tag{2.33}$$

$$\mathcal{R}_{TL'}\sin\phi \equiv (R_{TL'}^o + R_{TL'}^n \vec{\sigma}\cdot\vec{n})\sin\phi + \left(R_{TL'}^t \vec{\sigma}\cdot\vec{t} + R_{TL'}^l \vec{\sigma}\cdot\vec{l}\right)\cos\phi \tag{2.34}$$

In the presence of parity-violating components, 36 response functions need to be considered. These arise from the 9 independent tensors that can be constructed for the unpolarized case and for each of the three possible polarization states. A nice classification of the 18 response functions according to their dependencies upon θ_f, the out-of-plane angle ϕ and final-state interactions (FSI) can e.g. be found in Ref. [46].

These replacements result in the following general form for the fivefold $A(\vec{e},e'\vec{p})$ differential cross section:

$$\left(\frac{d^5\sigma}{d\epsilon' d\Omega_{e'} d\Omega_p}\right)_{fi}^{h} = \sigma_0 \frac{1}{2}\left[1 + \vec{P}\cdot\vec{\sigma} + h(A + \vec{P'}\cdot\vec{\sigma})\right], \tag{2.35}$$

where $\vec{P}(\vec{P'})$ is the induced (transferred) polarization. The induced polarization can be addressed with unpolarized electrons (i=n,l,t)

$$P_i = \frac{d^5\sigma(\sigma_i =\uparrow) - d^5\sigma(\sigma_i =\downarrow)}{d^5\sigma(\sigma_i =\uparrow) + d^5\sigma(\sigma_i =\downarrow)}, \tag{2.36}$$

whereas the polarization transfer also requires polarized electron beams (i=n,l,t)

$$P_i' = \frac{\left[d^5\sigma^+(\sigma_i =\uparrow) - d^5\sigma^-(\sigma_i =\uparrow)\right] - \left[d^5\sigma^+(\sigma_i =\downarrow) - d^5\sigma^-(\sigma_i =\downarrow)\right]}{\left[d^5\sigma^+(\sigma_i =\uparrow) + d^5\sigma^-(\sigma_i =\uparrow)\right] + \left[d^5\sigma^+(\sigma_i =\downarrow) + d^5\sigma^-(\sigma_i =\downarrow)\right]}, \tag{2.37}$$

where σ_i= $\uparrow$ ($\downarrow$) denotes that the ejected hadron has a spin (anti)parallel to the i direction, and where the plus (minus) sign in $\sigma^{\pm}$ refers to the helicity h of the electron impinging on the target nucleus. One distinct advantage of polarization observables is that they result from cross-section ratios. As a consequence, unlike the response functions, they are independent of overall scaling factors, like e.g.

spectroscopic factors. These latter ones arise since the occupation probabilities for the single-particle levels turned out to be substantially smaller than what could be expected within the context of a naive mean-field model [3]. This observation provided sound evidence for the importance of short- and long-range correlations for the properties of nuclei [4, 5].

2.2 The electromagnetic current operator

We now turn to the question how to accomplish the electron-nucleus coupling in the transition matrix elements of Eqs. (2.7,2.8). According to QED, the current for a Dirac point-like particle is given in terms of its spinors as

$$J^\mu = \overline{u}_f \gamma^\mu u_i \ . \tag{2.38}$$

For a spin-$1/2$ particle with internal structure, the current can be written by introducing in Eq. (2.38) appropriate form factors. For a free nucleon, the Gordon identity allows expressions for the one-body vertex function J^μ in several equivalent forms of which some of the more frequently used ones read [48]

$$J^\mu_{cc1} = G_M(Q^2)\gamma^\mu - \frac{\kappa}{2M_N} F_2(Q^2)(K_i^\mu + K_f^\mu) \ , \tag{2.39a}$$

$$J^\mu_{cc2} = F_1(Q^2)\gamma^\mu + i\frac{\kappa}{2M_N} F_2(Q^2)\sigma^{\mu\nu} q_\nu \ , \tag{2.39b}$$

$$J^\mu_{cc3} = \frac{1}{2M_N} F_1(Q^2)(K_i^\mu + K_f^\mu) + i\frac{1}{2M_N} G_M(Q^2)\sigma^{\mu\nu} q_\nu \ , \tag{2.39c}$$

where F_1 is the Dirac, F_2 the Pauli, G_M the Sachs magnetic form factor and κ is the anomalous magnetic moment. In this work, we adopt the philosophy that the in-medium (or, off-shell) electron-proton vertex J^μ has the same Lorentz structure as the free-proton one. Accordingly, the electromagnetic interaction of the virtual photon with the target nucleus is supposed to occur through the individual nucleons. In combination with the assumption that the struck nucleon coincides with the detected one, this approach founds the so-called impulse approximation (IA), which has been successfully applied in a vast number of calculations. The electromagnetic coupling on a bound nucleon, however, implies that one can no longer compute the $A(e,e'p)$ reaction in a model-independent fashion. The reason for this is twofold. First, when considering off-shell nucleons embedded in a nuclear

medium, the vertex functions of Eq. (2.39) can no longer be guaranteed to produce identical results. This elusive feature is known as the Gordon ambiguity and is a source of uncertainties when performing calculations involving finite nuclei [48, 49, 50]. Another equally important issue, that is closely related to the Gordon ambiguity, is the gauge invariance of the electromagnetic current in many-body systems. In nuclear physics, imposing the Coulomb gauge is a widely used procedure to "effectively" restore current conservation and is based on modifying the longitudinal component of the nuclear vector current using the substitution

$$J_z \rightarrow \frac{w}{q}\rho \ . \tag{2.40}$$

This procedure is partly inspired on the observation that meson-exchange and isobar terms enter the charge current operator in a higher relativistic order than for the vector current. Other prescriptions which are meant to restore current conservation are e.g. the Lorentz and the Weyl gauge.

Often, the electromagnetic form factors are related to the charge and magnetization density. These are known as the Sachs form factors and are constructed in terms of the Dirac and Pauli form factors as follows:

$$G_E = F_1 - \tau\kappa F_2 \ , \qquad G_M = F_1 + \kappa F_2 \ , \tag{2.41}$$

with $\tau = Q^2/4M_N^2$. The adopted nomenclature of electric (G_E) and magnetic (G_M) stem from the fact that in the photon limit they are given by

$$G_E(Q^2=0) = \frac{Q}{e} \ , \qquad G_M(Q^2=0) = \frac{\mu}{\mu_N} \ , \tag{2.42}$$

where Q and μ are the nucleon's charge and magnetic moment.

For long, the accumulated data pointed towards electromagnetic form factors of the nucleon whose Q^2 dependence can be well described in terms of a dipole parametrization, given by

$$G_D(Q^2) = \frac{1}{\left(1+\frac{Q^2}{M_V^2}\right)^2} \ , \tag{2.43}$$

with M_V=0.843 (GeV/c). For the neutron electric form factor, one frequently uses the Galster parametrization [51]

$$G_E^n(Q^2) = -\frac{G_M^n(Q^2=0)a\tau}{1+b\tau}G_D(Q^2) \ , \tag{2.44}$$

with a=1 and b=5.6. Traditionnaly, the proton electromagnetic form factors were obtained by means of a Rosenbluth separation of elastic $p(e,e')p$ scattering measurements. New data obtained from polarization-transfer measurements $p(\vec{e},e')\vec{p}$ [52, 53] revealed a different picture for $Q^2 \geq 1$ (GeV/c)^2. Fig. 2.3 shows the ratio of G_E^p to G_M^p as extracted by Rosenbluth measurements (diamonds) and from polarization measurements (crosses). The solid line shows a fit using cross section data only. The dashed line displays the fit obtained from both the cross-section and polarization data and is denoted as the BBA-2003 parametrization [54, 55], in which the form factors read

$$G_{E,M}^N(Q^2) = \frac{G_{E,M}^N(Q^2=0)}{1+\sum_{n=1}^{6} a_{2n}(Q^2)^n} \; . \tag{2.45}$$

The coefficients a_{2n} are summarized in Table 2.1. The neutron electric form factor is parametrized as in Eq. (2.44), with a=0.942 and b=4.61.

	a_2	a_4	a_6	a_8	a_{10}	a_{12}
G_E^p	3.253	1.422	0.08582	0.3318	-0.09371	0.01076
G_M^p	3.104	1.428	0.1112	-0.006981	0.0003705	-0.7063E-05
G_M^n	3.043	0.8548	0.6806	-0.1287	0.00912	

Table 2.1 The coefficients a_{2n} of the BBA-2003 parametrization for G_E^p,G_M^p and G_M^n [54, 55].

The discrepancy between the electromagnetic form factors obtained with the two techniques is an unresolved issue. So far, most work has focussed on the possibility that two-photon exchange corrections may lead to an additional correction on the cross section. This correction has a significant dependence on the virtual-photon polarization. Such two-photon corrections were generally estimated to be small, and this appeared to be confirmed by measurements comparing positron and electron scattering. However, recent calculations of the two-photon corrections [56, 57], and a reexamination of the positron data [39], indicate that two-photon corrections may in fact play an important role in this kinematic region.

2.3 Relativistic bound-state wave functions

In this section, we briefly shed light on the bound-state wave functions entering Eqs. (2.7,2.8). An accurate description of the ground states of finite nuclei is one

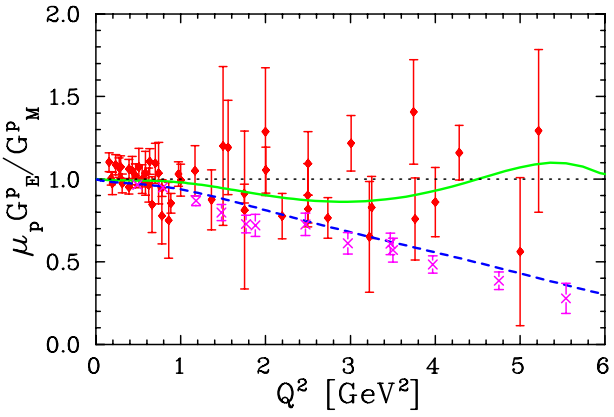

Figure 2.3 Ratio of G_E^p to G_M^p. The diamonds show the results from Rosenbluth extraction. The crosses result from polarization measurements [52, 53]. The solid line shows a fit using cross section data only. The dashed line shows the predictions from the BBA-2003 parametrization [54, 55]. This figure was taken from Ref. [54].

of the fundamental problems in theoretical physics. For many years, people relied on the non-relativistic Schrödinger equation in the hunt for nuclear structure and nucleon-nucleon interactions. A relativistic description of nuclei, however, has several virtues compared to the non-relativistic treatment. Indeed, in a field-theoretic approach the mesonic degrees of freedom can be implemented at the very early stage of the development of the model. Furthermore, constraints of causality, retardation, and relativistic kinematics can be incorporated naturally. In addition, whereas the spin-orbit interaction needs to be inserted by hand in non-relativistic approaches, it is inherently contained in relativistic theories.

A relativistic quantum field theory for atomic nuclei was proposed by Walecka in the 1970's [58]. This well-known "$\sigma-\omega$" model contains nucleons (ψ) interacting with scalar mesons (ϕ) through a Yukawa coupling $\overline{\psi}\psi\phi$ and with neutral vector mesons (V_μ) that couple to the conserved baryon current $\overline{\psi}\gamma_\mu\psi$. The lagrangian density is [17, 59]

$$\begin{aligned}\mathcal{L}_0 &= \bar{\psi}(\imath\partial\!\!\!/ - M)\psi + \frac{1}{2}(\partial_\mu\phi\partial^\mu\phi - m_s^2\phi^2) - \frac{1}{4}G_{\mu\nu}G^{\mu\nu} \\ &\quad + \frac{1}{2}m_v^2 V_\mu V^\mu - g_v\bar{\psi}\gamma_\mu\psi V^\mu + g_s\bar{\psi}\psi\phi\ , \end{aligned} \tag{2.46}$$

with M, m_s and m_v the nucleon, scalar meson and vector meson masses, respectively, and $G^{\mu\nu} \equiv \partial^\mu V^\nu - \partial^\nu V^\mu$ the vector meson field strength. The scalar (g_s) and

vector (g_v) fields may be associated with the σ and ω mesons. This model can be extended to include also isovector π and ρ mesons, as well as the coupling to the photon field [60]. Since the full quantum theory is highly complex, in practice a suitable approximate starting point is needed. As discussed by Walecka [58], the quantum field theory can be approximated by replacing the meson field operators with their expectation values at high densities. In infinite matter this amounts to $\langle\phi\rangle \equiv \phi_0$ and $\langle V^\mu\rangle \equiv \delta^{\mu 0} V_0$. In a Hartree-Fock approach, the resulting mean-field problem can then be solved in an iterative way.

In [61] it was shown that a Hartree calculation can be viewed as equivalent to a density-functional approach in which higher-order many-body corrections are treated approximately. A chiral effective field theory has been proposed in Ref. [62]. It includes all the relevant symmetries of QCD, such as Lorentz invariance, parity invariance, electromagnetic gauge invariance and isospin. In particular, the $SU(2)_L \times SU(2)_R$ chiral symmetry is realized nonlinearly. Applying a one-baryon-loop order in this model is equivalent to the Dirac-Hartree approximation [59]. The static Dirac equation with eigenvalues E_α and eigenfunctions $\phi_\alpha(\vec{r},\vec{\sigma})$ reads [17]

$$\hat{\mathcal{H}}\phi_\alpha(\vec{r},\vec{\sigma}) = E_\alpha \phi_\alpha(\vec{r},\vec{\sigma}), \tag{2.47}$$

where the single-particle Dirac Hamiltonian of [62] is given by

$$\hat{\mathcal{H}} = - i\vec{\alpha}\cdot\vec{\nabla} + g_v V_0(\vec{r}) + \frac{1}{2}\tau_3 g_\rho b_0(\vec{r}) + \beta(M - g_s\Phi_0(\vec{r})) \tag{2.48}$$

$$+ \frac{1}{2}(1+\tau_3)eA_0(\vec{r}) - \frac{i}{2M}\beta\vec{\alpha}\cdot\Big(f_\rho\frac{1}{2}\tau_3 g_\rho\vec{\nabla}b_0(\vec{r}) \tag{2.49}$$

$$+ f_v g_v\vec{\nabla}V_0(\vec{r})\Big) + \frac{1}{2M^2}(\beta_s + \beta_v\tau_3)e\vec{\nabla}^2 A_0(\vec{r}), \tag{2.50}$$

Here, Φ_0, V_0, b_0 and A_0 refer to the sigma, omega, rho and Maxwell mean fields, respectively. The corresponding couplings are denoted by g_s, g_v, g_ρ and e. The β_s and β_v are couplings for higher-order $\sigma(\omega)N$ and $\sigma\sigma(\omega\omega)$ interactions. f_ρ is the so-called tensor coupling. The pion field does not enter in the Hartree approximation, if one assumes that the nuclear ground state is spherically symmetric and a parity eigenstate [63].

For spherically symmetric potentials, the solutions $\phi_\alpha(\vec{r},\vec{\sigma})$ to a single-particle Dirac equation have the form [64]

$$\phi_\alpha(\vec{r},\vec{\sigma}) \equiv \phi_{n\kappa m}(\vec{r},\vec{\sigma}) = \begin{bmatrix} i\frac{G_{n\kappa}(r)}{r}\mathcal{Y}_{\kappa m}(\Omega,\vec{\sigma}) \\ -\frac{F_{n\kappa}(r)}{r}\mathcal{Y}_{-\kappa m}(\Omega,\vec{\sigma}) \end{bmatrix}, \tag{2.51}$$

where n denotes the principal, κ and m the generalized angular momentum quantum numbers. The $\mathcal{Y}_{\pm\kappa m}$ are the spin spherical harmonics and determine the angular and spin parts of the wave function,

$$\mathcal{Y}_{\kappa m}(\Omega,\vec{\sigma}) = \sum_{m_l m_s} \left\langle l m_l \frac{1}{2} m_s | l \frac{1}{2} j m \right\rangle Y_{l m_l}(\Omega) \chi_{\frac{1}{2} m_s}(\vec{\sigma}) \ ,$$
$$j = |\kappa| - \frac{1}{2} \ , \qquad l = \begin{cases} \kappa, & \kappa > 0 \\ -(\kappa+1), & \kappa < 0 \ . \end{cases} \tag{2.52}$$

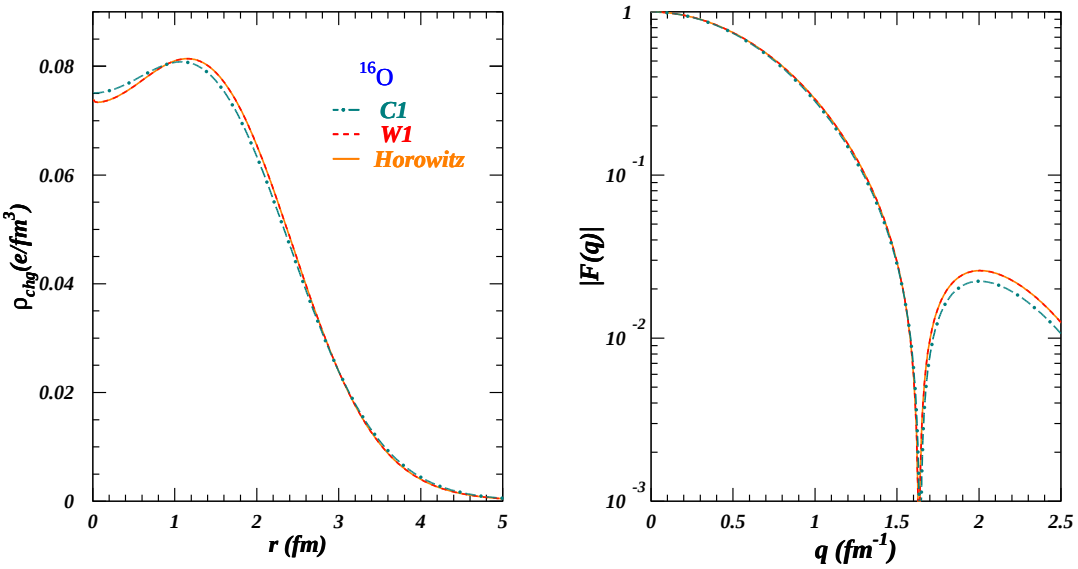

Figure 2.4 The left (right) panel shows the charge density (form factor) of ^{16}O . The solid line shows the prediction of Ref. [59]. The dashed (dot-dashed) line are the results obtained in the "W_1" ("C_1") parametrization for the different field strengths of Ref. [62].

Starting from an educated guess for the scalar and vector potential, the Dirac equations can be solved iteratively. The Hartree approximation yields then a set of coupled equations for the different fields, which constitute the basis of a relativistic Hartree approach. The eigenfunctions and eigenvalues depend on the meson masses and coupling constants. All bound-state wave functions contained in this work are determined in the "W1" parametrization for the different field strengths [62]. This parametrization predicts an average binding energy per nu-

cleon of 7.16(7.29) MeV for ^{12}C (^{16}O), which complies reasonably well with the empirical value of 7.42(7.72) MeV. Fig. 2.4 shows the charge density and form factor of ^{16}O in the "W1" and "C1" predictions of Ref. [62]. For comparison, also the results obtained with the different field strengths quoted by Horowitz *et al.* [59] are displayed.

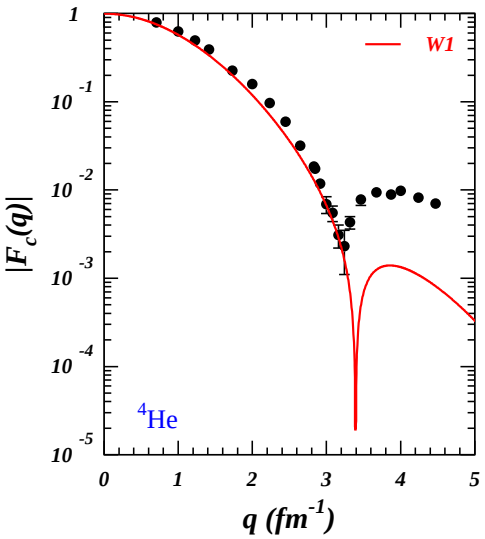

Figure 2.5 The charge form factor of ^{4}He, obtained within the W1 parametrization of Ref. [62]. The data are from [65] and [66].

Further on, ^{4}He$(e, e'p)$ results will be presented. At first sight, an independent particle-approximation for describing the four-nucleon system may appear as a venture into dangerous territory. However, at present, realistic relativistic wave functions for the ^{4}He ground state are not at hand. Wave functions based on a relativistic mean-field approach emerge as the only alternative when embarking on fully relativistic $A(e, e'p)$ calculations. As can be appreciated from Fig. 2.5, a fair description of the low-momentum part of the charge form factor for the ^{4}He nucleus is obtained with the "W1" parametrization. The deviation between the computed and measured charge form factor F_c at high momentum transfer can be partly attributed to large two-body charge contributions [67], which are neglected for the curve displayed in Fig. 2.5.

2.4 Relativistic formulation of Glauber theory

The remaining ingredient entering the transition matrix element of Eqs. (2.7,2.8) is the scattering state. Including nucleon-nucleus FSI is a long-standing issue in theoretical $A(e,e'p)$ reactions. At present there is no uniform and realistic framework in which the proton-nucleus FSI effects can be computed for proton kinetic energies ranging from low energies to several GeV. For kinetic energies up to around 1 GeV, most theoretical $A(e,e'p)$ investigations are performed within the context of the distorted-wave impulse approximation (DWIA) [10, 11], where the effect of the scatterings on the emerging nucleon is estimated with the aid of proton-nucleus optical potentials. Three important features of high-energy FSI make the extension of this medium energy formalism to high energies problematic. First, the number of relevant partial waves increases rapidly with the relative proton-$(A-1)$ energy. In addition, for proton kinetic energies T_p beyond 1 GeV parametrizations of optical potentials are usually not at hand. Finally, the NN interaction becomes predominantly inelastic for proton lab momenta exceeding 1 GeV. Accordingly, the use of optical potentials for modeling FSI processes does not seem natural. At higher energies, the so-called Glauber framework, which is a multiple-scattering extension of the eikonal approximation [18], provides a valid and economical alternative. In this model, FSI are described within the approximation of the additivity of phases, acquired in the sequential rescatterings of high-energy projectiles off the target nucleons.

In a Glauber framework, the effects of FSI on the $A(e,e'p)$ observables are computed directly from the elementary proton-nucleon scattering data through the introduction of a profile function. The Glauber method postulates linear trajectories and frozen spectator nucleons, and the lower-energy limit of this treatment to $A(e,e'p)$ has not yet been established. Before embarking on the study of a relativized version of Glauber theory, below, we first concentrate on the eikonal approximation which constitutes the baseline for the Glauber concept. The formalism outlined here follows the discussions of Refs. [68, 69].

2.4.1 Dirac-Eikonal approximation

We start our derivations by looking for solutions to the time-independent Dirac equation for a projectile with relativistic energy E=$\sqrt{k_f^2 + M_N^2}$ and spin state $|\frac{1}{2}m_s\rangle$ in the presence of spherical Lorentz scalar $V_s(r)$ and vector potentials $V_v(r)$

$$\mathcal{H}\Psi^{(+)}_{\vec{k}_f,m_s}(\vec{r}) = [\vec{\alpha}\cdot\hat{\vec{p}} + \beta M_N + \beta V_s(r) + V_v(r)]\Psi^{(+)}_{\vec{k}_f,m_s}(\vec{r}) = E\Psi^{(+)}_{\vec{k}_f,m_s}(\vec{r}) \ , \quad (2.53)$$

where we have introduced the notation $\Psi^{(+)}_{\vec{k}_f,m_s}$ for the unbound (scattered) Dirac states and $\hat{\vec{p}}$ represents the impulse operator. After some straightforward manipulations, a Schrödinger-like equation for the upper component emerges

$$\left[-\frac{\hbar^2\nabla^2}{2M_N} + V_c + V_{so}(\vec{\sigma}\cdot\vec{L} - i\vec{r}.\hat{\vec{p}})\right] u^{(+)}_{\vec{k}_f,m_s}(\vec{r}) = \frac{k_f^2}{2M_N} u^{(+)}_{\vec{k}_f,m_s}(\vec{r}) \ , \quad (2.54)$$

where the central and spin-orbit potentials V_c and V_{so} are defined as

$$V_c(r) = V_s(r) + \frac{E}{M_N}V_v(r) + \frac{V_s^2(r) - V_v^2(r)}{2M_N} \ , \quad (2.55)$$

$$V_{so}(r) = \frac{1}{2M_N[E + M_N + V_s(r) - V_v(r)]}\frac{1}{r}\frac{d}{dr}[V_v(r) - V_s(r)] \ . \quad (2.56)$$

Since the lower component is related to the upper one through

$$w^{(+)}_{\vec{k}_f,m_s}(\vec{r}) = \frac{1}{E + M_N + V_s(r) - V_v(r)}\vec{\sigma}\cdot\hat{\vec{p}}u^{(+)}_{\vec{k}_f,m_s}(\vec{r}) \ , \quad (2.57)$$

the solutions to Eq. (2.54) determine the complete relativistic eigenvalue problem. In RDWIA approaches, an equation of the type (2.54) is solved numerically for Dirac optical potentials $V_s(r)$ and $V_v(r)$ derived from global fits to elastic proton-nucleus scattering data [70]. The potentials used in relativistic Hartree calculations are real potentials. As such, only elastic rescattering contributions are taken into account. In general, strength from the incident beam is drained into unobserved inelastic channels, and one needs to incorporate this local absorption in the description of the reaction process. This is commonly done by adopting a complex or optical potential that is able to describe elastic scattering accompanied by absorption. The scattering wave function, expressed in terms of a partial-wave expansion in configuration space, reads

$$\Psi^{(+)}_{\vec{k}_f,m_s}(\vec{r}) = 4\pi\sqrt{\frac{E + M_N}{2E}}\sum_{\kappa\mu m} e^{-i\delta^*_\kappa} i^\ell \langle \ell m \frac{1}{2} m_s | j\mu\rangle Y_\ell^{m*}(\Omega_{k_f})\Psi^\mu_\kappa(\vec{r}) \ , \quad (2.58)$$

where $\Psi^{\mu}_{\kappa}(\vec{r})$ are four-spinors of form (2.51), with complex phase shifts and radial functions.

Not only are global parametrizations of Dirac optical potentials usually restricted to proton kinetic energies $T_p \leq 1$ GeV, calculations based on exact solutions of the Dirac equation frequently become impractical at higher energies. This is particularly the case for approaches relying on partial-wave expansions. At higher proton kinetic energies it appears more convenient to solve the equation (2.54) in the eikonal approximation (EA) [23, 71, 72, 73]. The EA belongs to the group of semi-classical approaches that become useful when the de Broglie-wavelength λ=$\hbar/k$ of the incident particle with momentum k is sufficiently short compared to the distance in which the potential varies appreciably. If the potential varies smoothly and has a range a, this short-wavelength condition is equivalent to the requirement that $ka \gg 1$. In addition one assumes that $|V_0|/E \ll 1$, with V_0 the typical strength of the potential and E the energy of the impinging particle. Since the potentials appearing in Eq. (2.53) vary smoothly and have an approximate range of $2-3$ fm, the condition to be fulfilled can then be written as $k \gg 500$ MeV/c or $T_p \gg 125$ MeV.

In the Dirac-eikonal approach, one postulates a phase-modification for the upper component of the plane wave:

$$u^{(+)}_{\vec{k}_f,m_s}(\vec{r}) \equiv e^{i\left(\vec{k}_f\cdot\vec{r}+\mathcal{S}(\vec{r})\right)}\chi_{\frac{1}{2}m_s} \ . \tag{2.59}$$

Inserting this ansatz into Eq. (2.54) will yield an expression for the eikonal phase $e^{i\mathcal{S}(\vec{r})}$. Here, we adopt the formalism depicted in Ref. [69]. We define the average momentum $\vec{K}$ and momentum transfer $\vec{\Delta}$ in terms of the proton's initial and final momentum $\vec{k}_i$ and $\vec{k}_f$, respectively,

$$\vec{K} = \frac{\vec{k}_f+\vec{k}_i}{2}, \tag{2.60}$$

$$\vec{\Delta} = \vec{k}_i - \vec{k}_f \ . \tag{2.61}$$

Within the context of the eikonal, or, equivalently the small-angle approximation ($\Delta/k_i \ll 1$), the following operational substitution is made in computing the scattering wave function [74]

$$\hat{p}^2 = [(\hat{\vec{p}}-\vec{K})+\vec{K}]^2 \longrightarrow 2\vec{K}\cdot\hat{\vec{p}} - K^2 \ . \tag{2.62}$$

As a result, Eq. (2.54) becomes a linear equation in the momentum operator, yielding a scattering wave function of the form

$$\psi^{(+)}_{\vec{k}_f,m_s} = \sqrt{\frac{E+M_N}{2M_N}} \begin{bmatrix} 1 \\ \frac{1}{E+M_N+V_s(r)-V_v(r)}\vec{\sigma}\cdot\hat{\vec{p}} \end{bmatrix} e^{i\vec{k}_f\cdot\vec{r}} e^{i\mathcal{S}(\vec{r})} \chi_{\frac{1}{2}m_s} \ , \tag{2.63}$$

where the eikonal phase reads ($\vec{r} \equiv (\vec{b}, z)$)

$$i\mathcal{S}(\vec{b},z) = -i\frac{M_N}{K}\int_{-\infty}^{z} dz' \left\{ V_c(\vec{b},z') + V_{so}(\vec{b},z')[\vec{\sigma}\cdot(\vec{b}\times\vec{K}) - iKz'] \right\} \ . \tag{2.64}$$

Hereby, the z-axis is defined along the direction of the "averaged" momentum $\vec{K}$. In this equation, the term iKz' is usually referred to as the Darwin term.

It is worth stressing that the eikonal phase can be obtained by performing a straight line integration along the direction of $\vec{K}$. A more accurate evaluation of the scattering wave function would in fact involve the calculation of its phase along the actual curved classical trajectory. We therefore expect that the eikonal method will be justified for small-angle collisions, or equivalently if the magnitude of the three-momentum transfer $|\vec{q}|$ is sufficiently large in comparison with the projected initial (or, missing) momentum of the ejectile (or, $q \gg p_m$=$|\vec{k}_f - \vec{q}|$).

The scattering wave function from Eq. (2.63) differs from the plane-wave solution in two respects. First, the lower component exhibits a dynamical enhancement since $V_s - V_v < 0$. Second, the eikonal phase $e^{i\mathcal{S}(\vec{r})}$ accounts for the interactions that the struck nucleon undergoes in its way out of the target nucleus. In intermediate-energy elastic $p-^{40}$Ca scattering ($T_p \approx 500$ MeV) the EA was shown to successfully reproduce the exact Dirac partial-wave result [71]. Bianconi and Radici showed that for ejectile momenta exceeding 1 GeV, the EA almost reproduced the ^{12}C$(e,e'p)$ differential cross sections obtained through performing a partial-wave expansion of the "exact" scattering wave function [75, 76].

Henceforth, the $A(e,e'p)$ results obtained with a scattering state of the form of Eq. (2.63) are dubbed as a relativistic optical-model eikonal approximation (ROMEA) calculation. It is important to note that in the actual calculation of the scattering state of Eq. (2.63), the impulse operator $\hat{\vec{p}}$ is replaced by $\vec{k}_f$, the momentum of the outgoing nucleon. This is equivalent to what in literature is usually referred to as the effective momentum approximation (EMA), in which the momentum operators

that appear in spinor-distortion operators are replaced by asymptotic kinematics [11]. We stress, however, that the dynamical enhancement of the lower components due to presence of the scalar and vector potentials is taken into account, and that spinor distortions in the bound-state wave functions are fully retained.

The eikonal phase of Eq. (2.64) reflects the accumulated effect of all interactions which the ejectile undergoes in its way out of the nucleus. All these effects are parametrized in terms of mean-field like optical potentials and the link with the elementary proton-proton and proton-neutron scattering is lost. In Glauber theory this link with the elementary processes will be reestablished.

2.4.2 Proton-nucleon scattering

First, let us consider a nucleon-nucleon scattering process and assume that it is governed by a local Lorentz and vector potential $V_s(r)$ and $V_v(r)$. The scattering amplitude corresponding with this process reads [71]

$$F_{m_s m_{s'}}(\vec{k}_i, \vec{k}_f, E) = -\frac{M_N}{2\pi} \left\langle \Psi^{(+)}_{\vec{k}_f, m_{s'}} \right| (\beta V_s + V_v) \left| \Phi_{\vec{k}_i, m_s} \right\rangle \ , \tag{2.65}$$

with $\Psi^{(+)}_{\vec{k}_f, m_{s'}}$ the relativistic scattered state as determined in Eq. (2.63), and the free Dirac solution

$$\Phi_{\vec{k}_i, m_s} = \sqrt{\frac{E + M_N}{2M_N}} \begin{bmatrix} 1 \\ \\ \frac{1}{E+M_N} \vec{\sigma} \cdot \hat{\vec{p}} \end{bmatrix} e^{i\vec{k}_i \cdot \vec{r}} \chi_{\frac{1}{2} m_s} \ . \tag{2.66}$$

After performing some algebraic manipulations, the scattering amplitude adopts the following form [71]

$$F_{m_s m_{s'}}(\vec{k}_i, \vec{k}_f, E) = \left\langle \chi_{s'} \left| F(\vec{k}_i, \vec{k}_f, E) \right| \chi_s \right\rangle \ , \tag{2.67}$$

where

$$F(\vec{k}_i, \vec{k}_f, E) = iK \int \frac{d\vec{b}}{2\pi} e^{i\vec{\Delta} \cdot \vec{b}} \Gamma(\vec{b}) \ . \tag{2.68}$$

In Eq. (2.68) the profile function has been introduced, according to

$$\Gamma(\vec{b}) = 1 - e^{i\chi(\vec{b})} \ , \tag{2.69}$$

with the phase-shift function given by

$$\chi(\vec{b}) = i\frac{M}{K}\int_{-\infty}^{\infty} dz \left\{ V_c(\vec{b},z) + V_{so}(\vec{b},z)[\vec{\sigma}\cdot(\vec{b}\times\vec{K})] \right\} . \tag{2.70}$$

Compared to Eq. (2.64), the Darwin term has vanished since it is an odd function of z.

In conventional Glauber theory the phase shift function $\chi(\vec{b})$ is not calculated on the basis of knowledge about the radial dependence and magnitude of the potentials $V_c(r)$ and $V_{so}(r)$, but is directly extracted from nucleon-nucleon scattering data. To cut a long story short, on the basis of Eq. (2.68) one manages to determine the profile function directly from nucleon-nucleon scattering data. This requires some extra manipulations which will be exposed below.

The most general form for the scattering amplitude in the NN center-of-mass system assuming parity conservation, time-reversal invariance, the Pauli principle, and isospin invariance can be written in terms of five invariant amplitudes [77]

$$\begin{aligned} F\left(\vec{\Delta}\right) = A\left(\vec{\Delta}\right) + B\left(\vec{\Delta}\right)(\vec{\sigma}_1+\vec{\sigma}_2)\cdot\hat{n} + C\left(\vec{\Delta}\right)(\vec{\sigma}_1\cdot\hat{n})(\vec{\sigma}_2\cdot\hat{n}) \\ + D\left(\vec{\Delta}\right)(\vec{\sigma}_1\cdot\hat{m})(\vec{\sigma}_2\cdot\hat{m}) + E\left(\vec{\Delta}\right)(\vec{\sigma}_1\cdot\hat{l})(\vec{\sigma}_2\cdot\hat{l}) . \end{aligned} \tag{2.71}$$

The nucleon spin operators are denoted by $\vec{\sigma}_1$ and $\vec{\sigma}_2$, and $\hat{n} \equiv \frac{\vec{k}_i\times\vec{k}_f}{|\vec{k}_i\times\vec{k}_f|}$, $\hat{m} \equiv \frac{\vec{k}_i-\vec{k}_f}{|\vec{k}_i-\vec{k}_f|}$, and $\hat{l} \equiv \frac{\vec{k}_i+\vec{k}_f}{|\vec{k}_i+\vec{k}_f|}$. The transferred momentum is denoted by $\vec{\Delta}$. Accordingly, the NN amplitude consists of a central term "A", a spin-orbit term "B" and three other spin-dependent terms. In principle, the amplitudes can be determined from a complete phase-shift analysis of NN data. For a long time, the small angle elastic scattering of protons with $k_p > 1$ GeV was assumed to be dominated by the central spin-independent amplitude. A very recent experiment performed at COSY/Jülich, however, provided indications for non-negligible spin-dependences at $k_p \approx 1.88$ GeV [78]. Unfortunately, today no theoretical model supplies a clear phenomenological understanding of the spin-dependence of the nucleon-nucleon interaction above 1 GeV [79]. In the analysis of proton-nucleus cross-section data, the spinless version of Glauber theory, including only the central part of the NN interaction, was very successful [18, 77, 80]. Albeit it has recently been shown that certain $A(e,e'p)$ interference responses might be sensitive to spin-dependent FSI [81, 82], in this work only the central amplitude will be retained.

As can be inferred from Fig. 2.6, the differential cross section for elastic pp scattering displays characteristic diffraction features which are closely related to Fraunhofer-diffraction patterns in optics. Diffraction phenomena appear because the wavelength of the incident particles is smaller than the dimension of the target particles. As in optical diffraction, the forward peak stands out clearly, and at t=0 ($t \equiv (k_f^\mu - k_i^\mu)^2$) the value of $d\sigma/dt$ is nearly independent of the incident momentum. Fig. 2.6 shows that the diffraction peak drops exponentially for many orders of magnitude. This behaviour suggests that at forward angles the cross section can be approximated by

$$\frac{d\sigma_{pN}^{el}}{dt} \approx \left.\frac{d\sigma_{pN}^{el}}{dt}\right|_{t=0} \exp\left(-\beta_{NN}^2 \mid t \mid\right) \ , \tag{2.72}$$

with β_{NN}^2 the slope parameter.

The diffractive behaviour gives rise to the following Gaussian parametrization for the central term of Eq. (2.71)

$$A(\vec{\Delta}) \equiv A(\vec{\Delta}=0) \exp\left(-\frac{\beta_{NN}^2 \Delta^2}{2}\right) \ . \tag{2.73}$$

The optical theorem $\mathrm{Im} f(\theta=0, \phi=0)$=$\frac{k\sigma_{tot}}{4\pi}$ leads then to

$$A(\vec{\Delta}) = \frac{k\sigma_{tot}^{NN}}{4\pi}(\epsilon_{NN}+i) \exp\left(-\frac{\beta_{NN}^2 \Delta^2}{2}\right) , \tag{2.74}$$

with ϵ_{NN} the ratio of the real to the imaginary part of the scattering amplitude.

Inverting Eq. (2.68) yields the following expression for the profile function

$$\Gamma\left(\vec{b}\right) \equiv 1 - e^{i\chi(\vec{b})} = \frac{\sigma_{tot}^{NN}(1-i\epsilon_{NN})}{4\pi\beta_{NN}^2} \exp\left(-\frac{\vec{b}^2}{2\beta_{NN}^2}\right) . \tag{2.75}$$

With the aid of this expression, the profile function can be determined directly from the elementary nucleon-nucleon scattering data. This constitutes the principle idea behind what is called "Glauber" theory. The three parameters which enter in Eq. (2.75) will be the subject of discussion in Section 2.4.4. First, we extend the above considerations to the issue of multiple-scattering events, and present a relativized version of Glauber theory.

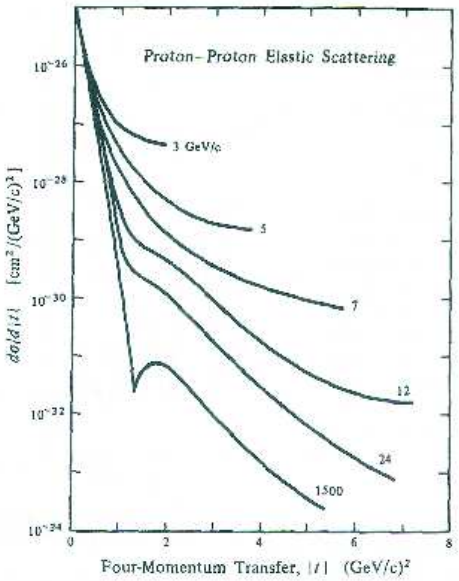

Figure 2.6 Differential cross section for elastic pp scattering. The parameter assigned to the curves gives the laboratory momentum of the incident protons. This figure was taken from Ref. [83].

2.4.3 Relativized Glauber model for $A(e, e'p)$

A major advantage of the eikonal approach relates to the fact that it can be easily extended to multiple-scattering events. Consider the $A(e, e'p)$ reaction, which was the subject of investigation at the start of this chapter. This situation is equivalent with the scattering of a fast ejected proton by a residual nucleus, composed of $A-1$ scatterers. We assume that the ejectile passes through the nucleus in a very short time so that variations in the positions of the residual nucleons can be ignored. This is the so-called frozen approximation. As stated above, we suppose that the ejectile interacts with the spectator nucleons by means of two-body spin-independent interactions. Exchange effects between the ejectile and the spectator nucleons are also neglected.

The Glauber scattering amplitude for multiple collisions leading from an initial

state $|i\rangle$ to a final state $|f\rangle$ is then given by

$$F_{multi}(\vec{\Delta}) = ik_f \int \frac{d\vec{b}}{2\pi} e^{i\vec{\Delta}\cdot\vec{b}} \langle f| 1 - e^{i\chi_{tot}(\vec{b},\vec{b}_2,\cdots,\vec{b}_A)} |i\rangle \ , \tag{2.76}$$

where $\vec{b}$ denotes the impact parameter of the struck proton and $(\vec{b}_2, \vec{b}_3, \cdots, \vec{b}_A)$ those of the frozen spectator nucleons in the target. The total Glauber phase-shift function

$$\chi_{tot}(\vec{b}, \vec{b}_2, \cdots, \vec{b}_A) = \sum_{j=2}^{A} \chi_j(\vec{b} - \vec{b}_j) \ , \tag{2.77}$$

is the sum of the phase shifts χ_i contributed by each of the spectator scatterers as the wave, representing the ejected nucleon, progresses through the residual nucleus. This property of so-called phase-shift additivity is a direct consequence of the one-dimensional nature of the relative motion, together with the neglect of three- and more-body forces, recoil effects and longitudinal momentum transfer. Furthermore, the expression of Eq. (2.76) is only a valid one for collisions for which the energy transfer is small compared to the incident particle energy. This is true for elastic collisions and for mildly inelastic ones in which the target is excited. It is not true for deep inelastic collisions in which the nature of the incident or target particles is modified or the number of particles is altered during the collision.

A similar introduction of the profile function as in Eq. (2.69) leads then to the following expression for the operator $\hat{\mathcal{S}}$, which represents the consecutive elastic or "mildly inelastic" collisions of the struck proton with the "frozen" nucleons,

$$\hat{\mathcal{S}}(\vec{r}, \vec{r}_2, \vec{r}_3, \cdots, \vec{r}_A) \equiv \prod_{j=2}^{A} \Big[1 - \Gamma(\vec{b} - \vec{b}_j)\theta(z_j - z)\Big] \ . \tag{2.78}$$

The step function $\theta(z_j - z)$ guarantees that the struck particle can only interact with the spectator protons and neutrons which it finds in its forward propagation path.

The antisymmetrized A-body wave function in the final state reads now

$$\Psi_A^{\vec{k}_f, m_s}(\vec{r}, \vec{r}_2, \vec{r}_3, \cdots, \vec{r}_A) \backsim \hat{\mathcal{A}} \Bigg[\hat{\mathcal{S}}(\vec{r}, \vec{r}_2, \vec{r}_3, \cdots, \vec{r}_A) \begin{bmatrix} 1 \\ \frac{1}{E+M_N}\vec{\sigma}\cdot\vec{p} \end{bmatrix} e^{i\vec{k}_f\cdot\vec{r}} \chi_{\frac{1}{2}m_s} \times \Psi_{A-1}^{J_R M_R}(\vec{r}, \vec{r}_2, \vec{r}_3, \cdots, \vec{r}_A) \Bigg] \ , \tag{2.79}$$

where $\vec{r}(\vec{b},z)$ denotes the position of the struck particle and $(\vec{r}_2,\vec{r}_3,\cdots,\vec{r}_A)$ those of the frozen spectator protons and neutrons in the target. $\Psi_{A-1}^{J_R M_R}$ is the wave function characterizing the state in which the $A-1$ nucleus is created and $\hat{\mathcal{A}}$ is the antisymmetrization operator. Here, the dynamical enhancement of the lower component which appeared in Eq. (2.63) has been omitted since $E+M_N \gg |V_s - V_v|$ at the intermediate energies embodied in this work.

The Dirac-Glauber $A(e,e'p)$ transition amplitude of Eq. (2.8) can be written as

$$\begin{aligned}\langle J^\mu \rangle &= \int d\vec{r} \int d\vec{r}_2 \cdots \int d\vec{r}_A \left(\Psi_A^{\vec{k}_f, m_s}(\vec{r},\vec{r}_2,\vec{r}_3,\cdots,\vec{r}_A) \right)^\dagger \\ &\times \gamma^0 J^\mu(r) e^{i\vec{q}\cdot\vec{r}} \Psi_A^{gs}(\vec{r},\vec{r}_2,\vec{r}_3,\cdots,\vec{r}_A) \,, \end{aligned} \tag{2.80}$$

where for convenience only the spatial coordinates are explicitly written. For the sake of brevity of the notations, in the forthcoming derivations we consider the case A=3. A generalization to arbitrary mass number A is rather straightforward. The initial A-nucleon wave function is constructed within the context of a mean-field picture, and is thus of the Slater-determinant form

$$\Psi_A^{gs}(\vec{r}_1,\vec{r}_2,\vec{r}_3) = \frac{1}{\sqrt{A!}} \begin{vmatrix} \phi_{\alpha_1}(\vec{r}_1) & \phi_{\alpha_2}(\vec{r}_1) & \phi_{\alpha_3}(\vec{r}_1) \\ \phi_{\alpha_1}(\vec{r}_2) & \phi_{\alpha_2}(\vec{r}_2) & \phi_{\alpha_3}(\vec{r}_2) \\ \phi_{\alpha_1}(\vec{r}_3) & \phi_{\alpha_2}(\vec{r}_3) & \phi_{\alpha_3}(\vec{r}_3) \end{vmatrix} . \tag{2.81}$$

For spherically symmetric potentials, the solutions $\phi_\alpha(\vec{r})$ to a single-particle Dirac equation entering this Slater determinant have the form of Eq. (2.51).

The final A-body wave function reads

$$\Psi_A^{\vec{k}_f, m_s}(\vec{r}_1,\vec{r}_2,\vec{r}_3) = \frac{1}{\sqrt{A!}} \begin{vmatrix} \hat{\mathcal{S}}(\vec{r}_1,\vec{r}_2,\vec{r}_3)\phi_{k_f m_s}(\vec{r}_1) & \phi_{\alpha_2}(\vec{r}_1) & \phi_{\alpha_3}(\vec{r}_1) \\ \hat{\mathcal{S}}(\vec{r}_2,\vec{r}_1,\vec{r}_3)\phi_{k_f m_s}(\vec{r}_2) & \phi_{\alpha_2}(\vec{r}_2) & \phi_{\alpha_3}(\vec{r}_2) \\ \hat{\mathcal{S}}(\vec{r}_3,\vec{r}_1,\vec{r}_2)\phi_{k_f m_s}(\vec{r}_3) & \phi_{\alpha_2}(\vec{r}_3) & \phi_{\alpha_3}(\vec{r}_3) \end{vmatrix} . \tag{2.82}$$

Relative to the target nucleus ground state written in Eq. (2.81), the wave function of Eq. (2.82) refers to the situation whereby the struck proton resides in a state "α_1", leaving the residual $A-1$ nucleus as a hole state in that particular single-particle level.

Adopting the IA, the nuclear current is a one-body operator. As both the initial and final wave functions are fully antisymmetrized, one can choose the operator J^μ to act on one particular coordinate and write without any loss of generality

$\left(\vec{r}' \equiv \left(\vec{b}'(x',y'),z'\right)\right)$

$$\begin{aligned}\langle J^\mu\rangle = \;& A\;\frac{1}{A!}\int d\vec{r}'\int d\vec{r}_2'\int d\vec{r}_3' \sum_{k,l,m\,\in\,\{k_f m_s,\alpha_2,\alpha_3\}}\;\sum_{n,o,p\,\in\,\{\alpha_1,\alpha_2,\alpha_3\}} \epsilon^*_{klm}\epsilon_{nop}\\ &\times\;\phi_k^\dagger(\vec{r}')\phi_l^\dagger(\vec{r}_2')\phi_m^\dagger(\vec{r}_3')e^{i\vec{q}\cdot\vec{r}'}\gamma^0\\ &\times\;J^\mu(\vec{r}')\left[1-\theta(z_2'-z')\Gamma(\vec{b}_2'-\vec{b}')\right]^\dagger\left[1-\theta(z_3'-z')\Gamma(\vec{b}_3'-\vec{b}')\right]^\dagger\\ &\times\;\phi_n(\vec{r}')\phi_o(\vec{r}_2')\phi_p(\vec{r}_3')\;, \end{aligned}\tag{2.83}$$

with ϵ_{ijk} the Levi-Civita symbol, and where we have introduced a frame (x',y',z') defined by the following unit vectors

$$\hat{z}' = \frac{\vec{k}_f}{\mid\vec{k}_f\mid}\quad,\quad \hat{y}' = \frac{\vec{k}_f\times\vec{q}}{\mid\vec{k}_f\times\vec{q}\mid}\quad,\quad \hat{x}' = \hat{z}'\times\hat{y}'\;. \tag{2.84}$$

In this way, the z'-axis lies along the direction of the ejectile and the (x',z') plane coincides with what is usually known as the hadronic reaction plane in $A(e,e'p)$ reactions.

Assuming that the profile function Γ does not contain spin-dependent terms, one can safely make the following approximation for elastic and mildly inelastic scatterings

$$\begin{aligned}&\int d\vec{r}'\;\int d\vec{r}_2'\phi_k^\dagger(\vec{r}')\phi_l^\dagger(\vec{r}_2')J^\mu(\vec{r}')\left[1-\theta(z_2'-z')\Gamma(\vec{b}_2'-\vec{b}')\right]^\dagger\phi_n(\vec{r}')\phi_o(\vec{r}_2')\\ &\quad\approx\;\delta_{lo}\int d\vec{r}'\int d\vec{r}_2'\phi_k^\dagger(\vec{r}')J^\mu(\vec{r}')\\ &\quad\times\;\left[1-\theta(z_2'-z')\Gamma(\vec{b}_2'-\vec{b}')\right]^\dagger\phi_n(\vec{r}')|\phi_o(\vec{r}_2')|^2\;. \end{aligned}\tag{2.85}$$

Inserting this in Eq. (2.83) yields

$$\begin{aligned}\langle J^\mu\rangle = \;& A\;\frac{1}{A!}\int d\vec{r}'\int d\vec{r}_2'\int d\vec{r}_3' \sum_{l,m\,\in\,\{\alpha_2,\alpha_3\}}\epsilon^*_{(k_f m_s)lm}\epsilon_{\alpha_1 lm}\\ &\times\;\phi^\dagger_{k_f m_s}(\vec{r}')|\phi_l(\vec{r}_2')|^2|\phi_m(\vec{r}_3')|^2e^{i\vec{q}\cdot\vec{r}'}\gamma^0J^\mu(\vec{r}')\phi_{\alpha_1}(\vec{r}')\\ &\times\;\left[1-\theta(z_2'-z')\Gamma(\vec{b}_2'-\vec{b}')\right]^\dagger\left[1-\theta(z_3'-z')\Gamma(\vec{b}_3'-\vec{b}')\right]^\dagger\;. \end{aligned}\tag{2.86}$$

This leads to our final result for the Dirac-Glauber $A(e,e'p)$ transition amplitude

$$\langle J^\mu\rangle \;=\; \int d\vec{r}\phi^\dagger_{k_f m_s}(\vec{r})\,\mathcal{G}^\dagger(\vec{b},z)\gamma^0J^\mu(\vec{r})e^{\imath\vec{q}\cdot\vec{r}}\phi_{\alpha_1}(\vec{r})\;, \tag{2.87}$$

where the Dirac-Glauber phase $\mathcal{G}(\vec{b},z)$ is defined in the following fashion

$$\mathcal{G}(\vec{b},z)=\prod_{\alpha_{occ}\neq\alpha}\left[1-\int d\vec{r}'\left|\phi_{\alpha_{occ}}\left(\vec{r}'\right)\right|^2\theta\left(z'-z\right)\Gamma\left(\vec{b}'-\vec{b}\right)\right]. \tag{2.88}$$

Here, the product extends over all nucleon states, but for the one from which the detected nucleon was emitted. The entire effect of FSI is contained in the phase $\mathcal{G}(\vec{b},z)$.

The numerical evaluation of the Glauber phase $\mathcal{G}(\vec{b},z)$ is rather challenging if no additional approximations are introduced. A Monte Carlo integration method was suggested in Ref [84]. In our numerical calculations we did not introduce any further approximations and found it most appropriate to evaluate the scattering amplitudes and Glauber phases in the frame defined by the unit vectors of Eq. (2.84). Inserting the expression for the Dirac single-particle wave functions ϕ_α of Eq. (2.51) in the Eq. (2.88) for the Glauber phase, one gets ($d\vec{r}'\equiv dz'b'db'd\phi_{b'}$)

$$\begin{aligned}\mathcal{G}(\vec{b},z) \equiv \mathcal{G}(b,z)=\prod_{\alpha_{occ}\neq\alpha}\Bigg\{1-\frac{\sigma_{pN}^{tot}(1-i\epsilon_{pN})}{4\pi\beta_{pN}^2}\int_0^\infty b'db'\int_{-\infty}^{+\infty}dz'\theta(z'-z)\\ \left(\left[\frac{G_{n\kappa}\left(r'(b',z')\right)}{r'(b',z')}\mathcal{Y}_{\kappa m}(\Omega',\sigma)\right]^2+\left[\frac{F_{n\kappa}\left(r'(b',z')\right)}{r'(b',z')}\mathcal{Y}_{\kappa m}(\Omega',\sigma)\right]^2\right)\\ \times\exp\left[-\frac{(b-b')^2}{2\beta_{pN}^2}\right]\int_0^{2\pi}d\phi_{b'}\exp\left[\frac{-bb'}{\beta_{pN}^2}2\sin^2\left(\frac{\phi_b-\phi_{b'}}{2}\right)\right]\Bigg\}.\end{aligned} \tag{2.89}$$

Standard numerical integration techniques were adopted to evaluate the integrals occurring in this equation. It is important to remark that cylindrical symmetry about the z'-axis makes the above expression independent of ϕ_b. As a result, the relativistic Glauber phase depends on only two independent variables (b,z). Unfortunately, this cylindrical symmetry prohibits any meaningful use of a partial-wave expansion technique to solve the Dirac equation of the ejectile. Instead, the multi-dimensional integrals are computed numerically. In the above expression (2.89), each of the frozen spectator nucleons is identified by its quantum numbers (n,κ,m) and its corresponding Dirac wave function $\phi_{n\kappa m}(\vec{r},\vec{\sigma})$.

Henceforth, the $A(e,e'p)$ results obtained with a scattering state of the form of Eq. (2.79) are dubbed as a relativistic multiple-scattering Glauber approximation (RMSGA) calculation [69]. Now that we are provided with a model, still attention

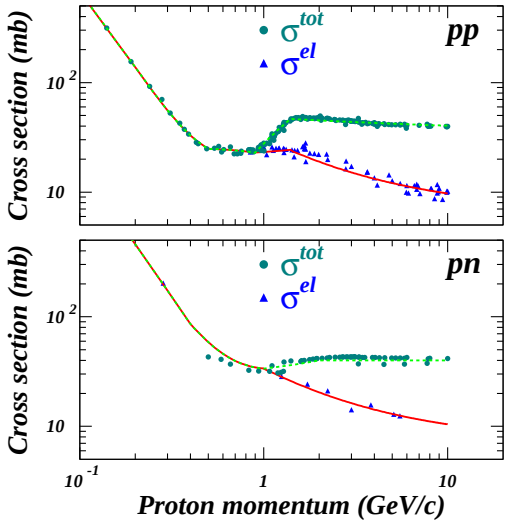

Figure 2.7 Total and elastic cross sections for proton-proton and proton-neutron scattering as a function of the proton lab momentum. The data are from Ref. [85]. The solid (dashed) curve displays our global fit to the elastic (total) cross section.

need to be paid to the nucleon-nucleon scattering parameters which underly the complete concept of Glauber theory.

2.4.4 Glauber parameters

It is worth stressing that in contrast to the RDWIA models, all parameters entering the calculation of the scattering states in the RMSGA $A(e,e'p)$ model can be directly determined from the elementary proton-proton and proton-neutron scattering data. In practice, for a given ejectile's lab momentum $\mid \vec{k}_f \mid$ the following input is required : the total proton-proton σ_{pp}^{tot} and proton-neutron σ_{pn}^{tot} cross sections, the corresponding slope parameters (β_{pp}^2 and β_{pn}^2) and the ratios of the real to imaginary part of the scattering amplitude (ϵ_{pp} and ϵ_{pn}). We obtain the numbers σ_{pN}^{tot}, β_{pN}^2 and ϵ_{pN} through interpolation of the data base available from the Particle Data Group [85]. The fitting functions employed in our formalism are displayed in Table 2.2. Fig. 2.7 displays the total and elastic cross sections for proton-proton and proton-neutron scattering as a function of the proton lab momentum.

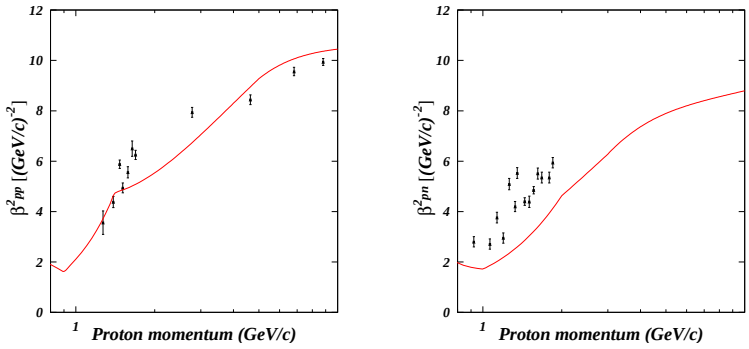

Figure 2.8 The Glauber slope parameters β^2_{pp} and β^2_{pn} as obtained from Eq. (2.90) with the global fits contained in Fig. 2.7. The data are from Refs. [86] (proton-neutron) and [87] (proton-proton) and are determined from the small-angle t dependence of the measured differential cross sections.

In high-energy proton-proton scattering, it is known that the total reaction cross section varies slowly with the proton lab momentum. Most of the inelastic cross section goes into the production of mesons. The slope parameters β^2_{pp} and β^2_{pn} may be found by analyzing the shape of the differential cross sections assuming that the contribution from the spin-dependent terms is negligible. At proton momenta $p_p \leq 1$ GeV the slope parameters found directly from experiment and phase-shift analysis differ significantly due to a large contribution from the spin-dependent scattering amplitude [77]. At higher energies this difference drops quickly indicating that spin effects are small in that region. Values for the slope parameters below 1 GeV are scarce and not free of ambiguities. Therefore, in our calculations, the slope parameters are obtained from the ratio of the elastic σ^{el}_{pN} to the total σ^{tot}_{pN} cross section through the following relation

$$\beta^2_{pN} \approx \frac{\left(\sigma^{tot}_{pN}\right)^2 \left(\epsilon^2_{pN}+1\right)}{16\pi\sigma^{el}_{pN}} \,. \tag{2.90}$$

In Fig. 2.8 we compare the slope parameters obtained through this formulae with those extracted directly from the t-dependence of the differential pN cross sections. The curves in Fig. 2.8 use the above formulae (2.90) and our global fits to σ^{tot}_{pN}, σ^{el}_{pN} and ϵ_{pN} shown in Figs. 2.7 and 2.9. For proton-proton scattering the

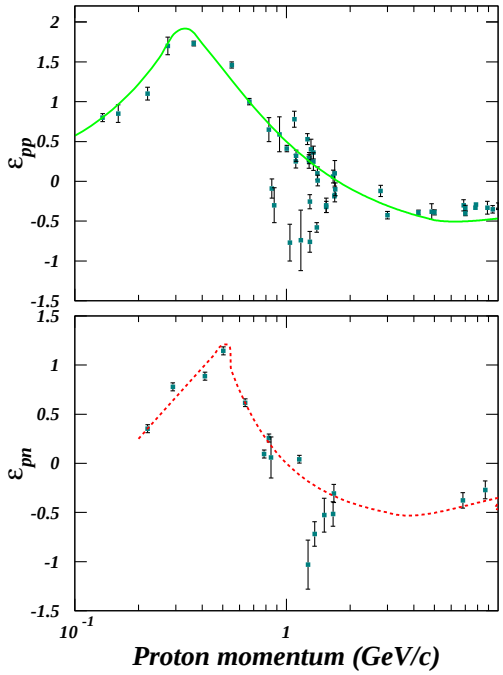

Figure 2.9 The ratios of the real to imaginary parts of the central amplitude f^c_{pN} for proton-proton and proton-neutron scattering as a function of the proton lab momentum. The curves are our global fits to the data points. The data are from the review paper of Ref. [77].

situation emerges to be very satisfactory.

2.5 The Dirac-Glauber phase: numerical results

This section is devoted to a presentation of results for the Dirac-Glauber phase of Eq. (2.88) for the nuclei ^{4}He, ^{12}C, ^{56}Fe and ^{208}Pb. First, we investigate how many rescatterings a proton undergoes during its escape. To this end, we estimate the contribution of single- and multiple-scattering events for the target nuclei ^{4}He, ^{12}C and ^{208}Pb. Next, attention is paid to the role of relativistic effects when computing the impact of FSI. Finally, the validity of a frequently adopted approximation, namely the replacement of the squared nucleon wave functions by some average nuclear density, is investigated.

Parameter	Fitting function	Energy range
σ_{pp}^{tot}(mb)	$48 + 0.522(\ln k_f)^2 - 4.51 \ln k_f$	$k_f > 1.4$
	$23 + 47.1(k_f - 0.9)$	$0.9 < k_f \leq 1.4$
	$25 - 5(k_f - 0.5)$	$0.5 < k_f \leq 0.9$
	$\frac{8.667}{k_f^2} - \frac{23.114}{k_f} + 36.559$	$k_f \leq 0.5$
σ_{pn}^{tot}(mb)	40	$k_f > 2.0$
	$33.7 + 6.3(k_f - 1)$	$1.0 < k_f \leq 2.0$
	$\frac{19.7}{k_f^2} - \frac{34.083}{k_f} + 48.083$	$0.4 < k_f \leq 1.0$
	$\frac{26.426}{k_f^2} - \frac{48.595}{k_f} + 42.325$	$k_f \leq 0.4$
σ_{pp}^{el}(mb)	$11.9 + 26.9 k_f^{-1.21} + 0.169(\ln k_f)^2 - 1.85 \ln k_f$	$k_f > 1.7$
	$23 + 2.65(k_f - 0.9)$	$0.9 < k_f \leq 1.7$
	$25 - 5(k_f - 0.5)$	$0.5 < k_f \leq 0.9$
	$\frac{8.667}{k_f^2} - \frac{23.114}{k_f} + 36.559$	$k_f \leq 0.5$
σ_{pn}^{el}(mb)	$31 - 10.85 \ln k_f$	$k_f > 1.0$
	$\frac{19.7}{k_f^2} - \frac{34.083}{k_f} + 48.083$	$0.4 < k_f \leq 1.0$
	$\frac{26.426}{k_f^2} - \frac{48.595}{k_f} + 42.325$	$k_f \leq 0.4$
ϵ_{pp}	$\frac{-0.18}{k_f^2} + \frac{1.45}{k_f} - 0.77$	$k_f > 0.32$
	$0.8 + 6.49(k_f - 0.135)$	$k_f \leq 0.32$
ϵ_{pn}	$\frac{6.61}{k_f^2} - \frac{3.51}{k_f} - 0.0655$	$k_f > 3.0$
	$\frac{0.27}{k_f^2} + \frac{0.39}{k_f} - 0.66$	$0.5 < k_f \leq 3.0$
	$0.25 + 1.04(\ln k_f + 1.61)$	$k_f \leq 0.5$

Table 2.2 Fitting functions for σ_{NN}^{tot},σ_{NN}^{el} and ϵ_{NN} as a function of the ejectile's lab momentum $|\vec{k}_f|$. This latter one is given in units of (GeV/c).

2.5.1 Single- and multiple-scattering

One popular approximation in Glauber-inspired $A(e,e'p)$ calculations, is expanding the A-body operator $\hat{\mathcal{S}}(\vec{r},\vec{r}_2,\vec{r}_3,\cdots,\vec{r}_A)$ of Eq. (2.78)

$$\begin{aligned}
&\hat{\mathcal{S}}(\vec{r},\vec{r}_2,\vec{r}_3,\cdots,\vec{r}_A) \\
&\quad = 1-\sum_{j=2}^{A}\theta(z_j-z)\Gamma(\vec{b}-\vec{b}_j)+\sum_{j\neq k}^{A}\theta(z_j-z)\Gamma(\vec{b}-\vec{b}_j)\theta(z_k-z)\Gamma(\vec{b}-\vec{b}_k) \\
&\quad - \sum_{j\neq k\neq l=2}^{A}\theta(z_j-z)\Gamma(\vec{b}-\vec{b}_j)\theta(z_k-z)\Gamma(\vec{b}-\vec{b}_k)\theta(z_l-z)\Gamma(\vec{b}-\vec{b}_l) \\
&\quad + \cdots,
\end{aligned} \tag{2.91}$$

and truncating it at some order in Γ. In the above expression, the unity operator (first term) refers to "free passage" of the hit proton. The second term, which is linear in the profile function, reflects the situation whereby the struck nucleon scatters on one single spectator nucleon before turning asymptotically free (single-scattering process). Higher-order terms in the expression account for processes whereby the ejected proton subsequently scatters with two, three, ... , $A-1$ spectator nucleons. In many works, only a limited amount of terms in the expansion of Eq. (2.91) is retained. Often, the operator $\hat{\mathcal{S}}$ is replaced by the term which is first order in Γ. As a result, the FSI effects can be treated with the aid of one-body operators. Here, we wish to compare Glauber phases obtained with the exact operator with those that are produced when allowing only single scatterings. We wish to remind the reader that the Glauber phase, as it was defined in Eq. (2.88) depends on the two variables (b,z) and is independent of ϕ_b.

In Figs. 2.10, 2.11, 2.12 results are displayed for the computed real and imaginary part of the Glauber phase

$$\mathcal{G}(r,\theta)=\mathcal{G}\left(b=\sqrt{r^2-r^2\cos^2\theta},z=r\cos\theta\right), \tag{2.92}$$

corresponding with proton emission from the Fermi level for the target nuclei ^{4}He, ^{12}C and ^{208}Pb and θ=0^o. The radial coordinate r denotes the distance relative to the center of the target nucleus, whereas θ defines the polar angle with respect to the axis defined by the asymptotic momentum of the ejected particle. The Glauber phase at a peculiar value (r,θ) gives a measure of the FSI mechanisms which the hit

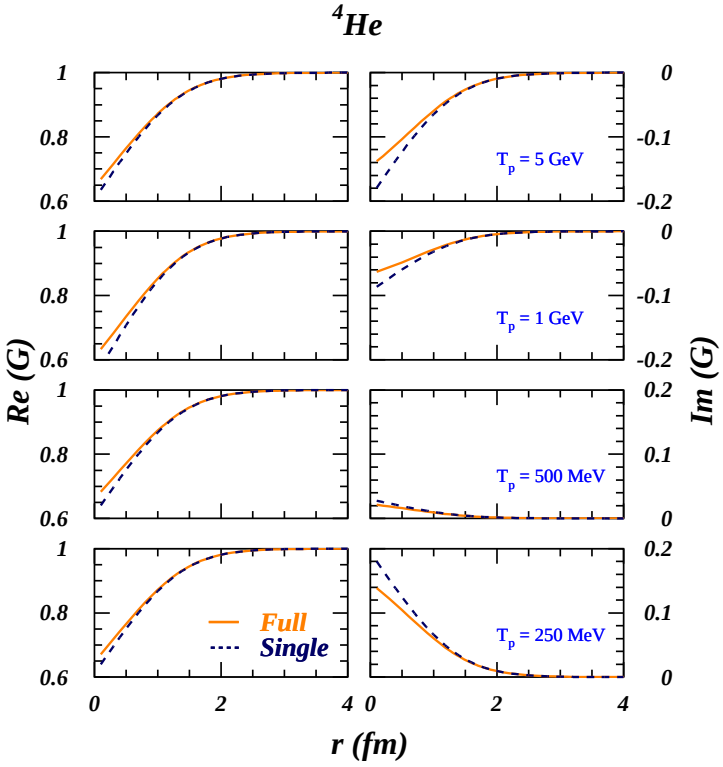

Figure 2.10 The radial dependence of the real and imaginary part of the computed Glauber phase $\mathcal{G}$ along the direction of the ejected particle ($\theta = 0°$) for proton emission from ^{4}He at various proton kinetic energies T_p. Results with the expression of Eq. (2.91) truncated to the first order in Γ (dashed line) are compared to the full result (solid line).

nucleon will undergo when the photon hits it at that position. We remind that in the absence of FSI the real part of $\mathcal{G}$ equals one, whereas the imaginary part vanishes identically. As becomes clear from Fig. 2.10, for a ^{4}He nucleus the single-scattering contributions give an adequate description for the real part of the Glauber phase, whereas the effect of higher-order scattering effects in the imaginary part is of the order of 5%. Multiple-scattering effects are particularly prominent for nucleons that are located near the center of the nucleus. In Fig. 2.13 we study the effect of multiple-scattering events on the ^{4}He$(e, e'p)$ differential cross sections, which is displayed as a function of the missing momentum at three different values of

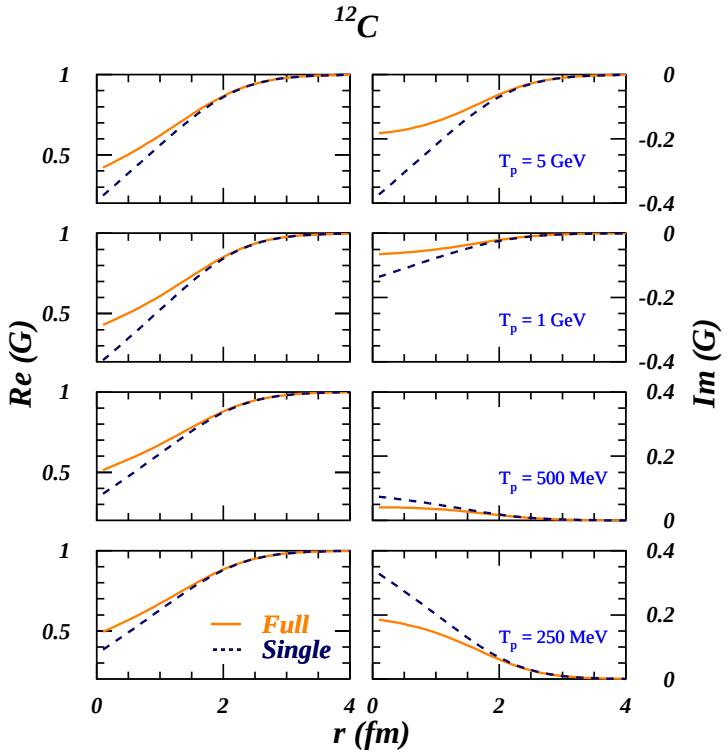

Figure 2.11 As in Fig. 2.10 but now for protons ejected from the Fermi-level (1p3/2) in ^{12}C.

Q^2. Apparently, only the high p_m-region is affected by the truncation to single-scattering contributions. This illustrates that the nucleons subject to the strongest FSI mechanisms are ejected from the center of the nucleus. The overall effect of the full Glauber phase is an estimated 10% reduction for the ^{4}He$(e,e'p)$ plane-wave cross section. This value is in line with the numbers obtained in Ref. [88].

It is clear that for a light nucleus like ^{4}He the average number of rescatterings can be inferred to be of the order of one. For a given ejectile's momentum, the average number of scatterers which it encounters in its way out of the nucleus is expected to grow like $A^{1/3}$. Given that for A=4 single scattering contributions provide a good description of FSI, one can infer that for a heavy nucleus like ^{208}Pb convergence of Eq. (2.91) is not reached until including quadruple-scattering terms. This

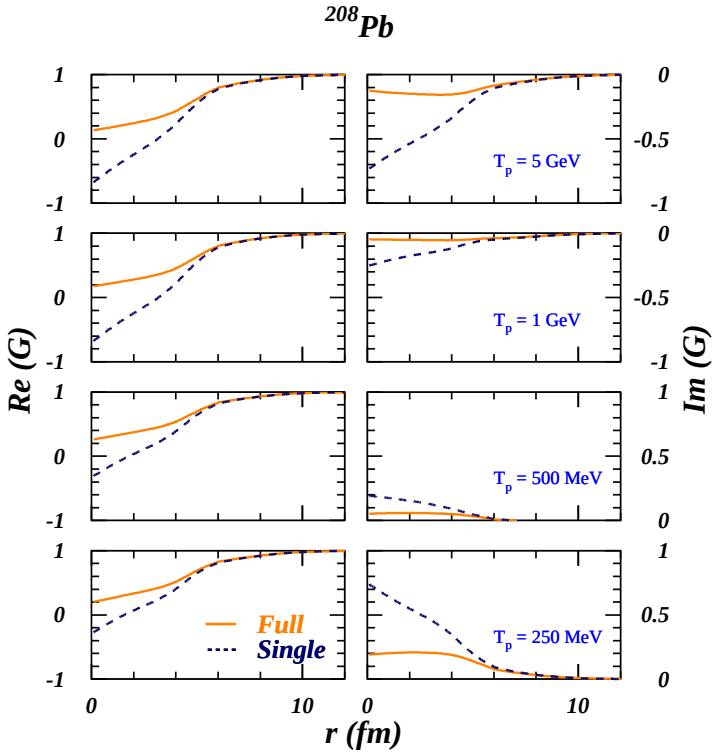

Figure 2.12 As in Fig. 2.10 but now for protons ejected from the Fermi-level in ^{208}Pb

complies with the results of calculations by various authors, see, e.g., Table 1 of Ref. [26]. Since the truncation to first order appears as a rather questionable procedure, all further results will be obtained with the "full" Glauber A-body operator of Eq. (2.78).

Figs. 2.10,2.11, 2.12 reveal that single-scattering events dominate the real and imaginary part of the Glauber phase at the nuclear surface. However, in the interior of the nucleus, subsequent orders in the scattering terms come with opposite signs for all target nuclei studied. As such, a truncation to single-scattering terms would yield a sizeable overestimation of the FSI effects, even for a nucleus like ^{12}C. The real part of $\mathcal{G}$ exhibits little T_p dependence over the energy range covered in the figures. The imaginary part, on the other hand, changes sign as one exceeds T_p=0.5

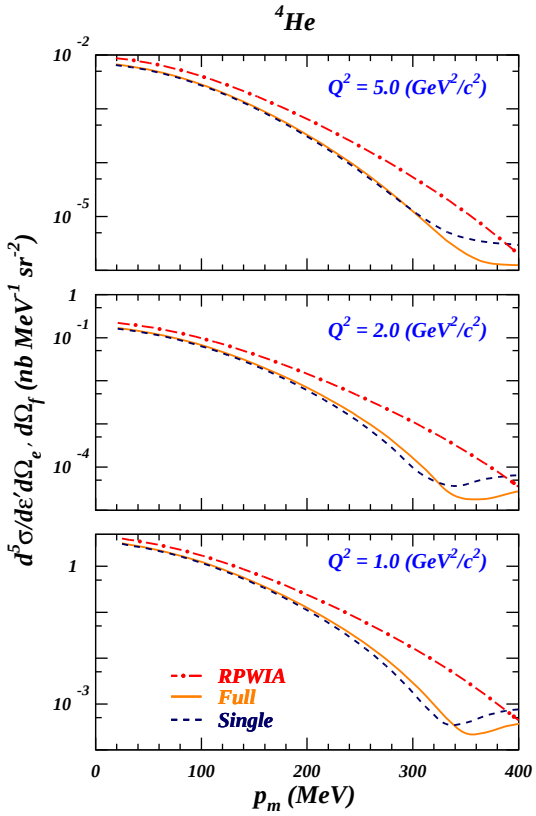

Figure 2.13 The ^{4}He$(e,e'p)$ differential cross section as a function of the missing momentum at three different values of Q^2. Results with the expression of Eq. (2.91) truncated to the first order in Γ (dashed line) are compared to the full result (solid line). The dot-dashed lines show the RPWIA results.

GeV and enters a highly inelastic regime. This observed change in the relative sign between the real and imaginary parts of the Glauber phase is governed by the T_p dependence of the parameters ϵ_{pp} and ϵ_{pn} as is shown in Fig. 2.9.

The figures 2.10-2.12 display effects stemming from FSI along the direction defined by the asymptotic momentum of the ejectile (θ=0^o). However, for a given r, the Glauber phase has an additional non-trivial dependence on the polar angle θ. Fig. 2.15 illustrates the computed radial and polar-angle dependence of the real and imaginary part of the Dirac-Glauber phase for 1 GeV protons ejected from the

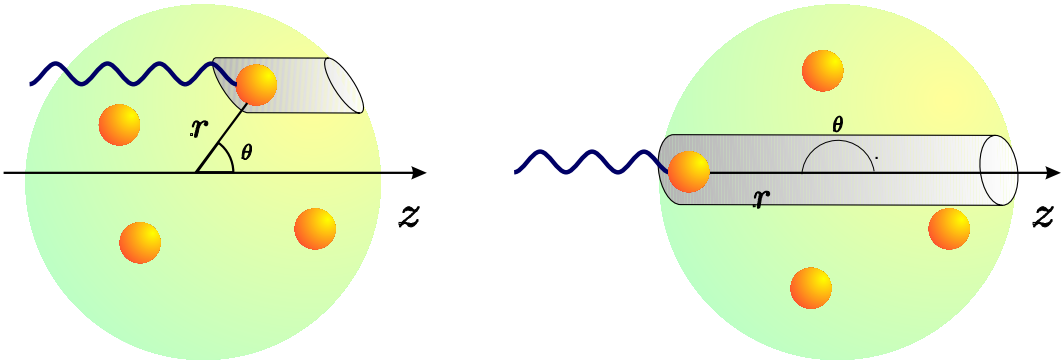

Figure 2.14 A schematic representation of the radial and polar-angle dependence of FSI. The proton is subject to FSI in a cone about the momentum transfer (grey-shaded areas). The left figure corresponds with a situation where the photon hits the nucleon in the forward hemisphere with respect to the direction defined by $\vec{k}_f$. The right figure refers to the peculiar event whereby θ=180^o.

Fermi level in ^{4}He and ^{56}Fe. Our expectations for heavier nuclei, i.e. the more nucleons in the nuclei, the larger the profile function and the smaller the Glauber phase $\mathcal{G}$, are clearly confirmed. To guide the eye, Fig. 2.14 gives a schematic representation of the situation. The grey-shaded areas refer to that part of the nucleus where the ejectile is subject to FSI. Here, $0^o \leq \theta \leq 90^o$ ($90^o \leq \theta \leq 180^o$) refers to a situation where the photon hits the nucleon in the forward (backward) hemisphere with respect to the direction defined by $\vec{k}_f$. The $\theta = 180^o$ case corresponds with a peculiar event whereby the photon couples to the proton along the direction defined by $-\vec{k}_f$. For $\theta = 180^o$ and increasing r, the photon initially hits the proton at the outskirts of the target nucleus and the proton has to travel through the whole nucleus before it becomes asymptotically free at the opposite side. It speaks for itself that these kinematical situations induce the largest FSI effects but cannot be expected to provide large contributions to the integrated matrix elements.

2.5.2 Relativity

One measure for the role of relativity in the description of the FSI can be estimated by neglecting the lower components $F_{n\kappa}(r)$ in the relativistic wave functions for the individual scattering nucleons in Eq. (2.88) and comparing it to the exact result. We have performed several of these calculations for a variety of target nuclei. In

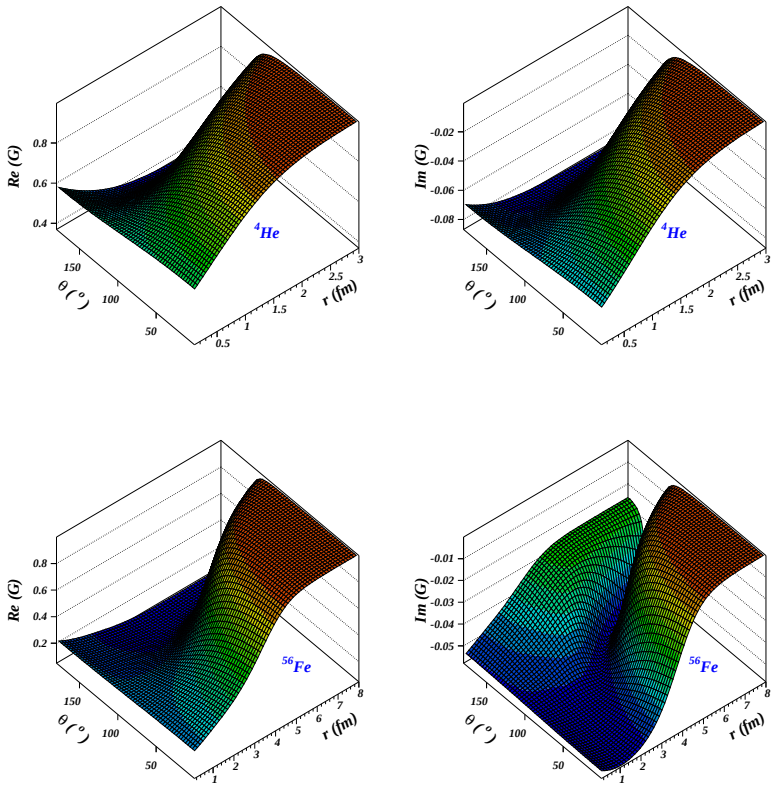

Figure 2.15 The computed radial and polar-angle dependence of the real and imaginary part of the Dirac-Glauber phase for protons with T_p=1000 MeV ejected from the Fermi level. The upper (lower) panels correspond to ^{4}He (^{56}Fe).

Fig. 2.16, the ratio of the "relativistic" to the "non-relativistic " Glauber phase is displayed for 1 GeV proton emission out of ^{12}C. In general, the relativistic lower wave-function components for the scattering centers (i.e. the nucleons residing in the daughter nucleus) are observed to have a minor impact on the predictions for both the real and imaginary part of the Glauber phase. However, it is well-known that the inclusion of the lower relativistic components is essential for some $A(e, e'p)$ observables [89, 90]. From the results presented here, it can be excluded that this could be attributed to a relativistic effect in the description of the final-state interactions.

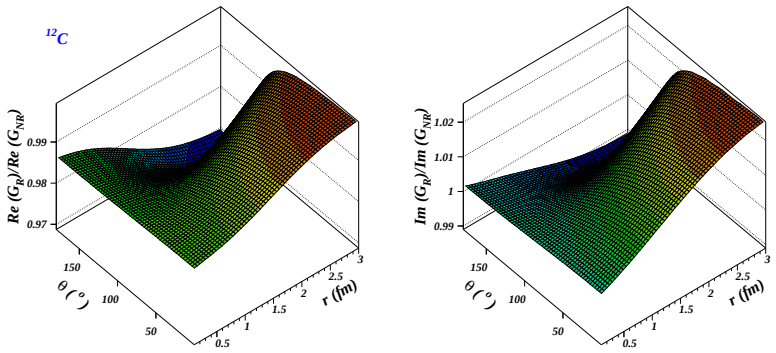

Figure 2.16 The effect of the lower components in the wave functions for the scattering centers on the computed Glauber phase $\mathcal{G}$ at $T_p = 1$ GeV for proton emission out of ^{12}C. The figures display the ratio of the "relativistic" to the "non-relativistic" Glauber phase of Eq. (2.88).

2.5.3 The thickness approximation

Most Glauber-based calculations performed within the framework of the independent particle model , introduce an additional averaging over the positions of the spectator nucleons. This procedure amounts to replacing in Eq. (2.88) the characteristic spatial distributions of each of the spectator nucleons described by the functions $F_{n\kappa}(r)$ and $G_{n\kappa}(r)$ by an average density distribution for the target nucleus

$$\mathcal{G}(\vec{b},z) \approx \mathcal{G}_T(\vec{b},z) = \left\{1 - \frac{\sigma_{NN}^{tot}(1-i\epsilon_{NN})}{4\pi\beta_{NN}^2}\int_0^\infty b'db'T_B(b',z)\exp\left[-\frac{(b-b')^2}{2\beta_{NN}^2}\right]\right.$$
$$\left.\times \int_0^{2\pi} d\phi_{b'}\exp\left[\frac{-2bb'}{\beta_{NN}^2}\sin^2\left(\frac{\phi_b-\phi_{b'}}{2}\right)\right]\right\}^{A-1}. \quad (2.93)$$

Henceforth, we will refer to this approximated Glauber phase as $\mathcal{G}_T$. The function $T_B(b',z)$ which was introduced in the above expressions is known as the "thickness function" and reads

$$T_B(b',z) = \frac{1}{A}\int_{-\infty}^{+\infty} dz'\theta(z'-z)\rho_B(r'(b',z')), \quad (2.94)$$

where the relativistic radial baryon density $\rho_B(r)$ is defined in the standard fashion

$$\begin{aligned}\rho_B(r) &\equiv \langle\overline{\Psi_A^{gs}}\gamma_0\Psi_A^{gs}\rangle = \sum_\alpha \int d\vec{\sigma}d\Omega(\phi_\alpha(\vec{r},\vec{\sigma}))^\dagger(\phi_\alpha(\vec{r},\vec{\sigma})) \\ &= \sum_{n\kappa}\frac{(2j+1)}{4\pi r^2}\Big[|G_{n\kappa}(r)|^2+|F_{n\kappa}(r)|^2\Big], \end{aligned} \tag{2.95}$$

and the sum over $n\kappa$ extends over all occupied states.

Fig. 2.17 shows the ratio of the "full" Glauber phase of Eq. (2.88) to the approximated expression $\mathcal{G}_\mathcal{T}$ of Eq. (2.89) for proton emission out of the Fermi level in ^{4}He, ^{12}C and ^{56}Fe. The real part of the Glauber phase gets an adequate description in the thickness approximation down to the 5% level. In the absorptive part, an overall overestimation of FSI gets introduced through the averaging procedure. The large deviations appearing in the absorptive part mainly arise due to the fact that one considers the ratio of very small quantities. In general, the largest deviations arise when θ approaches 180^o. As stated above, the impact of these kinematical situations on the integrated matrix elements can be exptected to be of marginal importance.

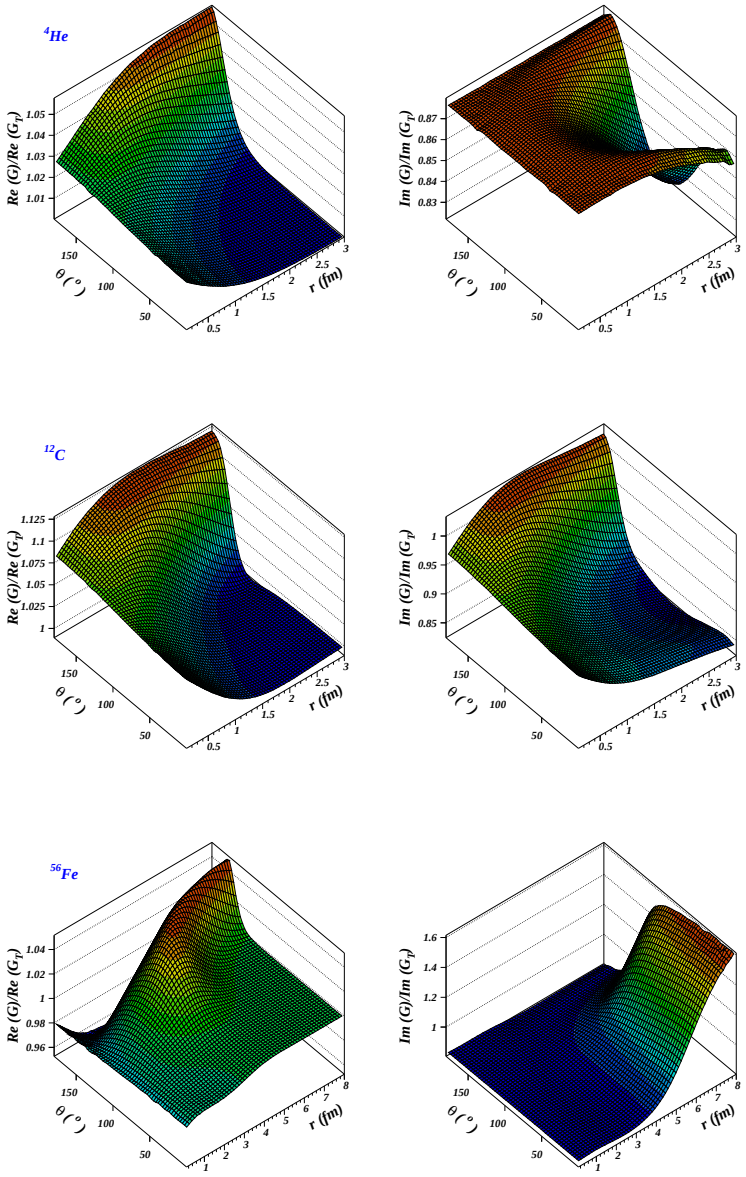

Figure 2.17 Effect of replacing the wave functions for the individual scattering centers by an average density for the computed Glauber phase $\mathcal{G}$. The results are obtained for $T_p = 1$ GeV for proton emission out of the Fermi level in ^{4}He, ^{12}C and ^{56}Fe. The figures display the ratio of the "full" Glauber phase of Eq. (2.88) to the approximated expression from Eq. (2.89).

Chapter 3

Transparencies in relativistic $A(e, e'p)$ models

The transparency of a medium to the propagation of one of its constituents is a topic of interest in many branches of physics. Hadron physics is no exception to this. The nuclear transparency provides a measure of the probability that a proton of a certain energy escapes from the nucleus without any further interaction. The nuclear transparency is a useful quantity for studying nuclear medium effects, and in particular, it is very well suited for investigations of the so-called color transparency (CT) phenomenon, which predicts a significant enhancement of the transmission of protons through nuclei once QCD mechanisms start playing a role [91, 92].

Nuclear transparency measurements with the $A(e, e'p)$ reaction are available for a range of target nuclei. The first experiments were performed at Bates for $Q^2 \approx 0.3$ (GeV/c)^2 [93], and at SLAC for $1 \leq Q^2 \leq 7$ (GeV/c)^2 [94, 95]. Recently, measurements at the Thomas Jefferson National Accelerator Facility (TJNAF) provided precise data for the target nuclei ^{2}D, ^{12}C and ^{56}Fe and $Q^2 = 3.3$, 6.1 and 8.1 (GeV/c)^2 [96]. The same facility provided an alternate set of data for the target nuclei ^{12}C, ^{56}Fe and ^{197}Au and 0.64$\leq Q^2 \leq$3.25 (GeV/c)^2 [7, 97, 98].

The prediction of the nuclear transparency to protons poses a serious challenge for models dealing with the $A(e, e'p)$ reaction due to the wide range of proton energies which are probed in the present-day experiments. Numerous predictions for the nuclear transparencies within the context of non-relativistic Glauber theory have been reported in literature [25, 26, 99, 100, 101, 102, 103, 104, 105]. These re-

sults are typically obtained in a non-relativistic and factorized model for dealing with the $e + A \rightarrow e' + (A-1) + p$ reaction dynamics. In this context, non-relativistic refers to the fact that the calculations use bound-state wave functions or nuclear densities from solutions to a Schrödinger equation and non-relativistic expressions for the electromagnetic photon-nucleus interaction Lagrangian. In the context of modeling $A(e, e'p)$ processes, factorization refers to the approximation of decoupling the electron-proton from the nuclear dynamics part in the calculations.

Here, we focus on relativistic and unfactorized descriptions of nuclear transparencies extracted from quasi-elastic $A(e, e'p)$ processes. In the past, RDWIA $A(e, e'p)$ calculations for the nuclear transparency have been presented by Kelly [106], Meucci [107] and Greenberg [72]. Kelly adopts an effective current operator containing the Dirac potentials, two-component bound states and distorted waves obtained as solutions to relativized Schrödinger equations. Meucci used bound-state wave functions from a relativistic mean-field approach, while the effective Pauli reduction was adopted to construct the ejectile's wave function.

In this chapter, transparencies obtained within the RMSGA and ROMEA frameworks will be compared with those obtained in the RDWIA framework as it has been implemented by the Madrid-Sevilla group [15, 108, 109, 110]. Both RMSGA and ROMEA models rely on the eikonal approach to calculate the scattering wave function, whereas the RDWIA pursues exact solutions of the Dirac equation. The ROMEA and RDWIA are similar in the sense that both of them estimate the effect of the scatterings on the emerging nucleon with the aid of proton-nucleus optical potentials. In contrast, in the RMSGA formalism the effects of FSI are computed directly from the elementary proton-nucleon scattering data. The comparison is made in a consistent way. For the transparency results which will be presented below, this implies that the frameworks only differ in the way they treat the final-state interactions. All the remaining ingredients are kept identical.

To check the consistency of our calculations, we start our discussion with a comparison of differential $A(e, e'p)$ cross sections in the predictions of the Ghent and Madrid models. Next, we present the definition of the nuclear transparency. Then, we focus on the sensitivity of the RDWIA transparencies to the adopted choice for the optical potentials and compare to the ROMEA results to probe the validity of the eikonal approximation. Further, we scrutinize the energy dependence, ex-

pressed in terms of the four-momentum transfer Q^2, and target-mass dependence of the nuclear transparencies obtained in the RMSGA and RDWIA approaches and compare them to the world data. Finally, we outline the theoretical assumptions which underly CT, and present RMSGA calculations which account for this QCD-related phenomenon.

3.1 Differential cross sections

In order to make the comparisons between the RDWIA, ROMEA and RMSGA transparency predictions as meaningful as possible, all the ingredients in the $A(e, e'p)$ calculations not related to FSI, as those concerning the implementation of relativistic dynamics and nuclear recoil effects, are kept identical. In particular, both pictures use the relativistic bound-state wave functions from a Hartree calculation with the "W1" parametrization for the different field strengths [62] (see section 2.3). Further, all the results presented are obtained within the Coulomb gauge using the so-called $CC2$ current operator [48] of Eq. (2.39b). For the description of nuclear transparencies, the effect of Coulomb distortions has been recognized as negligible [106]. Therefore, no attempt has been made to correct for the Coulomb-distortion effect.

In Chapter 2 it was outlined that in the relativistic impulse approximation to $A(e, e'p)$ reactions, the central quantity to be computed is the current matrix element [11]

$$\langle J^\mu \rangle = \int d\vec{r}\, \overline{\phi}_F(\vec{r}) \hat{J}^\mu(\vec{r}) e^{i\vec{q}.\vec{r}} \phi_B(\vec{r}) \; . \tag{3.1}$$

We wish to stress that the RDWIA, as implemented by the Madrid-Sevilla group, and RMSGA (ROMEA) codes adopt very different numerical techniques to compute the scattering wave functions and the corresponding matrix elements of Eq. (3.1). The Madrid RDWIA code employs a partial-wave expansion to solve the Dirac equation for the ejectile. The cylindrical symmetry of the Glauber and eikonal phases of Eqs. (2.88,2.64) prohibits any meaningful use of this technique in the RMSGA and ROMEA calculations. Instead, the multi-dimensional integrals are computed numerically. In the limit of vanishing FSI mechanisms, the so-called relativistic plane-wave impulse approximation (RPWIA) limit, however, the three codes should predict identical results. In the Glauber approach this limit is reached

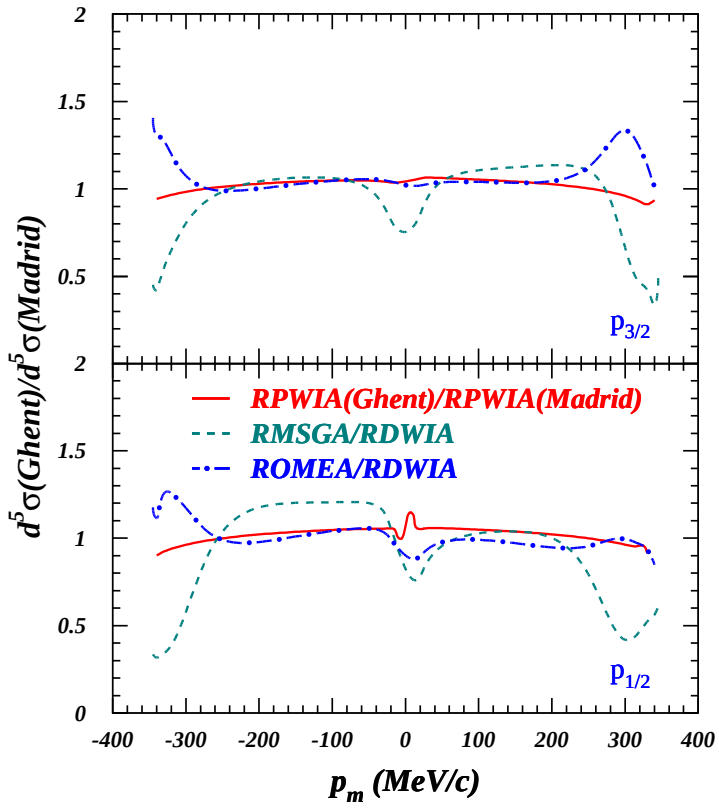

Figure 3.1 Comparison of RPWIA, RMSGA, ROMEA and RDWIA differential cross-section predictions for the ^{16}O$(e,e'p)$ reaction at ε=2.4 GeV, q=1 GeV and ω=0.442 GeV. The solid, dashed and dot-dashed lines show the RPWIA(Ghent)/RPWIA(Madrid), RMSGA/RDWIA, ROMEA/RDWIA ratios, respectively. Apart from the treatment of FSI, all ingredients are identical.

by putting the Glauber phase of Eq. (2.88) equal to unity. In the ROMEA and RDWIA pictures, the effect of FSI can be made vanishing by nullifying the optical potentials. Then, in the RDWIA, the computed partial waves sum to a relativistic plane-wave. To guarantee convergence, the total amount of partial waves grows with increasing proton kinetic energy. Convergence of the partial wave expansion was tested against the analytical plane-wave result [111] .

In Fig. 3.1, the ^{16}O$(e,e'p)$ cross sections calculated with the RPWIA, RDWIA, ROMEA and RMSGA models at ε=2.4 GeV, q=1 GeV and ω=0.442 GeV are dis-

played. To guide the eye, the ratios of the calculations, in particular RPWIA(Ghent) vs. RPWIA(Madrid), RMSGA vs. RDWIA and ROMEA vs. RDWIA, are shown. The optical models employ the EDAD1 parametrization for the potentials [70]. In the special case of vanishing FSI, the RPWIA(Ghent) and RPWIA(Madrid) codes produce differential cross sections with an agreement to better than 5% for the whole range of kinetic energies considered in this work. The remaining can be partially attributed to the numerical evaluation of the multi-dimensional integrals in RMSGA. This comparison gives us confidence about the consistency of the calculations and the validity of the numerics. For p_m below the Fermi momentum, the variation between the predictions of the ROMEA and RDWIA approaches is at most 10%, whereas the RMSGA cross sections are at most 25% larger compared to optical model calculations. Not surprisingly, at higher missing momenta (and corresponding larger polar angles), the differences between the exact and the eikonal approaches grow.

3.2 Nuclear Transparancy: definition

The nuclear transparency provides a measure of the likelihood that a struck nucleon with kinetic energy T_p escapes from the nucleus. The nuclear transparency is extracted from the measured $A(e, e'p)$ differential cross sections $d^5\sigma^{exp}(e, e'p)$ on the basis of the following ratio

$$T_{exp}(Q^2) = \frac{\int_{\Delta^3 p_m} d\vec{p}_m \int_{\Delta E_m} dE_m \; S_{exp}(\vec{p}_m, E_m, \vec{k}_f)}{c_A \int_{\Delta^3 p_m} d\vec{p}_m \int_{\Delta E_m} dE_m \; S_{PWIA}(\vec{p}_m, E_m)} \; . \tag{3.2}$$

Here, S_{exp} is the experimentally determined reduced cross section

$$S_{exp}(\vec{p}_m, E_m, \vec{k}_f) = \frac{\frac{d^5\sigma^{exp}}{d\Omega_p d\epsilon' d\Omega_{\epsilon'}}(e, e'p)}{K\sigma_{ep}}, \tag{3.3}$$

where K is a kinematical factor and σ_{ep} is the off-shell electron-proton cross section, which is usually evaluated with the $CC1$ prescription of de Forest [48]. The quantities $\Delta^3 p_m$ and ΔE_m specify the phase-space volume in the missing momentum and energy and are commonly defined by the cuts $|p_m| \leq 300\,\mathrm{MeV/c}$ and $E_m \leq 80\,\mathrm{MeV}$. These kinematic cuts, in combination with the requirement that the Bjorken variable $x = \frac{Q^2}{2M_p\omega} \approx 1$, guarantee that the electro-induced proton-emission process is

predominantly quasi-elastic. For example, the effects of two-body meson-exchange and isobar currents, which are neglected within the IA, have been shown to be at the percent level for quasi-elastic kinematics [112, 113].

In the above equation, S_{PWIA} is the reduced cross section within the plane-wave impulse approximation (PWIA) in the non-relativistic limit. The factor c_A in the denominator of Eq. (3.2) has been introduced to correct in a phenomenological way for short-range mechanisms and is assumed to be moderately target-mass dependent. It accounts for the fact that short-range correlations move a fraction of the single-particle strength to higher missing energies and momenta and, hence, beyond the ranges covered in the integrations $\int d\vec{p}_m \int dE_m$ of Eq. (3.2). The values for c_A which are adopted to extract the transparency from the $A(e,e'p)$ measurements are 0.9 (^{12}C), 0.88 (^{28}Si), 0.82 (^{56}Fe) and 0.77 (^{208}Pb).

Theoretically, the nuclear transparencies are extracted from the computed relativistic $A(e,e'p)$ angular cross sections for the individual single-particle states, according to

$$T_{theo}(Q^2) = \frac{\sum_\alpha \int_{\Delta^3 p_m} d\vec{p}_m S^\alpha(\vec{p}_m, E_m, \vec{k}_f)}{c_A \sum_\alpha \int_{\Delta^3 p_m} d\vec{p}_m S^\alpha_{PWIA}(\vec{p}_m, E_m)} \,. \tag{3.4}$$

This expression reflects the one used to determine T_{exp}. Indeed, in our approach, we obtain the "theoretical" transparencies by adopting identical expressions and cuts as in the experiments. Essentially, we replace the measured $A(e,e'p)$ angular cross sections by the computed ones. As our relativistic models to compute the transparencies adopt the IA and a mean-field approach, it may be argued that the factor c_A in the denominator of Eq. (3.4) can be let out. This would, however, necessarily introduce an additional model dependence in our calculations. Indeed, one would need to assume that the effect of correlations is Q^2 independent and that it can be quantified by the aforementioned values of c_A. As neither of these two assumptions can be considered realistic, we prefer to stick with a theoretical definition of the transparency that matches as closely as possible the one adopted in the analysis of the data. We wish to stress that the factors c_A have no impact on the comparisons between the relativistic approaches RDWIA, ROMEA and RMSGA. In addition, the integration over the missing energy $\int_{\Delta E_m} dE_m$ is replaced by a sum over all occupied shells ($\sum_\alpha$) in the ground state of the target nucleus. Indeed, the relativistic Hartree approximation predicts bound-state eigenfunctions with a fixed

energy-eigenvalue and zero width (like any mean-field approach). When determining the denominator in Eq. (3.4), in our calculations the PWIA limit is accomplished by nullifying all sources of FSI mechanisms and neglecting those contributions introduced by the presence of negative-energy components in the relativistic bound nucleon wave function [111].

3.3 Results

Transparencies have been calculated for the nuclei ^{12}C, ^{28}Si, ^{56}Fe and ^{208}Pb. All numerical calculations are performed in planar and constant $(\vec{q}, \omega)$ kinematics. The adopted values for $|\vec{q}|$ and ω are the central values of the kinematics in the $A(e, e'p)$ transparency experiments reported in Refs. [7, 93, 94, 97]. For each shell α, the kinetic energy of the outgoing nucleon is calculated by means of the relationship $T_p = \omega + E_\alpha$, where E_α is the energy eigenvalue of the corresponding single-particle state. Due to the internal motion of the confined protons, the ejected protons emerge in a cone about the transferred momentum. The boundaries of the cone are restricted by the requirement that the "initial " proton momentum $|p_m| \leq 300$ MeV/c.

In the RDWIA and ROMEA calculations, we have employed the global $S - V$ parametrizations of Cooper *et al.* [70], which provide the best phenomenological optical potentials to date. As the highest kinetic energy in these parametrizations is 1 GeV, RDWIA/ROMEA transparencies are obtained up to four-momentum transfers of $Q^2 \approx 1.8$ (GeV/c)^2. Due to the use of the eikonal approximation, the validity of ROMEA and RMSGA becomes questionable when approaching low values of Q^2. The ROMEA transparencies will be presented down to the lowest Q^2-values ($T_p \approx 0.3$ GeV), in order to probe the validity limits of the eikonal approach. The RMSGA model is not used for calculating transparencies below $Q^2 \approx 0.6$ (GeV/c)^2. Hence, the kinematic range $0.6 \leq Q^2 \leq 1.8$ (GeV/c)^2 will be covered in the RMSGA, the RDWIA and ROMEA frameworks.

3.3.1 Optical-potential models

First, we investigate the sensitivity of the computed transparencies to the adopted parametrizations for the optical potentials. In Fig. 3.2 results for ^{12}C and ^{208}Pb

are displayed as a function of Q^2 for different optical-potential parametrizations contained in Ref. [70]. Consider the calculations in the RDWIA framework. For ^{12}C, both the predicted Q^2 dependence and the value of the transparency depend on whether A-dependent (EDAD1/EDAD2) or A-independent (EDAIC) fits for the potentials are selected. A-dependent fits are more global in the sense that with one parameter set one can cover a range in proton kinetic energies and a range in target nuclei. For ^{208}Pb, the noted differences between the different types of optical-potential sets are less pronounced. Within the class of A-dependent parametrizations, the versions EDAD1 and EDAD2 give rise to comparable nuclear transparencies.

In the remainder of this chapter, the EDAD1 version will be used. There are various arguments to motivate this choice. First, the A-independent parametrization is only available for a very limited number of nuclei, and extrapolation to other nuclei has been discouraged [70]. Second, all energy-dependent A-dependent parametrizations in Ref. [70] produce similar transparency predictions. Finally, the relativistic transparency calculations by Kelly [106] and Meucci [107] employed the EDAD1 parametrization. Adopting the same choice facilitates the comparison between these predictions and ours.

In order to test the limits of the eikonal approximation, the ROMEA transparencies for the EDAD1 version are also displayed in Fig. 3.2. The RDWIA and ROMEA coincide within 8% over the entire Q^2 range, even at the lowest values where the eikonal approach becomes questionable. This gives us confidence that integrated quantities, such as the nuclear transparency, are probably less sensitive to the details of FSI such that the eikonal approach may be sufficiently accurate at lower ejectile energies. Similar conclusions were found for the other optical-potential parametrizations. Since the eikonal approximation turns out to be adequate for the description of nuclear transparencies, further on we will mainly focus on the differences between "nucleon-nucleon"(or, Glauber) and "nucleon-nucleus"(or, optical potential) models. To that purpose, the RDWIA calculations are considered as representatives for these latter ones.

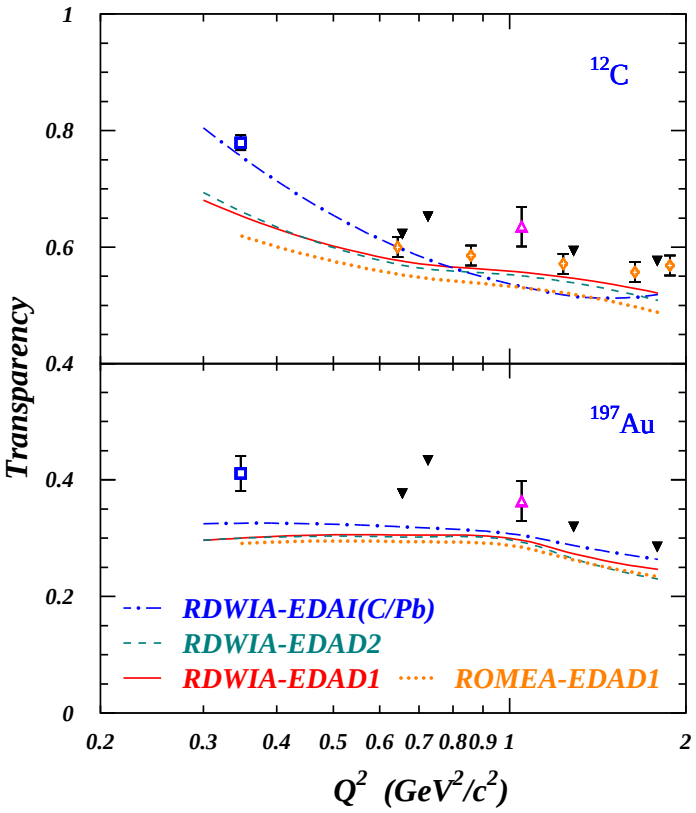

Figure 3.2 The sensitivity of the computed nuclear transparencies in ^{12}C and ^{197}Au to the adopted choice for the parametrization of the relativistic optical potentials. Results of RDWIA calculations with the EDAD1 (solid curve), EDAD2 (dashed curve) and EDAIC/EDAIPb (dot-dashed curve) are shown. The dotted line displays the ROMEA calculations with the EDAD1 version. Data points are from Refs. [93] (open squares), [94, 95] (open triangles), [7, 97](solid triangles) and [98](open diamonds).

3.3.2 "Nucleon-Nucleon" vs. "Nucleon-Nucleus"

In Fig. 3.3, the transparencies predicted by the RMSGA and RDWIA models are displayed as a function of Q^2 and compared to the world data. The ^{197}Au data are compared to ^{208}Pb calculations. The RDWIA approach systematically underestimates the data by roughly $5-10\%$. The presented RDWIA transparency results for ^{56}Fe and ^{208}Pb are in better agreement with the data than those reported in [97]. The RDWIA transparencies obtained in Ref. [107], on the other hand, are rather

comparable to ours for low Q^2, the differences increasing for higher values.

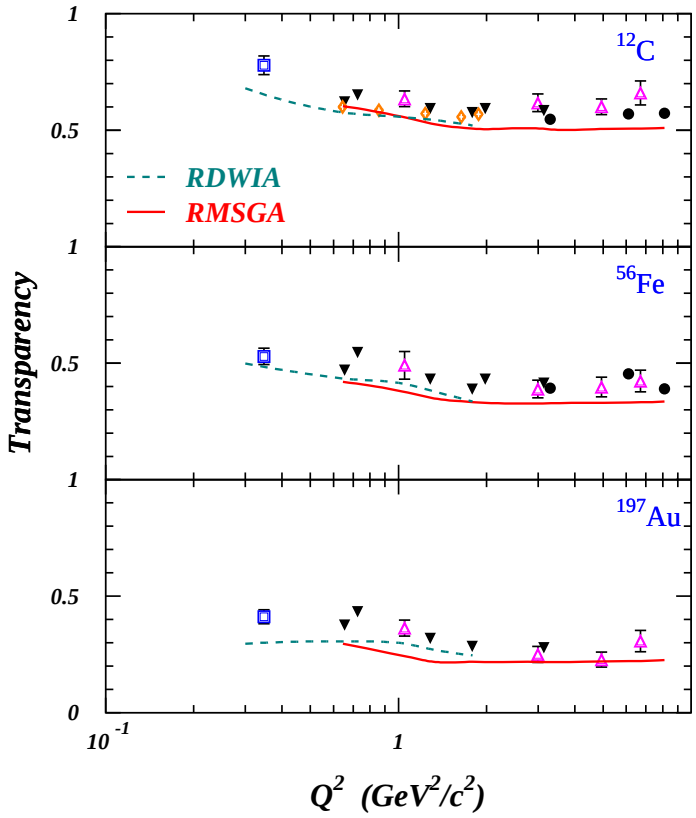

Figure 3.3 Nuclear transparencies versus Q^2 for $A(e,e'p)$ reactions in quasi-elastic kinematics. The RMSGA (solid lines) are compared to the RDWIA (dashed lines) results. Data are from Refs. [93] (open squares), [94, 95] (open triangles), [96](solid circles), [7, 97](solid triangles) and [98](open diamonds).

A global feature of the RDWIA and RMSGA calculations presented here, is that they tend to underestimate the measured transparencies. Further, the RMSGA predictions for the nuclear transparencies are in reasonable agreement with those of the typical non-relativistic Glauber approaches, as for example reported in Ref. [104]. In section 2.5.2 it was pointed out that genuine relativistic effects play a minor role in the predicted FSI effects as computed in the RMSGA model. The relativistic effects in the electromagnetic couplings tend to become visible in some well identified structure functions, like the transverse-longitudinal interference, and at

high missing proton momenta. Neither of these is highly important for a phase-space averaged quantity like the nuclear transparency. This makes the nuclear transparency to exhibit modest sensitivity to the details of the relativistic dynamics, once the relativistic kinematics is properly taken into account. We insist, however, on the necessity of including relativistic ingredients in transparency calculations, in particular when the kinetic energies of the ejected protons are of the order of the nucleon mass.

As can be inferred from Fig. 3.3, the RMSGA framework predicts less absorption than RDWIA for a light nucleus like ^{12}C. With increasing target mass the opposite holds true and when approaching the heaviest target nuclei considered here, the Glauber framework predicts 5 to 10 percent more absorption. The measured Q^2 dependence is reasonably well reproduced by both relativistic calculations. For low Q^2 the models reproduce the trend of decreasing transparencies. For $Q^2 \geq 2$ (GeV/c)^2, the RMSGA transparencies are close to constant, in line with the measured ones and those predicted in typical non-relativistic Glauber models. In fact, the modest energy variation of the transparency in the RMSGA model is a reflection of the fact that the total and elastic proton-nucleon cross sections remain fairly constant once $T_p \geq 1.7$ GeV.

In Ref. [106] large discrepancies were observed between the DWIA $A(e, e'p)$ transparencies and the ones from Glauber calculations of Nikolaev [26, 100]. In contradistinction, Fig. 3.3 indicates reasonably good agreement between our RDWIA and RMSGA model predictions for light and medium-heavy nuclei like ^{12}C and ^{56}Fe. Modest variations emerge when moving to a heavy nucleus. In Ref. [106] the noted differences between the transparencies obtained from DWIA and those from the particular Glauber approach of Refs. [26, 100], are attributed to the fact that the latter adopts a closure property in deriving the expression for the attenuation factor. We wish to stress that this approximation is NOT used in the RMSGA formulation of Glauber theory. In computing the effect of FSI mechanisms on the $A(e, e'p)$ cross sections, the sum extending over the occupied states α in Eq. (3.4) is carried out in a similar fashion in RMSGA and RDWIA.

Investigating the attenuation for each individual shell in the target nucleus allows one to study the radial dependence of the FSI mechanisms. Indeed, the $1s_{1/2}$, for example, has spatial characteristics which are very different from the $1p_{3/2}$ or-

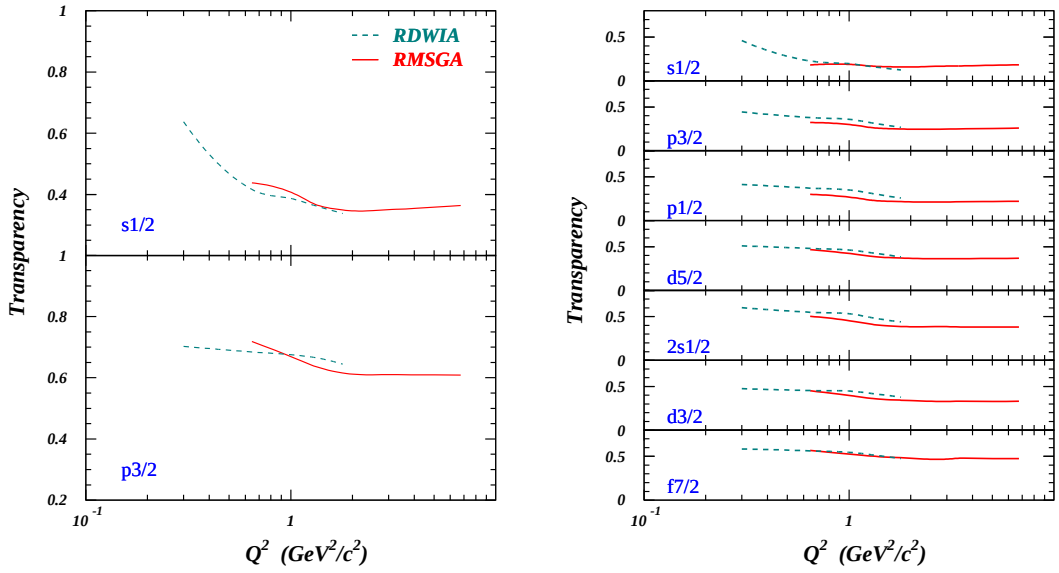

Figure 3.4 The Q^2 dependence of the computed nuclear transparency for the single-particle orbits as obtained in the RDWIA and RMSGA approach. Left (right) panel shows the results for ^{12}C (^{56}Fe).

bit. The attenuation for the individual states represents also a more stringent test of the (non-)similarity of the optical-potential and Glauber-based models for describing proton propagation through nuclei. In Fig. 3.4, the RMSGA and RDWIA predictions for the attenuation for the individual shells in ^{12}C and ^{56}Fe are compared. These numbers are computed according to the definition of Eq. (3.4) without performing the sum over the states α. Obviously, for ^{12}C the optical-potential approach predicts more absorption for both shells, whereas the predictions are in very good agreement for all single-particle shells in ^{56}Fe. As expected, both models predict a stronger attenuation for proton emission from a level which has a larger fraction of its density in the nuclear interior. Again, the results of Fig. 3.4 illustrate that the proton-nucleus (RDWIA) picture and the proton-nucleon picture (RMSGA) are not dramatically different in their predictions. These findings provide us additional confidence that the "low-energy" and "high-energy" regime can be bridged in a relatively smooth manner. Note further that the observed tendency

of increasing ^{12}C transparencies at low Q^2, can almost be entirely attributed to the $1s_{1/2}$ orbital.

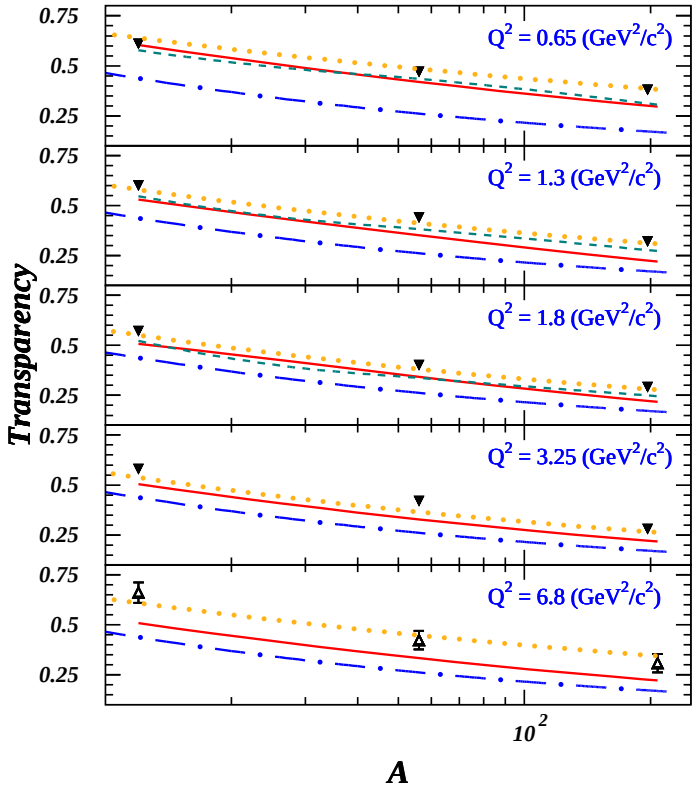

Figure 3.5 The A-dependence of the nuclear transparency at five values of the four-momentum transfer Q^2. The solid (dashed) curves are RMSGA (RDWIA) calculations. The dotted curves represent the $A^{-\alpha(Q^2)}$ parametrization, while the dot-dashed curve gives $A^{-1/3}$. Data are from [7, 97](solid triangles) and [94, 95](open triangles).

The A-dependence of the nuclear transparencies at various values of the four-momentum transfer is studied in Fig. 3.5. The RDWIA framework reproduces the measured A-dependence, while RMSGA slightly overestimates it. Under the assumption that the attenuation effect is proportional to the radius of the target nucleus one would naively expect that the A-dependence of the nuclear transparency

can be parametrized as

$$T(Q^2)=c(Q^2)A^{-\alpha(Q^2)} \ , \tag{3.5}$$

with α=1/3. In the work of Ref. [97] it was shown that the dependence of $T_{exp}(Q^2)$ on the mass number could be nicely fitted with $c(Q^2) \equiv 1$ and $\alpha \equiv 0.17 \pm 0.04 (Q^2$=0.65), $0.22 \pm 0.05 (Q^2$=1.3), $0.24 \pm 0.04 (Q^2$=1.8), $0.25 \pm 0.04 (Q^2$=3.3), $0.20 \pm 0.02 (Q^2$=6.8). To guide the eyes these curves are also displayed in Fig. 3.5.

In conclusion, despite the very different assumptions underlying the description of FSI effects in an optical-potential and Glauber based approach to $A(e,e'p)$, their predictions for the nuclear transparency and, in general, the effect of attenuation for different single-particle levels, are comparable.

3.4 Color transparency

Now that we are provided with baseline proton transparency calculations, we can study the so-called phenomenon of color transparency [91, 92]. This latter is one of the popular methods used to map the transition from hadronic to partonic degrees of freedom. The need for such a mapping arises from the fact that at low energies or long distances, the nucleon-meson picture is very succesful in describing the overall features of the strong interaction, while at high energies or short distances perturbative QCD with its quark-gluon degrees of freedom allows a precise description of the interaction. So far, there is no clear understanding of how these two regimes are connected.

A detailed description of CT would fall beyond the scope of this work. Here, we will only briefly sketch the basic assumptions which underly the concept of CT, and show RMSGA calculations which account for this effect, employing the most widely used procedure.

The basic idea of CT is that, under the right conditions, a $q\overline{q}$ or $3q$ system, which would normally interact very strongly with nuclear matter, could form a colourless object that passes undisturbed through the nuclear medium in hard processes. A clear signature for the onset of CT would involve a dramatic rise in the nuclear transparency with increasing hardness of the reaction. The assumptions which underly the concept of CT are actually predictions by different non-perturbative QCD-

models that still need experimental verification. Following the work of Frankfurt *et al.* [114, 115, 116], the physics of CT in $A(e, e'p)$ is based on three requirements:

(i) small objects are produced at high Q^2 reactions

Fig. 2.7 revealed that the nucleon-nucleon interaction becomes predominantly inelastic at high energies. Consequently, in a hadronic picture, one expects that a nucleon, excited by a highly energetic virtual photon , scatters into inelastic channels. However, due to the tight connection between high momentum transfer and small wavelengths, the virtual photon can probe the subnucleonic degrees of freedom. Suppose now that the incoming photon hits one of the confined colored quarks. The struck quark becomes off-energy shell by $\delta E \sim \omega$. So it has a lifetime $\tau \sim 1/\omega$ and decays by emitting a gluon. The confinement principle leaves now two possibilities: the quark hadronizes or it recombines with its companion quarks, which absorbed the emitted gluons. The second option is only viable when the other quarks were at most at distance $r \sim 1/\omega$ away from the off-shell quark. This means that the struck proton must have been a compact or point-like configuration (PLC).

Lattice calculations indicate that in QCD the so-called elementary particles are bound states of strongly interacting quarks and gluons. The hadron can be described in terms of an infinite number of basis states, e.g. $|qqq\rangle$,$|qqq+\pi\rangle$,... Different configurations are expected to have varying sizes. In quantum mechanics, a system fluctuates between its different configurations. Thus, "snapshots" of a hadron at different times would reveal both small- and large-sized configurations. One refers to these changes as color fluctuations. The uncertainty principle yields a time scale for fluctuations between two configurations: $\tau \sim 1/(m - M)$. The relevant mass differences are typically of the order of hundreds of MeV, so the fluctuation time is of the order of 1 fm. The possibility of PLC's at experimental available momentum transfers has been investigated by Frankfurt *et al.* [115], where several models of a nucleon have been analyzed with realistic short-range quark-quark interactions. It was found that small-sized PLC's already can occur at Q^2 of the order of a few $(\mathrm{GeV/c})^2$.

(ii) small objects have reduced interactions

The second condition which has to be fulfilled for CT to exist, is that the small object interacts in an anomalously weak manner with the surrounding nuclear medium. This assumption arises naturally from a two-gluon exchange model between two color singlets. As gluons carry color, single gluon exchange is forbidden. The situation finds its analogue in the charge screening effect in QED, where two neutral atoms interact with one another through their electric dipole moment. A small object will have a small electric dipole moment, and will interact in a much weaker way than a normal sized object. In this respect, the force between two color singlets can be regarded as a "color Van der Waals force".

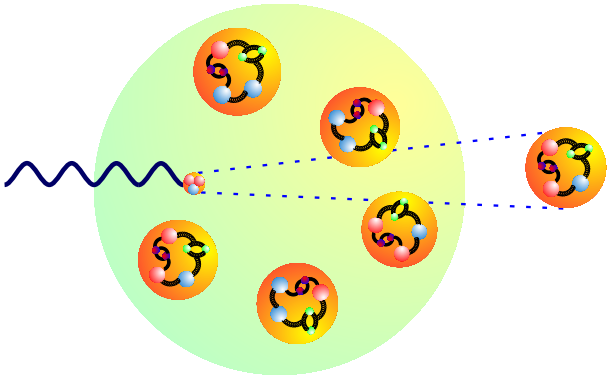

Figure 3.6 Schematic representation of the interaction of an expanding PLC with the surrounding nucleons.

(iii) small objects escape the nucleus before expanding

The PLC is not a stationary eigenstate of the QCD Hamiltonian, but a wave packet. Such a wave packet undergoes time evolution, which can only increase its size and restore soft quark-gluon fields. In its way out of the nucleus, the PLC expands and, if this expansion is fast enough, it will become normal-sized before leaving the nucleus. As such, it will interact as a "normal" nucleon with the surrounding medium. A schematic representation of this expansion is given in Fig. 3.6.

Consider a hadron with a large laboratory momentum k_f. Suppose that this hadron fluctuates from a PLC state with bare mass M to an object of normal hadronic

size with ground-state mass m. Then, the energy difference between the two configurations is given by $\sqrt{k_f^2+M^2}-\sqrt{k_f^2+m^2}\approx(M^2-m^2)/2k_f$. The time scale is inversely proportional to the energy. As such, a very large k_f implies a long fluctuation time scale. Before decaying, the PLC configuration of bare mass M can move now for a distance

$$l_c=\frac{2k_f}{M^2-m^2}\ , \tag{3.6}$$

the so-called coherence length. The condition for full CT to occur, can now be written as $l_c \gg R_A$. For sufficiently large energies, l_c is large enough so that the object can leave the nucleus while small enough to avoid FSI. Different estimates based on quark models lead to values of fluctuation time τ=$2k_f/(M^2-m^2)$ of $0.4-1.0$ (ϵ/GeV)fm. So with current values of ϵ up to 5 GeV, expansion will occur and FSI can not completely be disregarded. It should however be possible to get an estimate of the rate of this expansion in the few GeV regime.

The simplest way to include CT is to replace the free proton-nucleon cross section σ_{pN}^{tot} in the Glauber phase of Eq. (2.89) by a new quantity σ_{PLC}^{eff}, that describes the interaction of the PLC with the medium. This effective cross section needs to account for a suppression of interactions in the point where the PLC is produced and for a restoration of soft FSI with the nucleons as it moves through the nuclear medium. The need to include this expansion was recognized by Farrar *et al.*[117], who argued that the square of the transverse size is approximately proportional to the distance travelled from the point where the PLC is formed. We shall use the expression obtained in a quantum diffusion model [117]

$$\sigma_{PLC}^{eff}=\sigma_{pN}^{tot}\left\{\left[\frac{z}{l_c}+\frac{\langle n^2k_T^2\rangle}{Q^2}\left(1-\frac{z}{l_c}\right)\right]\theta(l_c-z)+\theta(z-l_c)\right\}. \tag{3.7}$$

Here, z is the distance passed by the expanding quark-gluon state along the trajectory from the point of hard interaction, n is the number of constituents in the proton (n=3), and k_T^2 is the average transverse momentum of constituents in the proton ($k_T^2\simeq(0.35GeV/c)^2$). The quantity l_c determines the length of the expansion, and depends on upon the squared mass difference of the initial PLC and the final hadron. Based on several constituent quark models, this difference is usually bound in the range of $0.7\leq\Delta M^2\leq 1.1$ (GeV/c)^2. An optimistic value of $\Delta M^2\approx 0.7$ (GeV/c)^2 would give an opportunity to witness the effect of CT for

energies as low as $Q^2 \geq 5$ (GeV/c)^2. In Ref. [116], it was outlined that some pitfalls may arise in the search for CT at intermediate energies. None of these have been taken into account here.

Fig. 3.7 displays the RMSGA calculations for the nuclear transparency in $A(e, e'p)$ reactions in ^{12}C and ^{56}Fe. We remark that all curves displayed here are obtained with the thickness approximation for the Dirac-Glauber phase, in order to save computer time. This is justified since our main aim is to estimate the relative effect of CT. The solid line shows the standard RMSGA calculations without the inclusion of CT effects. The dashed and dot-dashed lines account for the effect of CT with the quantum diffusion model parametrization of Eq. (3.7). Our results are in very close agreement to those of Refs. [118],[116],[100].

The experiments carried out so far have shown that there is no conclusive evidence for the onset of CT in qqq systems such as protons, up to Q^2 of 8.1 (GeV/c)^2. However, a number of experiments on the $q\overline{q}$ systems seem to show hints of CT-like effects and a recent experiment [7] from Jlab has shown interesting deviations from traditional calculations, which support claims for an early onset of CT in $q\overline{q}$ systems. The planned upgrade of Jlab to 12 GeV will potentially resolve the issue of the onset of phenomena such as CT by extending the search to very high Q^2.

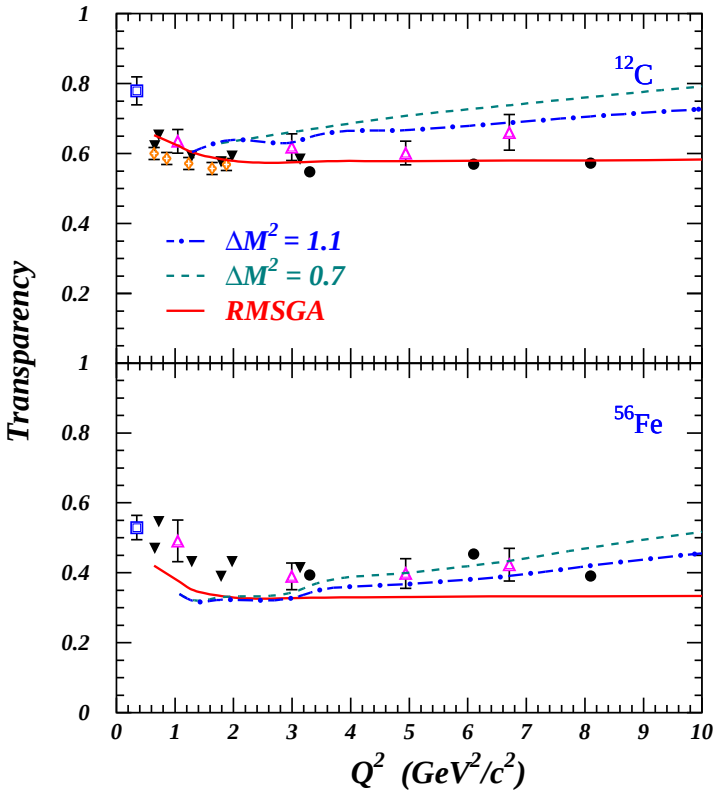

Figure 3.7 The nuclear transparency versus Q^2 for $A(e, e'p)$ reactions in quasi-elastic kinematics. The solid line shows the standard RMSGA results. The dashed (dot-dashed) account for the effect of CT in a quantum diffusion model with ΔM^2=0.7(1.1) (GeV/c)^2. Data are from Refs. [93] (open squares), [94, 95] (open triangles), [96](solid circles), [7, 97](solid triangles) and [98](open diamonds).

Chapter 4

Observables in $A(\vec{e}, e'\vec{p})$ reactions

The first chapter focussed on various methods to treat final-state interactions in exclusive $A(e, e'p)$ reactions. Next, results on $A(e, e'p)$ transparencies revealed that the low- and high-energy regimes can be bridged in a smooth manner. Nuclear transparencies, however, are integrated (or, inclusive) quantities and may hide some of the subtleties of the different models. Here, we will put the several frameworks to treat FSI mechanisms to more stringent tests by comparing them with exclusive $A(\vec{e}, e'\vec{p})$ data that have been collected at various electron scattering facilities.

The outline of this chapter is as follows. In sec. 4.1, we shed light on the transferred polarization components P'_l and P'_t. Recently, these observables have attracted considerable interest since they may provide us access to answering the delicate question whether or not the nucleon form factors are modified in the medium. In Sec. 4.2 the induced normal polarization P_n is the subject of investigation. In the one-photon exchange approximation, P_n vanishes in the absence of FSI. As such, this observable serves as a rigid test for models dealing with FSI mechanisms. Another quantity that reflects the sensitivity to the different ingredients that enter into our model calculations is the left-right asymmetry A_{LT}. Results on this will be presented in Sec. 4.3.

4.1 Polarization transfer in ^{4}He$(\vec{e}, e'\vec{p})$ and ^{16}O$(\vec{e}, e'\vec{p})$

In conventional nuclear physics, nuclei are described in terms of point-like protons and neutrons, interacting through the exchange of mesons. It has been a long-standing and unresolved issue whether the electromagnetic properties of bound nucleons differ from those of free nucleons. Any sizable modification would have a severe impact on the interpretation of e.g. the EMC effect [119].

Inclusive $A(e, e')$ data, including their separated longitudinal and transverse cross sections, are rather inconclusive with respect to the allowed ranges for medium modifications. Indeed, a recent re-analysis of the longitudinal inclusive ^{4}He(e, e') response, implementing two-body effects in the nuclear charge operator and realistic wave functions, finds the data consistent with the state-of-the-art calculations when using free-nucleon electromagnetic form factors [120]. On the contrary, an alternate recent re-evaluation of the Coulomb sum rule (CSR) concentrating on heavier nuclei, discerns it considerably quenched for $A \geq 40$, thereby not excluding sizable medium modifications for the electric form factor $G_E(Q^2)$ [121]. A y-scaling analysis of the inclusive $A(e, e')$ data [122], on the other hand, indicates that the medium effects on the magnetic form factor $G_M(Q^2)$ are smaller than 3% for $Q^2 \geq 1$ (GeV/c)^2. At lower values of the four-momentum transfer Q^2, a considerably improved description of the separated longitudinal and transverse $A(e, e')$ responses for ^{12}C and ^{40}Ca was reached after including in-medium $G_E(Q^2)$ and $G_M(Q^2)$ form factors as computed in the Nambu-Jona-Lasinio model [123]. This model provides a reasonable description of the dynamical breaking of chiral symmetry at nuclear-physics' scales.

Exclusive $A(e, e'p)$ processes have been put forward as more discriminative than inclusive $A(e, e')$ when it comes to investigating specific aspects of nuclei, and in particular, the possible modifications of the electromagnetic properties attributed to the presence of a medium. Finding signatures of those medium modifications, however, requires an excellent control over all those ingredients of the $A(e, e'p)$ reaction process that are directly related to the presence of a nuclear medium. They include medium-related effects, such as FSI, meson-exchange currents (MEC) and isobar currents (IC). We wish to stress that in principle there is a clear distinction between FSI, MEC and IC effects and those dubbed "medium modifications". Indeed, the latter refer to medium-driven changes in the internal quark-gluon structure of

nucleons. Unfortunately, at the level of the $A(e, e'p)$ observables, no formal distinction can be made between FSI, MEC and IC effects on one hand and possible medium modifications.

In the eighties, it was suggested that the ratio of the transverse (T) to the longitudinal (L) response in exclusive $A(e, e'p)$ may provide a handle on the medium modifications of the nucleon's electromagnetic properties [124, 125]. The longitudinal-transverse $A(e, e'p)$ separations suggested substantial deviations from the naive PWIA predictions for the T/L ratio. The data for medium-heavy nuclei like ^{12}C and ^{40}Ca, however, could be satisfactorily explained after implementing FSI mechanisms [126], thereby adopting free-nucleon electromagnetic form factors. For the ^{4}He nucleus, charge-exchange processes turned out to be of great importance to explain the measured T/L ratios [127, 128, 129]. The above-mentioned findings indicate that medium modifications of the electromagnetic form factors are apparently modest and support the picture that despite their substructure, nucleons are rather robust objects.

In polarized electron free-proton scattering $\vec{e}(E_e) + p \longrightarrow e'(E_{e'}) + \vec{p}$, the ratio of the electric to the magnetic Sachs form factors, can be extracted from [130]

$$\frac{G_E(Q^2)}{G_M(Q^2)} = -\frac{P'_x}{P'_z}\,\frac{E_e + E_{e'}}{2M_p}\tan\left(\frac{\theta_e}{2}\right) . \tag{4.1}$$

Here, P'_x and P'_z is the transferred polarization in the direction perpendicular to and parallel with the three-momentum transfer, defined as in Eq. (2.37). For bound nucleons, deviations from the measured ratio of P'_x/P'_z from the above value (thereby adopting free-nucleon form factors) can indicate the existence of medium modifications. Indeed, of all observables accessible in $A(e, e'p)$, the transferred polarization components P'_i have been recognized as the ones with the weakest sensitivity to FSI, MEC and IC distortions [89, 109, 111, 131, 132, 133]. Therefore, polarization-transfer components have been put forward as a tool to examine the magnitude of the in-medium electromagnetic form factors.

Recently, $(\vec{e}, e'\vec{p})$ measurements for the target nuclei ^{16}O [45] and ^{4}He [8, 9] have been reported. The ^{16}O$(\vec{e}, e'\vec{p})$ measurements have been confronted to various non-relativistic and relativistic calculations [134, 135, 136, 137, 138]. All these calculations utilize an optical potential to incorporate the FSI. The calculations of Ref. [137] indicate that two-nucleon currents like MEC and IC affect the polarization-transfer

components in ^{16}O to less than 5% provided that missing momenta below 200 MeV/c are probed. The non-relativistic calculations of Ref. [134] attributed somewhat larger corrections to the two-nucleon currents, in particular for proton knockout from the $p3/2$ and $s1/2$ shells. All calculations, however, predict similar trends for the MEC and IC corrections on the polarization-transfer components. One major finding is that their effect dwindles with increasing Q^2 and decreasing missing momentum. Relativistic effects on the transferred polarizations P'_x and P'_z have been investigated in Refs. [135, 138] and are discerned at the few percent level as long as the probed missing momentum remains relatively small ($p_m \leq 200$ MeV/c). These studies also indicated that at higher missing momenta the uncertainties stemming from off-shell ambiguities are larger than the overall impact of the relativistic effects. Apparently, all theoretical investigations indicate that when probing low missing momenta in quasi-elastic kinematics, the effect on the polarization-transfer components of typical medium-related complications like MEC, IC and off-shell ambiguities can be kept under reasonable control.

In Ref. [9] the Jefferson Laboratory (JLAB) ^{4}He$(\vec{e}, e'\vec{p})$ data, which cover the range $0.5 \leq Q^2 \leq 2.6$ (GeV/c)^2, are compared to the state-of-the-art RDWIA calculations of Udías *et al.* [15]. This model provided a better overall description of the data when implementing medium-modified electromagnetic form factors as predicted in the Quark-Meson Coupling (QMC) model [139, 140, 141]. However, as stated already in the previous sections, this model loses its applicability in the highest kinematic energy regimes accessible at JLAB. For example, for the Q^2=2.6 (GeV/c)^2 case, the ^{4}He$(\vec{e}, e'\vec{p})$ data of Ref. [9] are compared to RDWIA calculations with extrapolated optical potentials.

In this chapter, RMSGA predictions for the polarization-transfer components in ^{4}He and ^{16}O will be presented and compared to the world data. The numerical calculations are performed with both free and medium-modified electromagnetic form factors. For the latter we use the predictions of the QMC model [139, 140, 141], the chiral-quark soliton (CQS) model [142, 143] and of a modified Skyrme model [144, 145]. In the next section, we briefly shed light on the aforementioned nucleon models and outline how these form factors are implemented in the calculation of the polarization-transfer components.

4.1.1 In-medium electromagnetic form factors

From the 1980's on, various models that examine the influence of the nuclear medium upon the internal structure of a composite nucleon have been published [140, 143, 144, 146, 147, 148]. In this section, we focus on the predictions of some selected nucleon models, in particular the QMC model [139, 140, 141], the CQS model [142, 143] and a modified Skyrme model [144, 145].

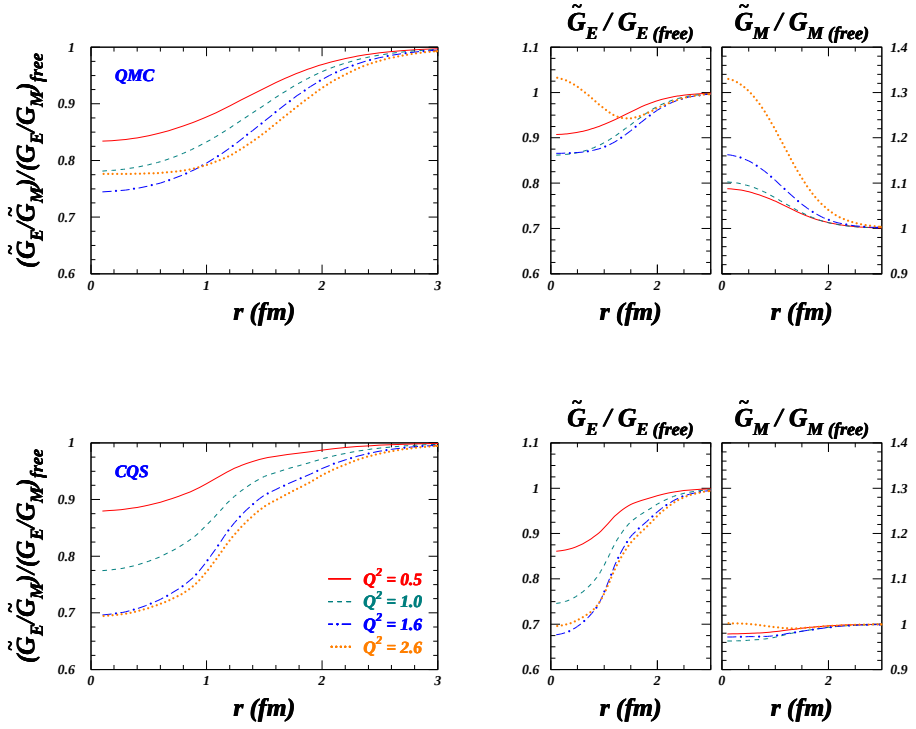

Figure 4.1 The radial dependence of G_E, G_M and G_E/G_M in ^{4}He at four different values of Q^2 (GeV/c)^2 in the predictions of the QMC model (upper panels) and of the CQS model (lower panels).

In the QMC model [139, 140, 141], the scalar (σ) and vector (ω) fields, carrying the forces between nucleons in Quantum Hadrodynamics [17, 58], couple directly to the quarks within the nucleon. As a result, the intrinsic properties of a bound nucleon are affected by the presence of a medium. In the QMC framework, the nucleon is described in terms of the MIT bag model with almost massless (m_q=5

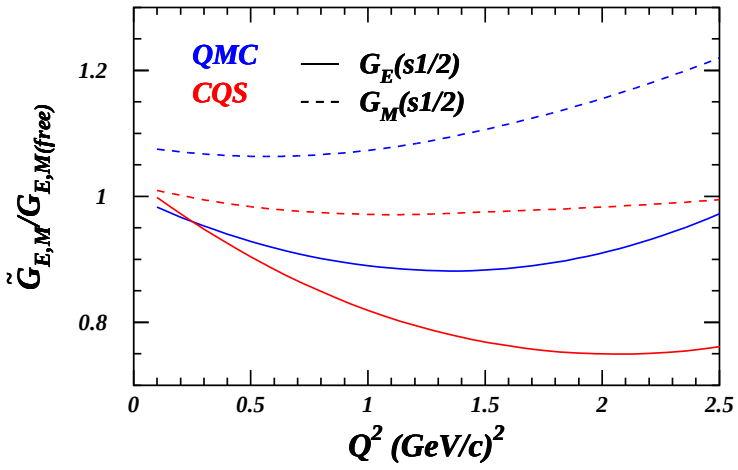

Figure 4.2 The Q^2 dependence of the ratio of the in-medium to the free electric and magnetic form factors for the proton in ^{4}He according to the QMC and CQS models.

MeV) and relativistic point-like quarks. Following the cloudy bag model (CBM), an elementary pion field coupled to the quarks inside the bag is introduced such that chiral symmetry is restored. A mean-field approximation for the description of the meson fields is adopted. This results in quark wave functions which look like the standard solution to the Dirac equation of Eq. (2.51). The nucleon wave functions are modified by the medium. More precisely, the mean values of the scalar $\langle\sigma\rangle$ and vector $\langle\omega\rangle$ fields are self-consistently determined by the coupled equations of motion for the $\sigma - \omega$ model [139].

For the $A(\vec{e}, e'\vec{p})$ results presented below, we use the QMC predictions corresponding to a bag radius of 0.8 fm. In the QMC model, the electric and magnetic form factors attain a dependence on the total baryon density of Eq. (2.95): $G_{E,M}(Q^2) \rightarrow G_{E,M}(Q^2, \rho_B(\vec{r}))$. The magnitude of the free form factors is not so well described within the QMC model. Therefore, we retain only the prediction for its density dependence and scale the free form factor with the ratio of the medium modified (MM) form factors at a given density, to the ones at vanishing baryon

density

$$\widetilde{G}^{MM}_{E,M}(Q^2, \rho_B(\vec{r})) = G_{E,M}(Q^2) \frac{G^{MM}_{E,M}(Q^2, \rho_B(\vec{r}))}{G^{MM}_{E,M}(Q^2, 0)}. \tag{4.2}$$

The CQS model [142, 143] bears a strong resemblance with the QMC one. In contrast to the QMC model, the CQS takes into account contributions from the sea. The sea quarks are almost completely unaffected by a dense environment, and serve to mitigate the effects on the valence quarks. The lack of medium effects in the sea can be seen directly in continuum dimuon production in high-energy hadron collisions, known as Drell-Yan experiments [149].

In Fig. 4.1, the QMC (upper panels) and CQS (lower panels) predictions for the radial dependence of $\widetilde{G}_E$, $\widetilde{G}_M$ and their ratio in ^{4}He are displayed at four different values of Q^2. Thereby, we have plotted the renormalized quantities as defined in Eq. (4.2). As can be inferred, the CQS model predicts somewhat larger effects than the QMC one for the electric form factor. Whereas the QMC model predicts a strong enhancement of G_M as the density increases, variations in this quantity are rather modest in the CQS model. In the CQS model, the orbital angular momentum carried by the sea is comparable to the one carried by the valence quarks. As such, the magnetic form factor receives equally important contributions from the valence and the sea. Conversely, the electric form factor is not affected by the sea to the same degree.

When hunting medium modifications in polarized $A(\vec{e}, e'\vec{p})$ experiments, however, one is rather interested in deviations in the double ratio G_E/G_M (see Eq. (4.1)). Figure 4.1 reveals that the CQS model follows the same trend as the QMC model.

In both models, the magnitude of medium modifications grows with Q^2. As suggested by Kelly in Ref. [133], the Q^2 dependence of the above ratios can be computed in the local density approximation (LDA) in terms of the following density convolution

$$\widetilde{G}^{MM}_{E,M}(\alpha_1, Q^2) = \frac{\int \widetilde{G}^{MM}_{E,M}(Q^2, \rho_B(\vec{r}))\ \rho_{\alpha_1}(\vec{r})\ d\vec{r}}{\int \rho_{\alpha_1}(\vec{r})\ d\vec{r}}\ . \tag{4.3}$$

Here, $\rho_{\alpha_1}(\vec{r})$ is the single-nucleon density corresponding with the state from which the proton is ejected. Figure 4.2 displays $\widetilde{G}^{MM}_{E,M}(s1/2, Q^2)$ for a proton in ^{4}He. Similar conclusions can be drawn as was done for the radial dependence. At $Q^2 \geq 1.5$

(GeV/c)^2, the averaged QMC medium magnetic form factor is 10% larger than the free one. This is considerably larger than what a y-scaling analysis of $A(e, e')$ appears to tolerate [122]. It has been pointed out that modifying the nucleon bag radius can considerably reduce the overall magnitude of the medium effects [150].

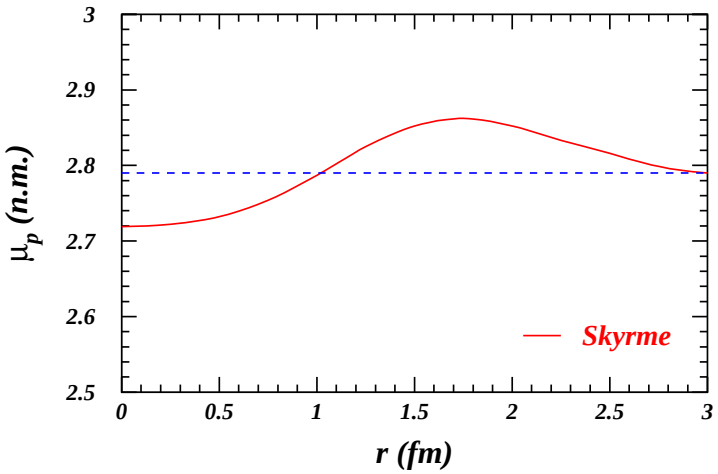

Figure 4.3 The radial dependence of the proton magnetic moment in ^{4}He according to the Skyrme model of Ref. [145]. The free case corresponds with μ_p=2.79 n.m.

Recently, Yakhshiev *et al.* [144, 145] addressed the issue of in-medium electromagnetic form factors in the framework of a modified Skyrme model. This model provides a fair description of nucleon properties in free space and adopts degrees of freedom inspired by the spontaneous chiral symmetry breaking of QCD. In contrast to most constituent quark models, the pion-cloud contribution is naturally taken into account. As a result, the influence of the nuclear medium and the nucleon's response to it, is predicted to be very probe dependent. Beyond $Q^2 = 0.6$ (GeV/c)^2, vector mesons and boost effects are deemed to come into play, and the Skyrme model is no longer considered realistic. In the Skyrme model, the proton magnetic moment gains an additional radial dependence dictated by the density of the nucleus. Whereas $G_E(Q^2)$ remains unaffected, its magnetic counterpart takes on the

form

$$G_M(Q^2, r) = \mu_p(r) G_E(Q^2). \tag{4.4}$$

In Fig. 4.3 the medium-dependent $\mu_p(r)$ from the Skyrme model is displayed as a function of the distance to the center of the ^{4}He nucleus. In the interior of ^{4}He, the magnetic form factor is mildly suppressed, whereas a modest increment is observed in the surface area. Weighting of $\mu_p(r)$ with the ^{4}He density leads to an effective magnetic moment which is quenched relative to the free value.

When including medium modifications in the $A(\vec{e}, e'\vec{p})$ calculations, the electromagnetic current operator of Eq. (2.39b) is modified according to

$$J^\mu(\vec{r}) = \widetilde{F}_1^p(Q^2, \rho_B(\vec{r}))\gamma^\mu + \widetilde{F}_2^p(Q^2, \rho_B(\vec{r}))i\frac{\kappa_p}{2m_p}\sigma^{\mu\nu}q_\nu \ . \tag{4.5}$$

The density-dependent Dirac and Pauli form factors are related to the $\widetilde{G}_E^{MM}(Q^2, \rho_B(\vec{r}))$ and $\widetilde{G}_M^{MM}(Q^2, \rho_B(\vec{r}))$ of Eq. (4.2) in the standard fashion. The medium-modified form factors $\widetilde{F}_{1,2}^p$ in Eq. (4.5) depend on the total density in the neighborhood of the nucleon that absorbs the virtual photon.

4.1.2 Results

All ^{4}He$(\vec{e}, e'\vec{p})$ and ^{16}O$(\vec{e}, e'\vec{p})$ calculations reported in this section are performed in quasi-elastic kinematics and adopt kinematical conditions which allow a direct comparison with the data from Refs. [8, 9, 45]. For the ^{4}He nucleus, the polarization-transfer measurements have been performed in parallel kinematics, whereas constant $(\vec{q}, \omega)$ kinematics are adopted for ^{16}O.

Throughout this section, we adopt a dipole parametrization for the free-nucleon form factors. In section 2.3 it was outlined that this choice may appear doubtful as improved fits implementing the new $p(\vec{e}, e')\vec{p}$ data are readily available [54]. For the present purposes, however, a dipole parametrization is adequate. Indeed, the ^{16}O$(\vec{e}, e'\vec{p})$ data are restricted to Q^2=0.8 (GeV/c)^2, where deviations between the dipole and more sophisticated parametrizations are minor. The ^{4}He polarization-transfer results, on the other hand, are commonly expressed in terms of a double ratio R

$$R = \frac{(P'_x/P'_z)_{^4He}}{(P'_x/P'_z)_{^1H}} \ , \tag{4.6}$$

which is almost independent of the used parametrization for the form factors, as long as identical ones are used for ^{4}He and ^{1}H. In order not to obscure the result by small kinematical differences between the individual ^{1}H and ^{4}He measurements, data and calculations are often shown in terms of a double ratio with the RPWIA result as baseline.

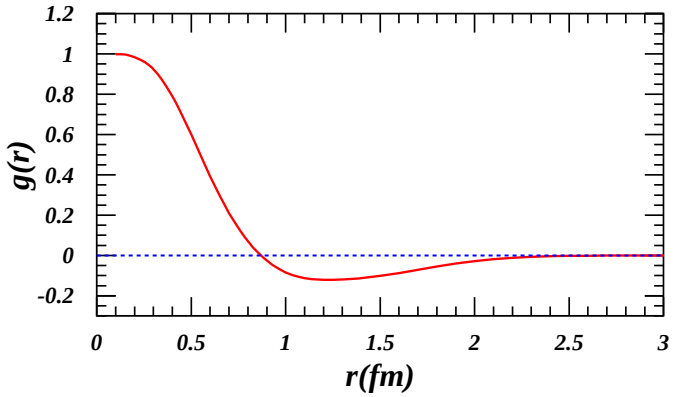

Figure 4.4 The Gearheart-Dickhoff correlation function of Ref. [151] as a function of the relative internucleonic distance r.

A source of theoretical uncertainty on the computed polarization-transfer components is the presence of short-range correlations (SRC). The RMSGA formalism outlined in chapter 2 is based on an independent-particle approximation. The effect of SRC on the FSI mechanisms can be estimated by introducing a central correlation function in the expression for the Dirac-Glauber phase of Eq. (2.88). This amounts to performing the following substitution

$$|\phi_\alpha(\vec{r}\,')|^2 \;\rightarrow\; |\phi_\alpha(\vec{r}\,')|^2 \;\left[1 - g(\vec{r} - \vec{r}\,')\right] \;, \tag{4.7}$$

where $g(\vec{r} - \vec{r}\,')$ is the central correlation function. In Eq. (4.7), $\vec{r}$ refers to the coordinate of the ejected nucleon, whereas the $\vec{r}\,'$ are the coordinates of the remaining nucleons from which it can scatter. Physically, the existence of a central correlation function reflects the inability of mean-field models to properly implement the

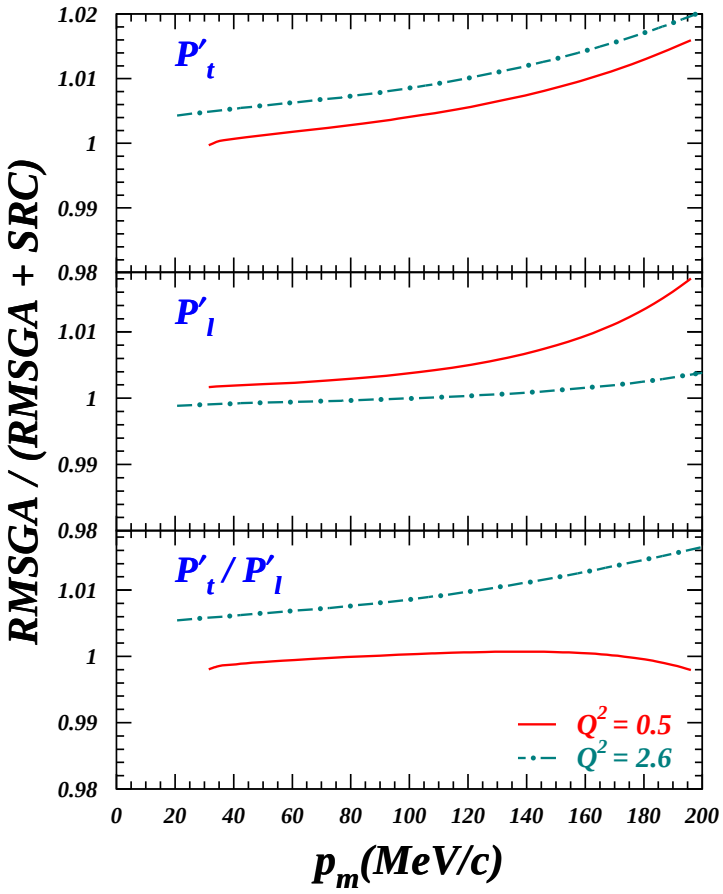

Figure 4.5 Relative effect of short-range correlations on the polarization-transfer components and their ratio. The solid (dot-dashed) curves refer to ^{4}He$(\vec{e}, e'\vec{p})$ in quasi-elastic and parallel kinematics for Q^2=0.5 (2.6) (GeV/c)^2. The RMSGA + SRC results implement the effect of SRC according to the prescription of Eq. (4.7).

strong repulsion of the nucleon-nucleon force at short internucleon distances. We use the central correlation function from a G-matrix calculation by Gearheart and Dickhoff [151] as plotted in Fig. 4.4. To date, the strongest sensitivity to central correlation functions is observed in exclusive $A(e, e'pp)$ reactions. The adopted correlation function provides a favorable agreement with the ^{12}C$(e, e'pp)$ and ^{16}O$(e, e'pp)$ data [152]. In the process of computing the Dirac-Glauber phase of Eq. (2.89), the introduction of a correlation function through the replacement of Eq. (4.7), strongly

reduces the interaction between the struck proton and any of the scattering centers when they are very close (internucleon distances smaller than 0.8 fm) and bring about a moderate enhancement for internucleon distances between 0.8 and 2 fm. In Fig. 4.5, we investigate the effect of SRC on the transferred-polarization components in ^{4}He at two different values of Q^2. The results are expressed in the barycentric frame defined in Eq. (2.28). As we can see, the SRC effects are relatively small, being typically of the order of 1% at a missing momentum of 200 MeV/c. Some asymmetric effect on P'_l and P'_t is seen. A major finding is that the effect of SRC on the Dirac-Glauber phase tends to cancel in the ratio R at smaller values of Q^2. At higher values, we predict a modest reduction of R due to SRC effects.

We now turn to the results for the double-polarization ratio R obtained for the ^{4}He nucleus. Response functions from the model calculations were used in a Monte-Carlo code [153] to calculate the proton polarization components averaged over the experimental acceptance. The starting point is always the huge number of events (experimental data or MC simulations) within the acceptance of the detectors. The full acceptance is then divided in various bins. For Figs. 4.6 and 4.7 there are four bins in p_m for the data and several more ($\approx 3 \times 10^3$) for the calculations. Next, the average value of the polarization is calculated for each bin. For the p_m distributions, the data is binned around a mean value of the missing momentum. The optimum comparison with the model would be to bin the MC data into the same number of bins as the data. One would then compare one data point with one calculated point. That way, however, the reader loses the information about the general missing momentum dependence. Our comparison is reliable as long as the transferred polarizations are not changing rapidly within the considered bin width.

Figure 4.6 shows R as a function of the missing momentum at Q^2=0.4 and 0.5 (GeV/c)^2. We note that positive missing momentum p_m corresponds to $|\vec{k}_f| < |\vec{q}|$. As can be inferred, the FSI have only a minor impact on R, but move the predictions somewhat closer to the measurements. Both RMSGA and RPWIA overestimate the double ratio R by nearly 10% and predict $R \approx 1$ for zero recoil momentum. After implementing the medium-modified electromagnetic form factors from the QMC model, the computed double-ratios R are lowered by almost 8%, resulting in a better overall agreement with the data. The predictions of the Skyrme and

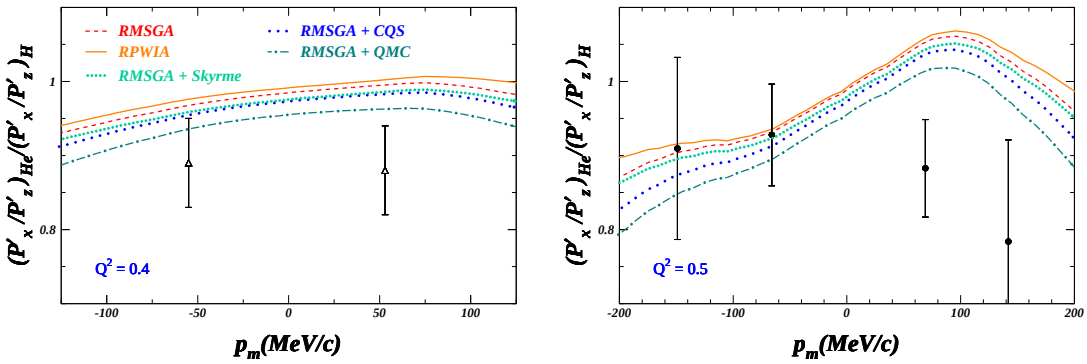

Figure 4.6 The double ratio R as a function of the missing momentum for Q^2=0.4 and 0.5 (GeV/c)^2 in ^{4}He. The solid (dashed) curve are RPWIA (RMSGA) calculations. The effect of medium modifications is shown for the QMC (dot-dashed), the CQS (long-dotted) and the Skyrme model (short-dotted). Data points are from [8](open triangles) and [9](solid circles).

CQS model are comparable and yield modest medium modifications which do not suffice to bring about a major improvement in the description of the data within the context of the RMSGA model.

Figure 4.7 summarizes the missing momentum dependence of the ^{4}He results for $Q^2 \geq 1$ (GeV/c)^2 [9]. The FSI effects on R are even smaller in this high-energy regime. For Q^2=1.6 (GeV/c)^2 the measured p_m dependence can be reasonably reproduced using free-nucleon form factors. Substituting the free form factors with the QMC and CQS ones reduces R, an effect which grows with p_m. Apparently, the differences between the QMC and CQS models dwindle with increasing energies, producing a nearly identical missing momentum dependence. At Q^2=1.0 (GeV/c)^2 the effect of medium modifications moves the theoretical curves closer to the data. Qualitatively our RMSGA results are not dramatically different from the RDWIA predictions presented in [9].

In Fig. 4.8, the superratio R/R_{RPWIA} is displayed as a function of Q^2. Also here, the data and calculations are integrated over the full experimental acceptance. The data and calculations are reported as single points at the nominal Q^2 value. The model "curves" only connect the computed points to guide the eye. As seen in

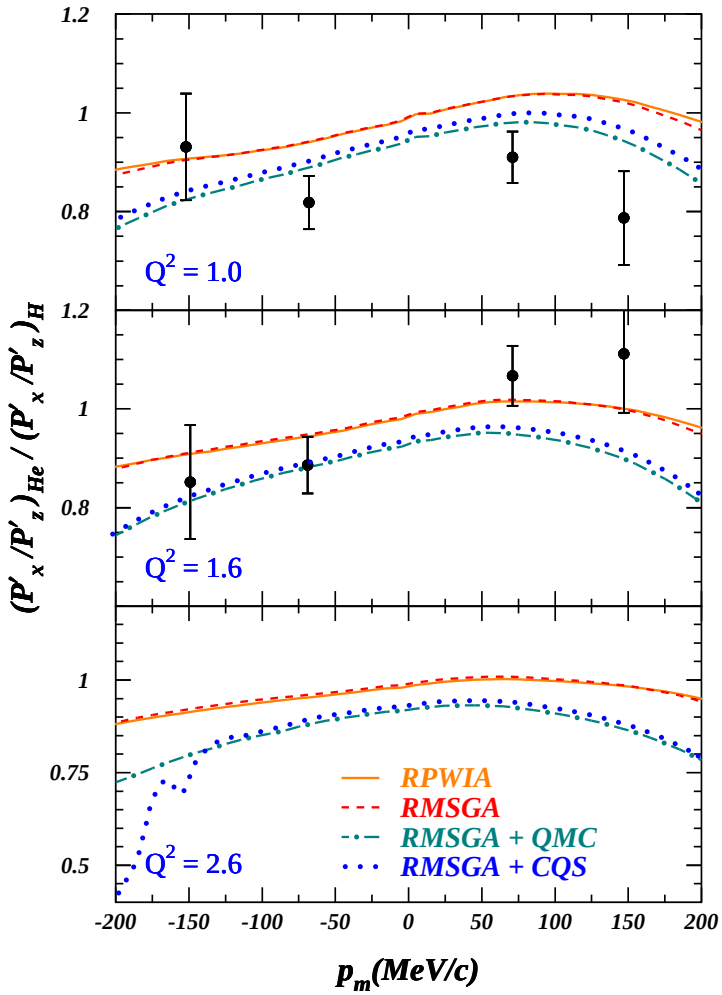

Figure 4.7 The double ratio R as a function of the missing momentum at three values of Q^2 in ^{4}He. The solid (dashed) curve are RPWIA (RMSGA) calculations, while the dot-dashed (dotted) curve represents RMSGA calculations including in-medium electromagnetic form factors of the QMC (CQS) model. Data points are from [9].

Fig. 4.8 the Mainz data point nicely matches with the lowest Q^2 measurement at JLAB. As off-shell effects are not completely negligible for the polarization-transfer components, it is worth stressing that the RDWIA (RMSGA) ^{4}He results shown here are obtained with the $CC1$ ($CC2$) current operator. For $Q^2 \leq 1$ (GeV/c)^2 the

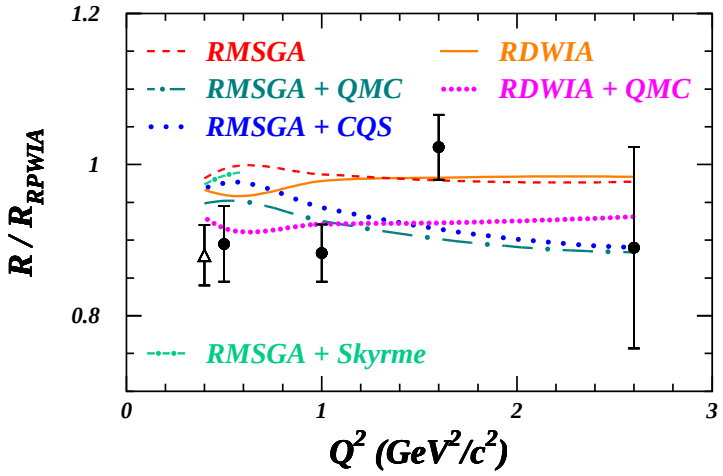

Figure 4.8 The superratio R/R_{RPWIA} as a function of Q^2 in ^{4}He. The dashed (solid) curve shows RMSGA (RDWIA) calculations, the long dot-dashed, long-dotted and short dot-dashed curves represent RMSGA calculations with in-medium electromagnetic form factors from the QMC, CQS and Skyrme model, respectively. The RDWIA and RDWIA+QMC (short-dotted) results are those from the Madrid group as reported in Ref. [9]. Data are from Refs. [8](open triangle) and [9](solid circles).

standard nuclear physics RDWIA and RMSGA results fail to reproduce the ratio R. The overestimation is of the order of 10% for RMSGA, and 5-7% in RDWIA. The predicted four-momentum dependence for R is modest in both models. The RMSGA attributes somewhat smaller effects to FSI than RDWIA does. In chapter 3, a similar trend was found when comparing RDWIA and RMSGA $A(e, e'p)$ nuclear transparencies for light nuclei.

Inclusion of medium modifications for the electromagnetic form factors according to the predictions of the Skyrme model shifts the RMSGA calculations marginally closer to the data. The results for the Skyrme model are shown up to Q^2=0.6 (GeV/c)^2 since the model is no longer deemed realistic at higher values. Implementing QMC electromagnetic form factors, on the other hand, lowers the p_m-integrated RMSGA predictions for the superratio R between 5% and 10%. The CQS model slightly worsens the agreement with the data at Q^2 $\leq$1 (GeV/c)^2, whilst at higher Q^2 it produces nearly identical results as the QMC model.

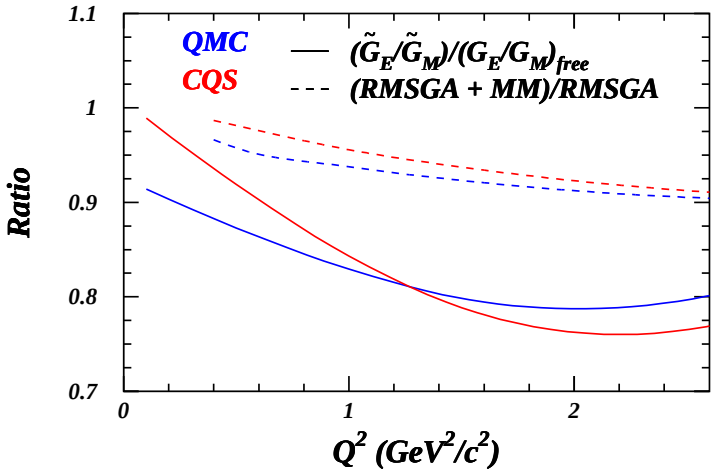

Figure 4.9 The ratio of the RMSGA+MM to the RMSGA prediction for R as a function of Q^2 for the $1s1/2$ proton in ^{4}He (dashed lines). Results are shown for the QMC and CQS models. The solid lines show $\left[\widetilde{G}_E^{MM}(1s1/2, Q^2)/\widetilde{G}_M^{MM}(1s1/2, Q^2)\right] / \left[G_E(Q^2)/G_M(Q^2)\right]$.

The difference between the RMSGA results with free and medium modified form factors for P'_x/P'_z grows with increasing Q^2. Referring to Fig. 4.9, this reflects the fact that in the QMC (CQS) model, the ratio $\widetilde{G}_E/\widetilde{G}_M$ moves steadily away from the free values with increasing Q^2 to reach a maximum of over 20% at $Q^2 \approx 2$ (GeV/c)^2, after which a change in the trend is observed. Fig. 4.9 also points out that about one third of the predicted magnitude of the medium modifications on G_E/G_M is visible in the P'_x/P'_z ratio. It is worth stressing that Fig. 4.9 compares two different quantities. On the one hand, the curve showing the $\widetilde{G}_E/\widetilde{G}_M$ has been averaged over the squared $1s1/2$ proton overlap wave function, thus receiving its largest contributions from the nuclear interior. This is not necessarily the case for the ^{4}He$(\vec{e}, e'\vec{p})$ observables. Indeed, in the process of computing the observables, the medium effects in the form factors are weighted with a more complex function which involves not only the $1s1/2$ proton overlap wave function, but also the current operator and the scattering wave function. The dashed curves of Fig. 4.9 indicate that on average larger radii, and correspondingly lower densities,

are probed. This phenomenon reduces the magnitude of the medium-dependent effects on the observables.

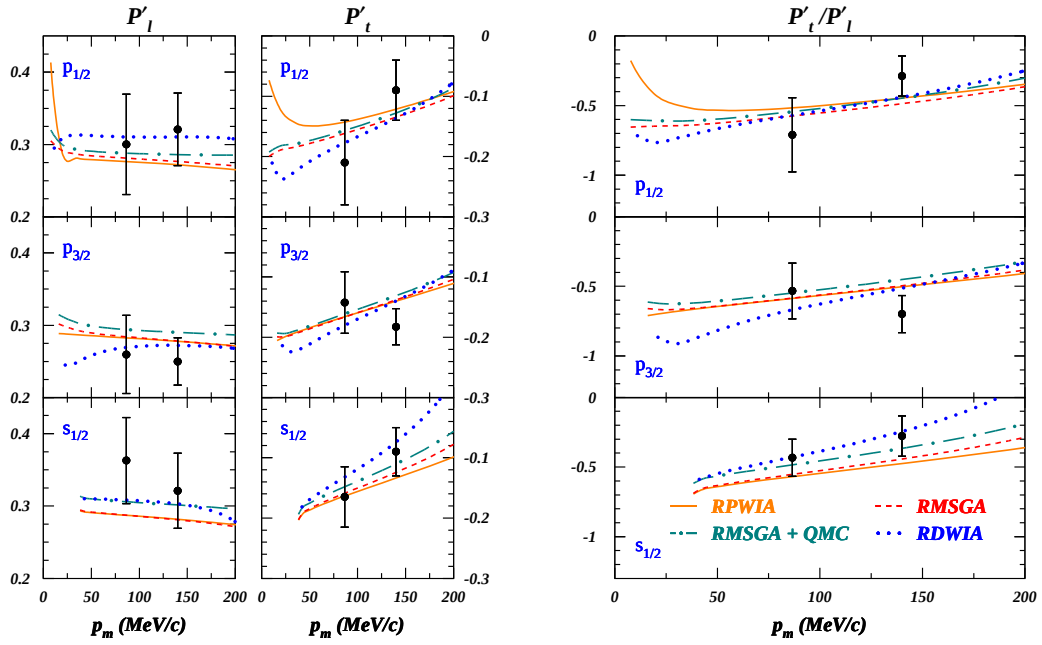

Figure 4.10 Transferred polarization components for proton knockout from the three shells in ^{16}O for Q^2=0.8 (GeV/c)^2 in constant $(\vec{q}, \omega)$ kinematics. The dashed (solid) curve represents RMSGA (RPWIA) calculations with free-nucleon form factors, while the dot-dashed curve is obtained from RMSGA calculations when using the QMC form factors. The dotted curve represents RDWIA calculations. Data points are from [45].

Finally, in Fig. 4.10, results for the transferred polarization components and their ratio for the ^{16}O nucleus are shown at Q^2=0.8 (GeV/c)^2. Hereby, we adopt constant $(\vec{q}, \omega)$ kinematics and compare the RMSGA predictions with the measurements of Ref. [45] and the results of the RDWIA model from the Madrid group. For the oxygen calculations, the RDWIA and RMSGA calculations adopt identical mean-field wave functions (W1 parametrization) and current operators ($CC2$ in the Coulomb gauge). The RDWIA calculations are performed with the EDAD1 parametrization for the optical potential [154]. The RPWIA and RMSGA curves for P'_l and P'_t are close, the RDWIA model predicting larger FSI distortions. At corre-

sponding Q^2 values (Figs. 4.6 and 4.7), the ^{4}He results could be better reproduced after introducing QMC medium-modified form factors. As can be appreciated from Fig. 4.10, the ^{16}O data do not allow one to draw conclusions on the possibility of medium modifications. The overall trends of the ^{16}O polarization-transfer data are reasonably reproduced in the RMSGA, using free-proton electromagnetic form factors. When comparing the RMSGA and RMSGA+QMC curves a significant orbital dependence of the magnitude of the medium effect is observed. The RMSGA+CQS curves are not shown but can hardly be discriminated from the RMSGA+QMC results. Comparing the results for R for the various orbitals in a particular nucleus could allow one to study the density dependence of the medium effects.

In conclusion, concerning the ^{16}O target, for which the data are restricted to Q^2=0.8 (GeV/c)^2, the calculations provide a fair description when adopting free-proton electromagnetic form factors. A similar situation holds for the ^{4}He case at $Q^2 \geq$1.6 (GeV/c)^2. For ^{4}He and $Q^2 \leq$1.0 (GeV/c)^2 substantial deviations between the RMSGA predictions and the data are observed when adopting electromagnetic form factors for free protons. Under these circumstances, the implementation of the in-medium form factors from the QMC and CQS nucleon models, makes the RMSGA calculations to go in the right direction and induces changes in the ratio of the polarization-transfer components, which are of the right order of magnitude to explain the discrepancies. Recent calculations performed by Schiavilla *et al.* [155] challenge this interpretation of the experimental data in terms of medium-modified form factors. A non-relativistic framework was employed, including correlation effects in both the initial and final nucleon wave functions. In addition, this model accounts for many-body terms in the electromagnetic current, and FSI mechanisms are described with the aid of optical potentials. The description of FSI effects, however, may not be reliable for $Q^2 \geq 1.6$ (GeV/c)^2, since the relevant proton kinetic energies require uncontrolled extrapolations of the optical model. The quenching in the double ratio R is explained by means of charge exchange processes and two-body current contributions. In particular the charge exchange processes, which are absent in the RMSGA and RDWIA frameworks, are crucial to reproduce the experimental data when free electromagnetic form factors are adopted. A recently approved experiment at JLAB [156] will address the polarization-transfer ratio at Q^2-values of 0.8 and 1.3 (GeV/c)^2, and is expected to reduce the statistical uncer-

tainties by over a factor of two compared to the previous round of measurements.

4.2 Induced normal polarization

Whereas the transferred polarization components P'_l and P'_t are usually studied to look for possible modifications of the nucleon in a dense baryonic environment, the induced normal polarization component P_n rather serves as a stringent test for models dealing with FSI mechanisms. Indeed, in the one-photon exchange approximation, P_n naturally vanishes in the absence of FSI.

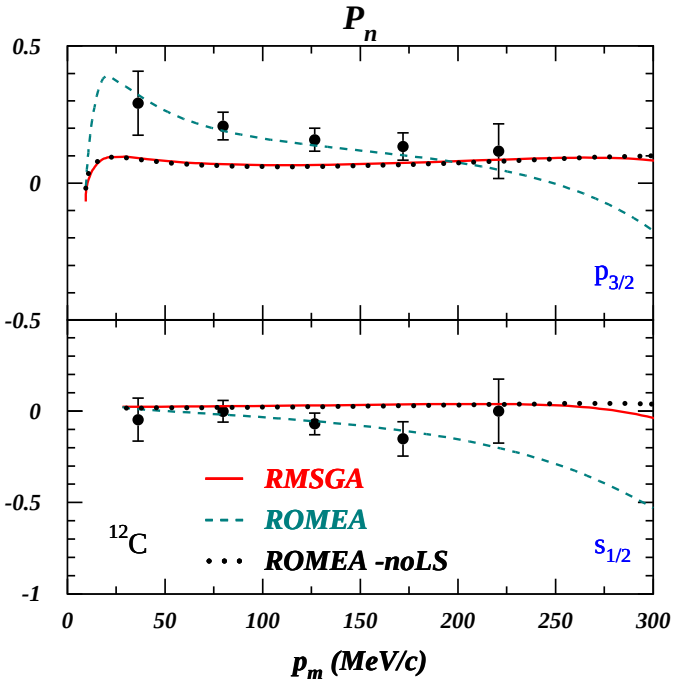

Figure 4.11 Induced polarization of the knocked-out proton in the ^{12}C$(e, e'\vec{p})$ reaction at ε=579 MeV, q=760 MeV, ω=292 MeV and ϕ=180°. The curves refer to predictions obtained within RMSGA (solid) and ROMEA (dashed) frameworks. The dotted lines represent ROMEA calculations, with the spin-orbit and Darwin part turned off. The data are from [157].

The first experiment measuring the induced normal polarization on a nucleus heavier than deuterium was carried out at Bates by Woo *et al.* [157] for the ^{12}C$(e, e'\vec{p})$ reaction. The measurement was performed at ε=579 MeV, ω=292 MeV and q=760

MeV, yielding Q^2=0.5 (GeV/c)^2. The azimuthal angle corresponds to ϕ=180^o. The first analysis of the experiment was made in a non-relativistic DWIA, and yielded a systematic underestimation of P_n of around 10% at best [157]. The RDWIA calculations of Ref. [89] are in very close agreement to the data, emphasizing the importance of dynamical relativistic effects. In Ref. [134], the effects of meson and isobar degrees of freedom were studied, and emerged to be of minor importance for $p_m \leq 250$ (MeV/c). Figure 4.11 shows the predictions obtained by the RMSGA and ROMEA frameworks and compares them to the data. As can be inferred, the ROMEA calculations are in line with the RDWIA calculations of Ref. [89], nearly reproducing the data for both single-particle orbitals. Apparently, the eikonal approach is well justified for this kind of observables and kinetic energies as low as 250 MeV. The RMSGA predicts a P_n which is close to zero over the entire missing momentum range. Since the eikonal approximation turns out to be adequate, the origin of the failure of the RMSGA in this particular situation is likely to stem from another source. In order to investigate this, in the ROMEA calculation we switched off the contributions from the spin-orbit potential V_{so} to the eikonal phase of Eq. (2.64). After all, the RMSGA framework as it was introduced earlier in this work, retains only spin-independent nucleon-nucleon scattering amplitudes. We stress that both the spin-dependent term $(\vec{\sigma} \cdot (\vec{b} \times \vec{K}))$ and the so-called Darwin term (iKz') are set to zero in the curves denoted as ROMEA-noLS. Though not shown, our calculations reveal that the impact of the Darwin term on P_n is negligible. As can be inferred from Fig. 4.11, the spin-orbit term gains in importance with rising missing momenta, which complies with other studies [109]. Furthermore, the ROMEA-noLS curves are very close to the Glauber ones for $p_m \leq 250$ (MeV/c). This suggests that the spin-orbit amplitude may be at the origin of the large deviations between the Glauber and optical-potential predictions for P_n.

Recently, the importance of spin-dependent amplitudes in the framework of Glauber theory has been studied for the deuteron [81] and ^{3}He [82]. They emerged of marginal importance for $p_m \leq 300$ (MeV/c) in the longitudinal-transverse asymmetry [82], and were shown to play only a crucial role in the $\mathcal{R}'_{TL}$ response [81]. We remark that the $\mathcal{R}'_{TL}$ response does not contribute to the calculation of induced polarization components. As such, it is not clear whether or not the spin-dependent nucleon-nucleon amplitudes can explain the discrepancies appearing

in Fig. 4.11. In the future, attempts will be made to include spin-orbit interactions in the RMSGA framework.

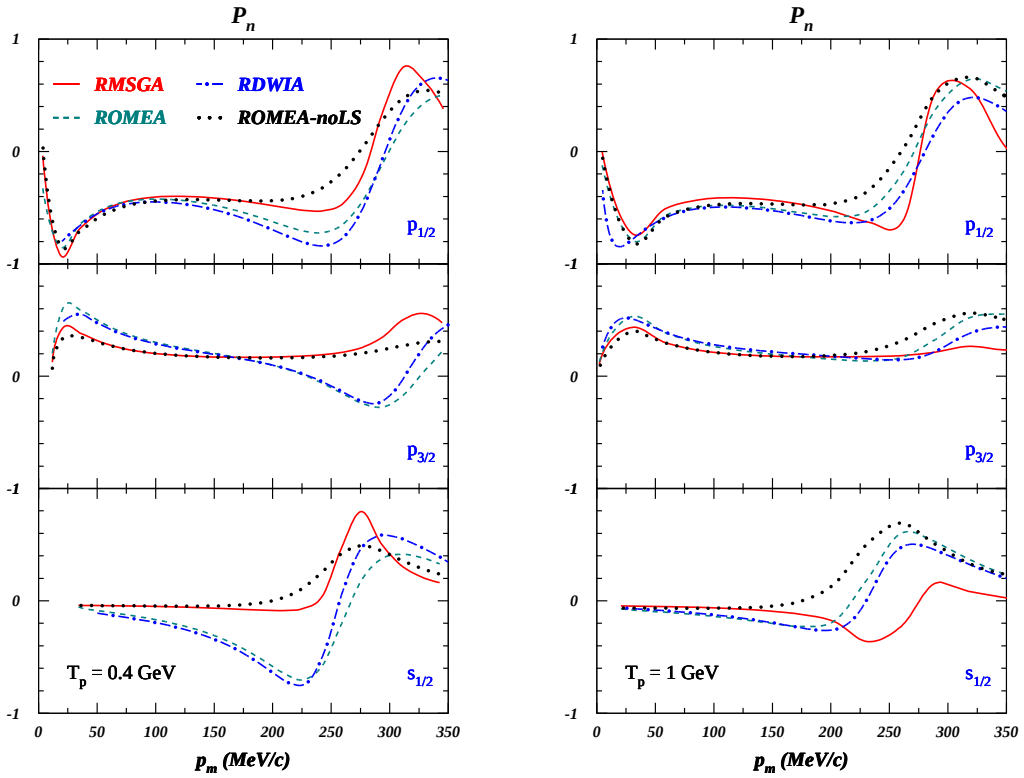

Figure 4.12 Induced polarization of the knocked-out proton in the ^{16}O$(e, e'\vec{p})$ reaction at T_p=0.4 GeV (left panel) and at T_p=1 GeV (right panel). Calculations for RMSGA (solid), ROMEA (dashed) and RDWIA (dot-dashed) are plotted. The dotted lines represent ROMEA calculations, with the neglection of the spin-orbit and Darwin parts.

In the past, studies in the Dirac eikonal approach have stressed the importance of the spin-orbit part in the optical potential for computed values of the induced normal polarization for the ^{16}O$(e, e'\vec{p})$ reaction [73]. Figure 4.12 displays calculations for this same reaction at two ejectile kinetic energies. The EDAD1 potential is employed for the RDWIA and ROMEA calculations. Once again, the RDWIA and ROMEA curves nearly reproduce each other, corroborating the use of the eikonal approach. Switching of the spin-orbit part in the ROMEA framework shifts its pre-

dictions to the RMSGA ones. The importance of the spin-orbit part, however, dwindles with increasing ejectile kinetic energies. Similar conclusions were reported in Ref. [73].

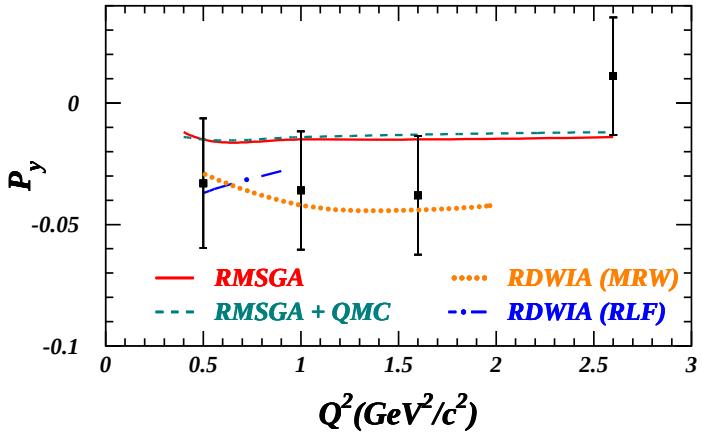

Figure 4.13 The induced normal polarization as a function of Q^2 in ^{4}He. The solid curve represents RMSGA calculations with free from factors. For the dashed lines $\widetilde{G}_{E,M}^{QMC}(Q^2, \rho(\vec{r}))$ form factors are used. Data points and RDWIA results are from Ref. [9].

Finally, Fig. 4.13 displays the induced normal polarization as a function of Q^2 for the ^{4}He nucleus. The data were collected at JLAB [9]. As for the transferred polarization components, results for the induced polarization are obtained by averaging over the experimental acceptance. The smallness of P_y suggests moderate FSI mechanisms. The RDWIA calculations for P_y are shown for exactly the same kinematics, though with the $CC1$ choice for the current operator. The other curves adopt the $CC2$ form. The RDWIA predictions for the P_y in ^{4}He$(e, e'\vec{p})$ are presented for two viable choices of the optical-potential parametrization : "RLF" (limited to proton lab kinetic energies smaller than 0.4 GeV) and "MRW" (limited to proton lab kinetic energies smaller than 1.0 GeV). The two optical potentials predict a dissimilar Q^2 dependence for P_y. Indeed, in many cases various optical potentials can fit the elastic proton-nucleus data equally well, but do not necessarily lead to identical predictions in electromagnetically induced nucleon knockout. The RDWIA

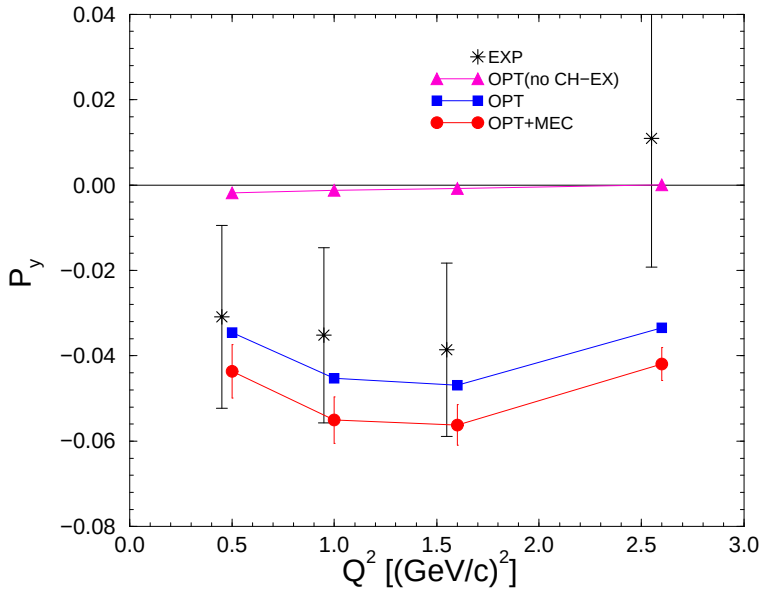

Figure 4.14 The induced normal polarization as a function of Q^2 in ^{4}He. The picture is taken from Ref. [82]. The triangles refer to "bare" non-relativistic optical potential calculations. The squares include the effects of charge exchange (CH-EX), whereas the circles account for MEC and CH-EX.

model predicts values for P_y that are over twice as large as the RMSGA ones. As stated above, this may be due to the importance of the spin-orbit part in the optical potential for the computed values of P_y. The smallness of the measured value of P_y at Q^2=2.6 (GeV/c)^2 may point to the decreasing role of the spin-dependent part in the distorting potentials as the energy increases. As can be inferred, P_y remains nearly unaffected by medium modifications in the electromagnetic form factors. This is not unexpected given that P_y is an observable which quantifies the magnitude of secondary processes, like rescattering mechanisms. The introduction of medium-modified form factors induces some change in the way these mechanisms are folded over the density of the target nucleus.

Fig. 4.14 displays the predictions of Schiavilla *et al.* [82] for the normal induced polarization in ^{4}He. For a brief description of the employed model, the reader is referred to section 4.1.2. As outlined there, this optical potential model challenges the interpretation of experimental data in terms of medium-modified form factors. In Fig. 4.14 , the triangles refer to "bare" non-relativistic optical potential calculations.

The squares include the effects of charge exchange FSI mechanisms, whereas the circles account in addition for two-body current contributions. In accordance with the conclusions drawn for the polarization-transfer ratio, the inclusion of charge exchange processes are crucial for reliably reproducing the P_y data. We stress, however, that the model calculations for the highest Q^2 values are subject to large uncertainties, due to the extrapolation of the optical potentials. It is remarkable that P_y receives a good description in both the "MRW" RDWIA model of Udias and the model of Schiavilla. Whereas the Schiavilla model stresses the role of charge exchange processes, however, we are rather inclined to emphasize the importance of the spin-orbit part in the optical potential for the computed values of P_y.

In conclusion, we can say that the RMSGA framework in its present form, i.e. relying on spin-independent nucleon-nucleon scattering amplitudes, is open for improvement with respect to the description of certain polarization observables. The spin-dependent effects, however, are expected to lose in importance with increasing energies. Polarization studies with the electromagnetic probe, such as the ones presented here, will help in further clarifying this issue.

4.3 A_{LT} asymmetries in ^{12}C and ^{16}O

During the last decade, the longitudinal-transverse interference response function $\mathcal{R}_{TL}$ has attracted a lot of attention, as it turned out to be an observable sensitive to spin mechanisms in the distorting nucleon-nucleus potentials [15, 89, 109, 158, 159]. A quantity that reflects this sensitivity is the left-right asymmetry

$$A_{LT} = \frac{\sigma(\phi = 0^o) - \sigma(\phi = 180^o)}{\sigma(\phi = 0^o) + \sigma(\phi = 180^o)} = \frac{v_{TL}\mathcal{R}_{TL}}{v_L\mathcal{R}_L + v_T\mathcal{R}_T + v_{TT}\mathcal{R}_{TT}} \ . \tag{4.8}$$

From an experimental point of view, A_{LT} is a particularly useful quantity as it is systematically much less challenging to extract than either an absolute cross section or an effective response function. From a theoretical point of view, this ratio has the major advantage of being independent of the spectroscopic factors and is very well suited to scrutinize different ingredients that enter various model calculations. Indeed, subtilities that remain concealed in other observables may become prominent in the A_{LT} asymmetry. Slight changes in the applied current operator, dynamical and kinematical relativistic effects, factorization properties, and

two-body current mechanisms have been widely investigated the last few years [109, 133, 138, 160, 161].

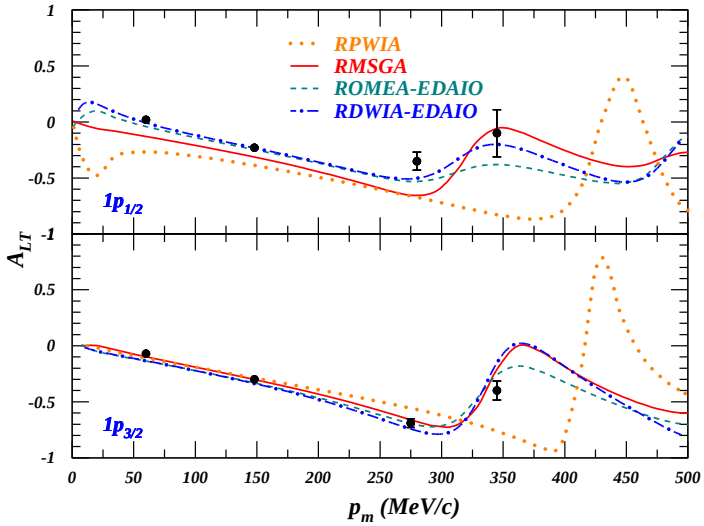

Figure 4.15 The left-right asymmetry A_{LT} for the ^{16}O$(e, e'p)$ experiment of [45]. The dotted, solid, dashed and dot-dashed lines show the predictions of RPWIA, RMSGA, ROMEA and RDWIA calculations, respectively.

Figure 4.15 shows the left-right asymmetry for the removal of 1p-shell protons of ^{16}O as a function of the missing momentum in the kinematics of Refs. [45, 161]. The data points are also from these references. The figure contains the results of various calculations. Apart from the treatment of FSI, all other ingredients in these calculations are identical. More precisely, all presented curves impose the Coulomb gauge, use the $CC2$ parametrization for the current operator, and $W1$ bound-state wave functions. The EDAIO parametrization for the optical potentials has been employed in the ROMEA and RDWIA formalisms. As can be inferred, the inclusion of FSI in the various models is particularly visible at high missing momentum. The structure in A_{LT} which is located at $p_m \approx 400$ (MeV/c) in RPWIA, is shifted to lower values of the missing momentum. This shift is essential to describe the data at $p_m \approx 350$ (MeV/c).

It is clear that the RDWIA formalism provides the best description of the data over the entire momentum range. However, in view of the adopted eikonal approach, the ROMEA calculations do a remarkable job up to $p_m \approx 350$ (MeV/c). The Glauber formalism does well with the overall trends, but yields a too large asymmetry for the $1p1/2$-state. This is not surprising if we reconsider Fig. 3.1, where the largest deviations arose for the $j = l - 1/2$ spin-orbit partner of the p-shell. In line with the conclusions drawn for the induced normal polarization, the absence of spin-dependent FSI mechanisms in the Glauber formalism may partly explain this deviation. The "stretched" spin-orbit partner, on the other hand, receives a very good description in the context of nucleon-nucleon scattering data. It is a very striking feature that the Glauber model, on the one hand, and the optical models, on the other hand, agree to such a high degree, not only for integrated quantities, but also for observables which are extremely sensitive to the details of the calculations.

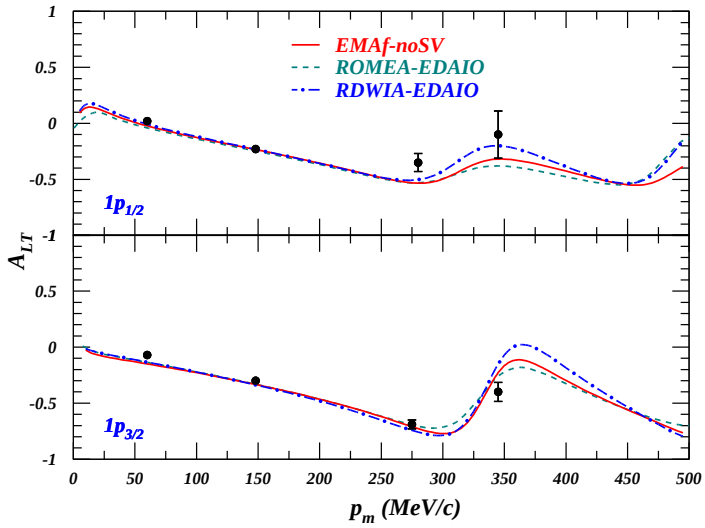

Figure 4.16 The left-right asymmetry A_{LT} for the ^{16}O$(e, e'p)$ experiment of [45] at Q^2=0.8 (GeV/c)^2. The dashed (dot-dashed) lines show the results of the ROMEA (RDWIA) calculations. The solid line displays the predictions of EMAf-noSV, neglecting spinor distortions in the scattered wave.

In Ref. [109, 161], the structure in A_{LT} at $p_m \approx 350$ (MeV/c) is explained in

terms of the distortion of the bound-nucleon and ejectile spinors. In peculiar, the distortion of the former ones are essential to obtain the large change in the slope at $p_m \approx 300$ (MeV/c). In section 2.4.1, however, it was outlined that in the ROMEA formalism, ejectile distortions are omitted in the sense that the impulse operator $\hat{\vec{p}}$ in Eq. (2.63) is replaced by the outgoing nucleon momentum $\vec{k}_f$. Figure 4.16 displays the ROMEA and RDWIA A_{LT}-predictions of Fig. 4.15. In addition, we present the results from an RDWIA calculation where only bound-nucleon spinor distortions are retained, and dubbed them EMAf-noSV. This refers to the fact that in computing the scattering state the EMA is adopted in combination with the neglect of the dynamical enhancement of the lower components. As can be inferred, the agreement between the ROMEA and the EMAf-noSV curves is excellent up to extreme high missing momenta of approximately 450 (MeV/c).

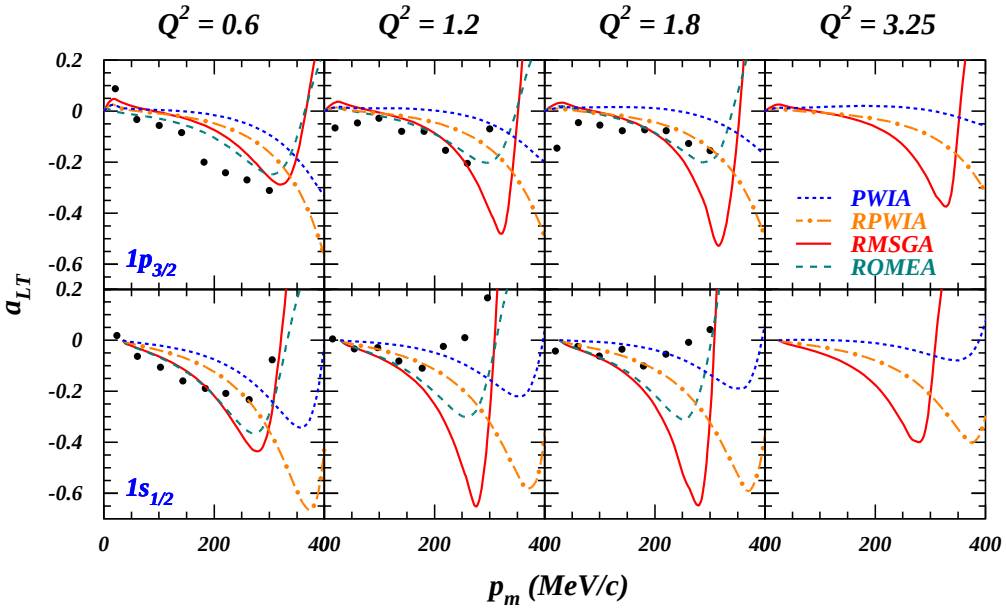

Figure 4.17 The left-right asymmetry for reduced cross sections for the ^{12}C$(e, e'p)$ experiment of [7] at Q^2=0.6, 1.2, 1.8 and 3.25 (GeV/c)^2. The dotted, dot-dashed, solid and dashed curves refer to PWIA, RPWIA,RMSGA and ROMEA calculations, respectively.

Recently, Dutta *et al.* measured reduced cross sections for ^{12}C$(e, e'p)$ in quasiper-

pendicular kinematics, aiming to extract nuclear transparencies [7]. The corresponding left-right asymmetry for reduced cross sections reads

$$a_{LT} = \frac{S(\phi = 0^o) - S(\phi = 180^o)}{S(\phi = 0^o) + S(\phi = 180^o)} \, , \tag{4.9}$$

with S defined by Eq. (3.3). This quantity is particular useful to measure the degree of factorization. In a factorized approach, the reduced cross section emerges as

$$S(\vec{p}_m, E_m, \vec{k}_f) \longrightarrow S(\vec{p}_m, E_m) \, , \tag{4.10}$$

with $S(\vec{p}_m, E_m)$ the spectral function describing the probability of finding a proton in the target nucleus with energy E_m and momentum $\vec{p}_m$. It is obvious that this probability does not depend on the azimuthal angle. Hence, in a factorized framework the a_{LT} should naturally vanish. The breakdown of factorization and the sensitivity of a_{LT} to spinor distortions was studied in some detail in Ref. [162]. Similar conclusions were drawn as for the left-right asymmetry A_{LT} in total cross sections. In particular, it was shown that spinor distortions are more important for the bound state than for the ejectile. The net effect of these dynamical relativistic effects, however, was found to decrease with Q^2.

Figure 4.17 displays our PWIA, RPWIA, ROMEA and RMSGA calculations for the reduced asymmetry a_{LT} at four different Q^2 values, and compares them to the data of Ref. [7]. In a fully non-relativistic PWIA model, one expects that factorization holds true and a_{LT} should yield zero. Our PWIA results, however, still account for spinor distortions in the bound-state wave functions and accordingly show some structure in a_{LT}. The agreement with zero improves, however, with rising Q^2. Hence, the net effect of spinor distortions dwindles with increasing energies, corroborating the findings of Ref. [162].

In line with the conclusions drawn for A_{LT}, the inclusion of FSI is essential for a reliable comparison of a_{LT} with the data. In particular, FSI induce a shift of the structure in a_{LT} located at $p_m \approx 400$ (MeV/c) to lower values of the missing momentum. The ROMEA predictions describe the p-shell a_{LT} data reasonably well and are in line with the RDWIA calculations of Ref. [162]. The RMSGA calculations, on the other hand, are in fair agreement with the ROMEA ones up to $p_m \approx 200$ (MeV/c). Beyond this value, a much larger dip is yielded in the Glauber approximation. The s-shell measurements show much less variation with p_m than

the calculations once Q^2 exceeds 1.2 (GeV/c)^2. It is not clear where this flattening originates from. One may argue that the primary "crime suspects" are continuum contributions that dilute the signal from single-nucleon knockout. There is, however, very little reason to believe that multinucleon knockout can retain the characteristic left-right asymmetry of single-nucleon knockout. Besides, the p-shell data at Q^2=1.8 (GeV/c)^2 point towards a vanishing profile in a_{LT} and are not contaminated by the continuum to such a degree, since the corresponding missing energies are well below two-nucleon emission threshold.

It is remarkable that our predictions, the ROMEA ones in particular, agree to such a high degree with the A_{LT} data of the ^{16}O experiment, wheras they tend to fail for the reduced cross section asymmetry in ^{12}C.

Chapter 5

Quasi-elastic neutrino-nucleus interactions

5.1 Introduction

The previous chapters dealt with issues in electron scattering from atomic nuclei. The construction and the planning of new experimental facilities with the objective of detecting neutrino interactions, however, has generated great interest in neutrino-nucleus scattering processes. Indeed, neutrinos are ubiquitous but remain elusive particles, since their presence can only be inferred by detecting the secondary particles they create when colliding and interacting with dense matter. Nuclei are often used as neutrino detectors, providing the required magnitude of cross sections that make the measurements experimentally feasible. As a consequence, a reliable interpretation of data involving neutrinos heavily relies on a detailed knowledge of neutrino-nucleus interactions under various circumstances. A precise knowledge of the energy and mass number dependence of the neutrino-nucleus cross section is essential to current and future measurements.

Just as electromagnetic probes, neutrinos can frisk the entire nuclear volume, thereby leaving the structure undisturbed. Glashow, Weinberg and Salam unified the electromagnetic and the weak interaction in the standard model for electroweak interactions. The tight connection between the electromagnetic and the weak interaction makes the extension of electron scattering formalisms to neutrino ones straightforward. Accordingly, at intermediate energies (here defined as en-

ergies beyond the nuclear resonance region), neutrino-nucleus interactions have been studied within several approaches, which were initially designed for the description of electron-nucleus scattering processes. The relativistic Fermi gas (RFG) model was employed in Refs. [163, 164, 165] to study the possibility of measuring strange-quark contributions to the nucleon form factors. The RFG takes into account the Fermi motion of the nucleons inside the nucleus, Pauli blocking and relativistic kinematics, but neglects several other effects. Refs. [166, 167] used a non-relativistic mean-field approach with Gaussian bound-state wave functions and plane-wave continuum states to estimate polarization-asymmetry effects in neutrino-induced nucleon knockout. Relativistic nuclear effects were included in the calculations of Refs. [168, 169, 170, 171, 172, 173], using a relativistic shell-model approach for the study of neutral-current and/or charged-current neutrino-nucleus scattering. In particular, in Refs. [168, 169, 170, 174] results in the RPWIA were compared to RFG calculations. It is shown that binding-energy effects tend to vanish as the energy increases. Going one step further in the complexity of the model calculation, the implementation of the FSI of the ejected nucleon has been performed in different manners. In Ref. [175] a phenomenological convolution model was applied to the RFG, showing that nucleon re-scattering can produce a reduction of the quasi-elastic cross section as large as 15% at incoming neutrino energies of about 1 GeV. A description of FSI mechanisms through the inclusion of relativistic optical potentials is presented in Refs. [168, 169, 170, 171, 172]. More specifically, Ref. [170] studies the uncertainties derived from the use of different prescriptions for the potentials. A reduction of the cross section of at least 14% is found at incoming neutrino energies of 1 GeV. In Refs. [171, 172], important FSI effects arise from the use of relativistic optical potentials within a relativistic Green's function approach. Apart from relativistic dynamics and FSI, other effects may have an impact on neutrino-nucleus reactions. In Refs. [176, 177, 178] the influence of relativistic nuclear structure effects, delta and pion degrees-of-freedom, and RPA-type correlations on neutrino-scattering cross sections was examined. In Refs. [179, 180], the BUU-transport model was extended to predict coherent pion-production in neutrino-nucleus interactions. Ref. [181] includes long-range correlations, FSI and Coulomb corrections in $^{12}C(\nu_\mu, \mu^-)^{12}C^*$ calculations. An alternative method was proposed in Ref. [182], where it was shown that a superscaling analysis of few-GeV

inclusive electron-scattering data allows one to predict charged-current neutrino cross sections in the nuclear resonance region, thereby effectively including delta isobar degrees-of-freedom.

In this chapter we compute the single-nucleon knockout contribution (often referred to as quasi-elastic (QE)) to the inclusive neutrino-nucleus cross sections, for energies and nuclei relevant to proposals like Minerνa [30], Miniboone [183] and FINeSSE [33]. It is important to note that the above connotation of QE differs from the one employed in exclusive processes like $A(e,e'p)$, which refers to $x \approx 1$. We judge that the large variety of relevant neutrino energies and the tendency to study neutrino-nucleus interactions at increasing energies, necessitate the use of relativity. We adopt the relativistic multiple-scattering Glauber approximation, outlined in chapter 2, to describe FSI in neutrino-nucleus interactions. In addition, we compare our results with the ones of the RDWIA model, that has already been employed in several neutrino-nucleus calculations [168, 169, 170]. The aim of this work is threefold. First, the relativistic models available to date predict different results in the limit of vanishing FSI, motivating a 'new round' of calculations. We aim at providing benchmark RPWIA for νA cross sections. To this end, we investigate the plane-wave limit of the RDWIA and RMSGA approaches. Second, we compute the effects of FSI within our models, paying special attention to the comparison between RDWIA and RMSGA results. It is well known that computing the effect of FSI on inclusive calculations is a challenging task. We propose a way to estimate FSI effects for the QE contribution to the inclusive neutrino-nucleus cross section using benchmark RPWIA results and transparency data from $A(e,e'p)$ experiments. The effects of many-body currents, nucleon-nucleon correlations, and contributions beyond quasi-elastic scattering processes as multi-nucleon processes and pion production are neglected. Finally, we focus on possible strange-quark contributions to the nucleon form factors. These are accessible due to the parity-violating character of the weak interaction and have gained wide interest during the last decade.

The outline of this chapter is as follows. In Sec. 5.2 we present the RMSGA formalism for the description of the neutral- and charged-current neutrino-nucleus scattering processes. Cross-section results are shown in Sec. 5.3. In Sec. 5.4 we study the strangeness content of the nucleon in neutrino-nucleus interactions. This

chapter is based on the results and discussions of Refs. [184, 185].

5.2 Formalism

We derive expressions for neutrino and antineutrino neutral-current (NC) reactions from nuclei which result in one emitted nucleon

$$\nu(\overline{\nu}) + A \Longrightarrow \nu(\overline{\nu}) + N + (A-1). \tag{5.1}$$

We also consider their charged-current (CC) counterparts

$$\nu_l(\overline{\nu}_l) + A \Longrightarrow l^-(l^+) + N + (A-1). \tag{5.2}$$

Here, l labels the flavor of the lepton, and A represents a nucleus with mass number A. The connection between electromagnetic and weak interactions makes that the analytical derivations go along the same lines as those used in the electron-nucleus scattering formalism of chapter 2. The main differences between neutrino and electron interactions stem from the intrinsic polarization of the neutrino due to the parity-violating character of the weak interaction. Moreover, in weak interactions the focus is on inclusive processes, whereas exclusive processes play a predominant role in current subatomic research with electrons.

Here, the same approximations and conventions are employed as discussed in section 2.1. In particular, we describe the processes of Eqs. (5.1,5.2) at lowest order in the electroweak interaction, i.e. considering the exchange of one gauge boson. In addition, we adopt an identical nomenclature to describe the different variables. More precisely, the four-momenta of the incident neutrino and scattered lepton are labeled K^μ and K'^μ. Further, K^μ_A, K^μ_{A-1} and K^μ_f represent the four-momenta of the target nucleus, the residual nucleus and the ejected nucleon. The four-momentum transfer is given by $q^\mu = (\omega, \vec{q}) = K^\mu - K'^\mu = K^\mu_{A-1} + K^\mu_f - K^\mu_A$ .The xyz coordinate system, the scattering plane and the hadron reaction plane are defined identically as displayed in Fig. 2.1.

5.2.1 Quasi-elastic neutrino-nucleus cross section

In the laboratory frame, the exclusive differential cross section for the processes specified in Eqs. (5.1) and (5.2) can be written as (cfr. Eq. (2.1))

$$\begin{aligned} d\sigma &= \frac{1}{\beta}\overline{\sum_{if}}|M_{fi}|^2\frac{M_l}{\varepsilon'}\frac{M_{A-1}}{E_{A-1}}\frac{M_N}{E_f}d^3\vec{k}_{A-1}d^3\vec{k}'d^3\vec{k}_f \\ &\times (2\pi)^{-5}\delta^4(K^\mu + K_A^\mu - K'^\mu - K_{A-1}^\mu - K_f^\mu). \end{aligned} \tag{5.3}$$

Dealing with neutrinos, the relative initial velocity β can trivially be put to 1. The factor $\frac{M_l}{\varepsilon'}$ stems from the normalization of the outgoing lepton spinor and becomes 1 for NC reactions. Integrating over the unobserved momentum of the recoiling nucleus $\vec{k}_{A-1}$, as well as over $|\vec{k_f}|$, results in the following five-fold differential cross section for the $A(\nu,\nu'N)$, $A(\overline{\nu},\overline{\nu}'N)$, $A(\nu_l,l^-N)$ and $A(\overline{\nu}_l,l^+N)$ reactions

$$\frac{d^5\sigma}{d\varepsilon' d^2\Omega_l d^2\Omega_f} = \frac{M_l M_N M_{A-1}}{(2\pi)^5 M_A \varepsilon'}k'^2 k_f f_{rec}^{-1}\overline{\sum_{if}}|M_{fi}|^2, \tag{5.4}$$

where Ω_l and Ω_f define the scattering direction of the outgoing lepton and the outgoing nucleon. The recoil factor f_{rec} is given by Eq. (2.4).

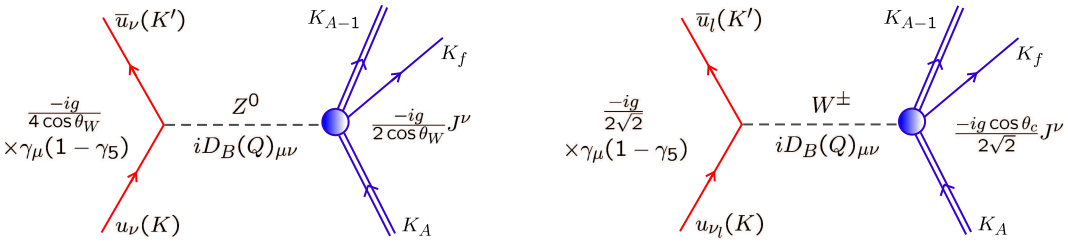

Figure 5.1 Lowest order diagrams corresponding to the exclusive neutrino-nucleus scattering processes. The left and right panels display neutral- and charged-current interactions, respectively.

A diagram for the exclusive scattering processes of Eqs. (5.1,5.2) can be found in Fig. 5.1. The gauge boson is represented by the propagator

$$D_B(Q)_{\mu\nu} = \frac{-g_{\mu\nu} + \frac{q_\mu q_\nu}{M_B^2}}{q^2 - M_B^2}, \tag{5.5}$$

with M_B the mass of the Z-boson (91.188 GeV) for NC reactions and that of the $W^\pm$-boson (80.1 GeV) for CC processes.

The squared invariant matrix element M_{fi} can now be written as

$$\overline{\sum_{if}}|M_{fi}|^2 = \frac{G_F^2}{2}\left[\frac{M_B^2}{Q^2+M_B^2}\right]^2 l_{\alpha\beta}W^{\alpha\beta}, \tag{5.6}$$

with G_F=$\frac{\sqrt{2}g^2}{8M_W^2}$ the Fermi constant. For CC reactions the latter has to be multiplied with a factor $\cos\theta_c$=0.974. This is the Cabbibo angle, determining the mixing of the strong down and strange quarks into the weak d-quark. In the above expression the lepton tensor is defined as

$$l_{\alpha\beta} \equiv \overline{\sum_{s,s'}}[\overline{u}_l\gamma_\alpha(1+h\gamma_5)u_l]^\dagger[\overline{u}_\nu\gamma_\beta(1+h\gamma_5)u_\nu], \tag{5.7}$$

with s and s' the initial and final lepton spins. In Eq. (5.7), $h=-1$ ($h=+1$) corresponds to the helicity of the incident neutrino (antineutrino). The hadron tensor is given by

$$W^{\alpha\beta} = \overline{\sum_{if}}\langle\Delta^{\alpha\mu}J_\mu\rangle^\dagger\langle\Delta^{\beta\nu}J_\nu\rangle = \overline{\sum_{if}}\langle\mathcal{J}^\alpha\rangle^\dagger\langle\mathcal{J}^\beta\rangle, \tag{5.8}$$

with

$$\Delta^{\mu\nu} = g^{\mu\nu} - \frac{q^\mu q^\nu}{M_B^2}. \tag{5.9}$$

The quantity $\langle\mathcal{J}^\alpha\rangle$ in Eq. (5.8) reflects the one of Eq. (2.8), i.e.

$$\langle\mathcal{J}^\alpha\rangle \equiv \left\langle(A-1)(J_RM_R), K_f(E_f,\vec{k}_f)m_s\left|\Delta_{\alpha\mu}\hat{J}^\mu\right|A(0^+,g.s.)\right\rangle, \tag{5.10}$$

with $\hat{J}^\mu$ the weak current operator. At the energies considered here, Eq. (5.9) can approximately be written as $\Delta^{\mu\nu}\approx g^{\mu\nu}$, and the quantity $\langle\mathcal{J}^\alpha\rangle\approx\langle J^\alpha\rangle$, re-establishing the connection between the four-vector $\mathcal{J}^\alpha$ and the nuclear current operator. Since the extreme relativistic limit is naturally valid for neutrinos, the contraction of the lepton tensor $l_{\alpha\beta}$ with the nuclear one $W^{\alpha\beta}$ in Eq. (5.6) can be cast in the form [41] :

$$\begin{aligned}\frac{d^5\sigma}{d\varepsilon' d^2\Omega_l d^2\Omega_f} &= \frac{M_N M_{A-1}}{(2\pi)^3 M_A}k_f f_{rec}^{-1}\sigma_M^{Z,W^\pm} \\ &\times\left[v_L R_L + v_T R_T + v_{TT}R_{TT}\cos 2\phi\right. \\ &\left. + v_{TL}R_{TL}\cos\phi + h(v'_T R'_T + v'_{TL}R'_{TL}\cos\phi)\right],\end{aligned} \tag{5.11}$$

with σ_M a "Mott-like" cross section defined by

$$\sigma_M^Z = \left(\frac{G_F \cos(\theta_l/2)\varepsilon' M_Z^2}{\sqrt{2}\pi(Q^2 + M_Z^2)} \right)^2, \tag{5.12}$$

for NC reactions and

$$\sigma_M^{W^\pm} = \sqrt{1 - \frac{M_l^2}{\varepsilon'^2}} \left(\frac{G_F \cos(\theta_c)\varepsilon' M_W^2}{2\pi(Q^2 + M_W^2)} \right)^2, \tag{5.13}$$

for CC reactions. In these equations, θ_l is the angle between the direction of the incident and the scattered lepton's momentum and ϕ the azimuthal angle of the reaction plane (see Fig. 2.1). For NC reactions, the lepton kinematics is contained in the kinematic factors

$$\begin{aligned}
v_L &= 1, && (5.14)\\
v_T &= \tan^2\frac{\theta_l}{2} + \frac{Q^2}{2|\vec{q}|^2}, && (5.15)\\
v_{TT} &= -\frac{Q^2}{2|\vec{q}|^2}, && (5.16)\\
v_{TL} &= -\frac{1}{\sqrt{2}}\sqrt{\tan^2\frac{\theta_l}{2} + \frac{Q^2}{|\vec{q}|^2}}, && (5.17)\\
v'_T &= \tan\frac{\theta_l}{2}\sqrt{\tan^2\frac{\theta_l}{2} + \frac{Q^2}{|\vec{q}|^2}}, && (5.18)\\
v'_{TL} &= \frac{1}{\sqrt{2}}\tan\frac{\theta_l}{2}. && (5.19)
\end{aligned}$$

The corresponding response functions read

$$\begin{aligned}
R_L &= \left| \langle \mathcal{J}^0(\vec{q}) \rangle - \frac{\omega}{|\vec{q}|} \langle \mathcal{J}^z(\vec{q}) \rangle \right|^2, && (5.20)\\
R_T &= \left| \langle \mathcal{J}^+(\vec{q}) \rangle \right|^2 + \left| \langle \mathcal{J}^-(\vec{q}) \rangle \right|^2, && (5.21)\\
R_{TT}\cos 2\phi &= 2\Re \left\{ \langle \mathcal{J}^+(\vec{q}) \rangle^* \langle \mathcal{J}^-(\vec{q}) \rangle \right\}, && (5.22)\\
R_{TL}\cos\phi &= -2\Re \left\{ \left[\langle \mathcal{J}^0(\vec{q}) \rangle - \frac{\omega}{|\vec{q}|} \langle \mathcal{J}^0(\vec{q}) \rangle \right] \left[\langle \mathcal{J}^+(\vec{q}) \rangle - \langle \mathcal{J}^-(\vec{q}) \rangle \right]^* \right\}, && (5.23)\\
R'_T &= \left| \langle \mathcal{J}^+(\vec{q}) \rangle \right|^2 - \left| \langle \mathcal{J}^-(\vec{q}) \rangle \right|^2, && (5.24)\\
R'_{TL}\cos\phi &= -2\Re \left\{ \left[\langle \mathcal{J}^0(\vec{q}) \rangle - \frac{\omega}{|\vec{q}|} \langle \mathcal{J}^z(\vec{q}) \rangle \right] \left[\langle \mathcal{J}^+(\vec{q}) \rangle + \langle \mathcal{J}^-(\vec{q}) \rangle \right]^* \right\}, && (5.25)
\end{aligned}$$

where $\langle\vec{\mathcal{J}}(\vec{q})\rangle$ is expanded in terms of the unit spherical vectors $\vec{e}_m$ of Eq. (2.25).

For CC reactions, the mass of the outgoing lepton has to be taken into account. This results in the following substitutions

$$v_T = 1 - \sqrt{1 - \frac{M_l^2}{\varepsilon'^2}}\cos\theta_l + \frac{\varepsilon\varepsilon'}{|\vec{q}|^2}\left(1 - \frac{M_l^2}{\varepsilon'^2}\right)\sin^2\theta_l, \tag{5.26}$$

$$v_{TT} = -\frac{\varepsilon\varepsilon'}{|\vec{q}|^2}\left(1 - \frac{M_l^2}{\varepsilon'^2}\right)\sin^2\theta_l, \tag{5.27}$$

$$v_{TL} = \frac{\sin\theta_l}{\sqrt{2}|\vec{q}|}(\varepsilon + \varepsilon'), \tag{5.28}$$

$$v'_T = \frac{\varepsilon + \varepsilon'}{|\vec{q}|}\left(1 - \sqrt{1 - \frac{M_l^2}{\varepsilon'^2}}\cos\theta_l\right) - \frac{M_l^2}{\varepsilon'|\vec{q}|}, \tag{5.29}$$

$$v'_{TL} = -\frac{\sin\theta_l}{\sqrt{2}}\sqrt{1 - \frac{M_l^2}{\varepsilon'^2}}. \tag{5.30}$$

Furthermore

$$R_{TL}\cos\phi = 2\Re\left\{\left[\langle\mathcal{J}^0(\vec{q})\rangle - \frac{\omega + M_l^2}{|\vec{q}|}\langle\mathcal{J}^z(\vec{q})\rangle\right]\left[\langle\mathcal{J}^+(\vec{q})\rangle - \langle\mathcal{J}^-(\vec{q})\rangle\right]^*\right\}, \tag{5.31}$$

and

$$v_L R_L = v_L^0 R_L^0 + v_L^z R_L^z + v_L^{0z} R_L^{0z}, \tag{5.32}$$

with

$$R_L^0 = \left|\langle\mathcal{J}^0(\vec{q})\rangle\right|^2, \quad R_L^z = \left|\langle\mathcal{J}^z(\vec{q})\rangle\right|^2, \quad R_L^{0z} = -2\Re\left\{\langle\mathcal{J}^0(\vec{q})\rangle\langle\mathcal{J}^z(\vec{q})\rangle^*\right\}, \tag{5.33}$$

and

$$v_L^0 = \left[1 + \sqrt{1 - \frac{M_l^2}{\varepsilon'^2}}\cos\theta_l\right], \tag{5.34}$$

$$v_L^z = \left[1 + \sqrt{1 - \frac{M_l^2}{\varepsilon'^2}}\cos\theta_l - \frac{2\varepsilon\varepsilon'}{|\vec{q}|^2}\left(1 - \frac{M_l^2}{\varepsilon'^2}\right)\sin^2\theta_l\right], \tag{5.35}$$

$$v_L^{0z} = \left[\frac{\omega}{|\vec{q}|}\left(1 + \sqrt{1 - \frac{M_l^2}{\varepsilon'^2}}\cos\theta_l\right) + \frac{M_l^2}{\varepsilon'|\vec{q}|}\right]. \tag{5.36}$$

The expressions for R_T, R_{TT}, R'_T and R'_{TL} remain unaltered.

Dirac	Pauli	Scalar	Axial vector	Pseudoscalar	Tensor
γ_α	$\sigma_{\alpha\beta}q^\beta$	q_α	$\gamma_\alpha\gamma_5$	$q_\alpha\gamma_5$	$\sigma_{\alpha\beta}q^\beta\gamma_5$

Table 5.1 Lorentz invariant operators contributing to the weak nucleon current.

So far, a precise knowledge of the kinematic variables at the lepton vertex was assumed. In practice, this information is not attainable in typical neutrino scattering experiments. Indeed, in NC reactions, the scattered lepton is chargeless and remains undetected. In CC processes, on the other hand, detection of the final lepton is possible and its energy and momentum could in principle be measured. Due to limited control on the incoming neutrino energies, however, this cannot be accomplished. In order to get the QE neutrino-nucleus cross section, we integrate over the phase space of the scattered lepton ($d^2\Omega_l$) and the outgoing nucleon ($d^2\Omega_f(\theta_f,\,\phi)$). For the latter, integration over the azimuthal angle ϕ yields a factor 2π, whilst only the ϕ-independent response functions of Eq. (5.11) survive due to symmetry properties. This yields

$$\frac{d\sigma}{d\varepsilon'} = \frac{M_N M_{A-1}}{(2\pi)^3 M_A} 4\pi^2 \int \sin\theta_l d\theta_l \int \sin\theta_f d\theta_f k_f f_{rec}^{-1} \sigma_M [v_L R_L + v_T R_T + h v'_T R'_T] \ . \quad (5.37)$$

In practice, we compute the response functions for all single-particle levels in the target nucleus, and obtain $d\sigma/d\varepsilon'$ by summing over all these.

5.2.2 The nuclear current

We evaluate the nuclear current matrix elements of Eq. (5.10) under the same assumptions as those adopted for the electron-scattering results of chapters 2-4. In particular, we describe the neutrino-nucleus nucleon-knockout reaction within the impulse approximation, and employ a relativistic independent-particle model for the wave functions of the target and the residual nuclei. Accordingly, the transition matrix elements can be cast in the form of Eq. (3.1). For an elaborate discussion on the bound-state and scattering wave functions entering this equation, the reader is referred to sections 2.3 and 2.4. The derivations outlined there are independent of the leptonic probe, and a reiteration would be superfluous.

Here, we mainly concentrate on the relativistic one-body current operator modeling the coupling between the virtual Z^0 or $W^\pm$ boson and a bound nucleon.

Lorentz invariance results in six operators involved in the weak nucleon current. These are summarized in Table 5.1. Further, the weak nucleon current is supposed to be Hermitian and invariant under time reversal. These conditions nullify the contributions from the tensor and scalar terms. Moreover, no experiment carried out so far calls this assumption into question. Accordingly, the one-body vertex function J^α can be expressed as

$$\begin{aligned} J^\alpha_{cc2} &= \tilde{F}_1(Q^2)\gamma^\alpha + i\frac{\kappa}{2M_N}\tilde{F}_2(Q^2)\sigma^{\alpha\beta}q_\beta \\ &\quad + G_A(Q^2)\gamma^\alpha\gamma_5 + \frac{1}{2M_N}G_P(Q^2)q^\alpha\gamma_5 \,, \end{aligned} \tag{5.38}$$

where $\tilde{F}_1$ is the weak Dirac, $\tilde{F}_2$ the weak Pauli, G_A the axial and G_P the pseudoscalar form factor, respectively. For a free nucleon, the Gordon identity allows several equivalent forms for the vector part of Eq. (5.38). Here, we employ the expressions that reflect the ones of Eq. (2.39), yielding

$$\begin{aligned} J^\alpha_{cc1} &= \tilde{G}_M(Q^2)\gamma^\alpha - \frac{\kappa}{2M_N}\tilde{F}_2(Q^2)(K_i^\alpha + K_f^\alpha) \\ &\quad + G_A(Q^2)\gamma^\alpha\gamma_5 + \frac{1}{2M_N}G_P(Q^2)q^\alpha\gamma_5 \,, \end{aligned} \tag{5.39a}$$

$$\begin{aligned} J^\alpha_{cc3} &= \frac{1}{2M_N}\tilde{F}_1(Q^2)(K_i^\alpha + K_f^\alpha) + i\frac{1}{2M_N}\tilde{G}_M(Q^2)\sigma^{\alpha\beta}q_\beta \\ &\quad + G_A(Q^2)\gamma^\alpha\gamma_5 + \frac{1}{2M_N}G_P(Q^2)q^\alpha\gamma_5 \,. \end{aligned} \tag{5.39b}$$

The relation between the weak Sachs electric and magnetic form factors $\tilde{G}_E$ and $\tilde{G}_M$ and the weak Dirac and Pauli form factors $\tilde{F}_1$ and $\tilde{F}_2$ is established by Eq. (2.41). As discussed in Sec. 2.2, ambiguities arise when the nucleon is embedded in a nuclear medium, and the above expressions are no longer guaranteed to produce the same results. Full current conservation is, in contrast to the electromagnetic case, not a prerequisite for the weak interaction.

Further on, we will show that there exists a direct relationship between the weak vector form factors and the electromagnetic ones. To that purpose, we review a number of basic concepts from the electroweak interaction within the context of the standard model.

The electroweak interaction

The electroweak interaction is part of the standard model and is based on a local $SU(2)_L \times U(1)_W$ symmetry. The index L indicates that weak interactions couple only to left-handed components of the particle fields and W stands for weak. In the standard model, the electromagnetic (J^α_{EM}), neutral (J^α_{NC}) and charged (J^α_{CC}) weak currents can be expressed in terms of quarks as

$$J^\alpha_{EM} = \overline{q}Q\gamma^\alpha q = \frac{2}{3}\overline{u}\gamma^\alpha u - \frac{1}{3}\overline{d}\gamma^\alpha d - \frac{1}{3}\overline{s}\gamma^\alpha s \ , \tag{5.40}$$

$$\begin{aligned} J^\alpha_{NC} &= \overline{u}\gamma^\alpha \left[\frac{1}{2} - \frac{2}{3}2\sin^2\theta_W - \frac{1}{2}\gamma_5\right] u - \overline{d}\gamma^\alpha \left[\frac{1}{2} - \frac{1}{3}2\sin^2\theta_W - \frac{1}{2}\gamma_5\right] d \\ &\quad -\overline{s}\gamma^\alpha \left[\frac{1}{2} - \frac{1}{3}2\sin^2\theta_W - \frac{1}{2}\gamma_5\right] s \ , \end{aligned} \tag{5.41}$$

$$J^\alpha_{CC} = \begin{cases} \overline{u}\gamma^\alpha(1-\gamma_5)d & \text{if } W^+ \ , \\ \overline{d}\gamma^\alpha(1-\gamma_5)u & \text{if } W^- \ . \end{cases} \tag{5.42}$$

In the above equations, θ_W corresponds to the Weinberg angle with standard value $\sin^2\theta_W = 0.2224$. Further, q refers to the fundamental representation of $SU(3)$

$$q \equiv \begin{pmatrix} u \\ d \\ s \end{pmatrix} \ , \qquad \begin{aligned} T_z &= +1/2 \\ T_z &= -1/2 \ , \\ T_z &= 0 \end{aligned} \qquad \begin{aligned} Y &= +1/3 \\ Y &= -1/3 \ . \\ Y &= -2/3 \end{aligned} \tag{5.43}$$

and $Q = T_z + \frac{Y}{2}$ the charge, with T_z the third component of isospin and Y the hypercharge. The above expressions are restricted to the low-energy section of QCD and include an implicit sum over color. For the charged weak current, we have neglected the parts that appear due to the Cabbibo mixing, as they are suppressed by a factor $\sin\theta_c$.

Apart from its local $SU(3)$-color gauge symmetry, QCD has global unitary symmetries. Indeed, assuming isospin symmetry (m_u=m_d=m_s), the QCD Lagrangian has a global $SU(3)$-flavor symmetry and is invariant under

$$q \longrightarrow \exp\left(i\theta^i \frac{\lambda_i}{2}\right) q \ , \tag{5.44}$$

with λ_i the Gell-Mann matrices and θ_i infinitesimal rotation angles ($i = 1, ..., 8$). The Gell-Mann matrices are listed in Appendix A. The corresponding conserved Noether currents are

$$V^\alpha_i = \overline{q}\gamma^\alpha \frac{\lambda_i}{2} q \ , \qquad i = 1, ..., 8 \ . \tag{5.45}$$

In the limit of massless quarks, QCD is chirally symmetric, making the Lagrangian invariant under

$$q_L \longrightarrow \exp\left(i\theta_L^i \frac{\lambda_i}{2}\right) q_L \qquad q_R \longrightarrow \exp\left(i\theta_R^i \frac{\lambda_i}{2}\right) q_R \ , \tag{5.46}$$

where q_L and q_R are the left and right-handed quark fields, defined as

$$q_L = \frac{1}{2}(1-\gamma_5)q \qquad q_R = \frac{1}{2}(1+\gamma_5)q \ . \tag{5.47}$$

The conserved Noether currents read

$$V_{i,L}^{\alpha} = \overline{q}_L \gamma^{\alpha} \frac{\lambda_i}{2} q_L \qquad V_{i,R}^{\alpha} = \overline{q}_R \gamma^{\alpha} \frac{\lambda_i}{2} q_R \ . \tag{5.48}$$

The sum of $V_{i,L}$ and $V_{i,R}$ gives rise to the vector currents of Eq. (5.45), whereas their difference defines the axial currents

$$A_i^{\alpha} = V_{i,R}^{\alpha} - V_{i,L}^{\alpha} = \overline{q}\gamma^{\alpha}\gamma_5 \frac{\lambda_i}{2} q \ , \qquad i = 1, ..., 8 \ . \tag{5.49}$$

In the Gell-Mann representation, λ_3 and λ_8 are the only diagonal matrices. Consequently they do not change flavor. Hence, one is allowed to rewrite the electromagnetic current as

$$J_{EM}^{\alpha} = V_3^{\alpha} + V_S^{\alpha} \ , \tag{5.50}$$

with V_3^{α} the isovector(isospin) current and V_S^{α} the isoscalar (hypercharge) current given by

$$V_S^{\alpha} = \overline{q}\gamma^{\alpha} \frac{\lambda_8}{2\sqrt{3}} q \ . \tag{5.51}$$

The neutral weak current can then be written as a sum of a vector and an axial part

$$J_{NC}^{\alpha} = V_{NC}^{\alpha} + A_{NC}^{\alpha} \ , \tag{5.52}$$

with

$$V_{NC}^{\alpha} = \left(1 - 2\sin^2\theta_W\right) V_3^{\alpha} - 2\sin^2\theta_W V_S^{\alpha} - \frac{1}{2}\overline{s}\gamma^{\alpha} s \ , \tag{5.53}$$

$$A_{NC}^{\alpha} = -A_3^{\alpha} + \frac{1}{2}\overline{s}\gamma^{\alpha}\gamma_5 s \ . \tag{5.54}$$

Finally, the charged weak current takes on the form

$$J^{\alpha}_{CC} = V^{\alpha}_{CC} + A^{\alpha}_{CC} \,, \tag{5.55}$$

with

$$V^{\alpha}_{CC} = \overline{q}\gamma^{\alpha}\frac{\lambda_{\pm}}{2}q \,, \tag{5.56}$$

$$A^{\alpha}_{CC} = -\overline{q}\gamma^{\alpha}\gamma_5\frac{\lambda_{\pm}}{2}q \,. \tag{5.57}$$

Accordingly, the electromagnetic current and the weak vector currents are related through the conserved flavor current. By analogy, we can conclude that in the limit of massless quarks the axial parts of the neutral and charged weak currents are components of the same conserved $SU(3)$ axial current.

Electroweak vector form factors

At the energy scales considered in this work, quarks are not the appropriate degrees of freedom, but hadrons are. Accordingly, the matrix elements of the currents are computed between initial and final nucleon states. As outlined in Sec. 2.2, one accounts for the internal structure of protons and neutrons by introducing form factors.

The electromagnetic one-body vertex function in the $CC2$ parametrization of Eq. (2.39b) reads

$$J^{\alpha,p}_{EM} = F^{p}_{1}\gamma^{\alpha} + \frac{i}{2M_N}\sigma^{\alpha\beta}q_{\beta}F^{p}_{2} \,, \tag{5.58}$$

$$J^{\alpha,n}_{EM} = F^{n}_{1}\gamma^{\alpha} + \frac{i}{2M_N}\sigma^{\alpha\beta}q_{\beta}F^{n}_{2} \,, \tag{5.59}$$

where $F_1^{p,n}$ and $F_2^{p,n}$ are the electromagnetic Dirac and Pauli form factors of the nucleon. In the previous section we mentioned expression for the electroweak interaction on individual quarks. The extension of current algebra from quarks to composite systems, however, can be easily made. Indeed, so far we only assumed isospin symmetry of the strong interaction. Accordingly, the obtained relations of Eqs. (5.50),(5.52) and (5.55) can be expected to be independent of the hadronic structure if isospin is a good symmetry of the particular hadronic system. Thus,

the electromagnetic current can be split into an isovector and isoscalar part, which yield the following current operators in isospin space

$$V_3^\alpha = \left(F_1^V\gamma^\alpha + \frac{i}{2M_N}\sigma^{\alpha\beta}q_\beta F_2^V\right)\frac{t_3}{2}\,, \tag{5.60}$$

$$V_S^\alpha = \left(F_1^S\gamma^\alpha + \frac{i}{2M_N}\sigma^{\alpha\beta}q_\beta F_2^S\right)\frac{1}{2}\,. \tag{5.61}$$

The convention for the isospin operators is given in Appendix A. These involve

$$t_3|p\rangle = +1|p\rangle \qquad \text{and} \qquad t_3|n\rangle = -1|n\rangle, \tag{5.62}$$

and hence we can write

$$F_{1,2}^V = F_{1,2}^p - F_{1,2}^n \qquad \text{and} \qquad F_{1,2}^S = F_{1,2}^p + F_{1,2}^n\,. \tag{5.63}$$

Eq. (5.53) reveals that the vector part of the neutral weak current is a linear combination of V_3^α and V_S^α. Accordingly, we can write the neutral weak vector form factors as

$$\tilde{F}_{1,2} = \left(\frac{1}{2} - \sin^2\theta_W\right)(F_{1,2}^p - F_{1,2}^n)\tau_3 - \sin^2\theta_W(F_{1,2}^p + F_{1,2}^n) - \frac{1}{2}F_{1,2}^s\,. \tag{5.64}$$

Hereby, τ_3 equals $+1(-1)$ for protons (neutrons). $F_{1,2}^s$ quantifies the effect of strange quarks.

Now we focus on the charged weak current. To that purpose, we assume that the matrix elements of the hadronic currents V_{CC}^α and V_3^α are related through isospin rotation. Since the electromagnetic current is conserved, this assumption implies that the weak vector current is conserved. This presumption was postulated by Feynman and Gell-Mann as the so-called conserved vector current hypothesis (CVC). On the quark level this hypothesis holds exactly as a consequence of QCD. The matrix elements of V_{CC}^α read

$$V_{CC}^\alpha = \left(F_1^v\gamma^\alpha + \frac{i}{2M_N}\sigma^{\alpha\beta}q_\beta F_2^v\right)\frac{t_\pm}{2}\,. \tag{5.65}$$

CVC now implies that the currents of Eq. (5.60) and Eq. (5.65) are components of the same isospin multiplet of conserved currents. This yields

$$F_{1,2}^v \equiv F_{1,2}^V\,. \tag{5.66}$$

Accordingly, we can write the charged weak vector form factors as

$$\tilde{F}_{1,2} = \begin{cases} \left(F^p_{1,2} - F^n_{1,2}\right) & \text{if } W^+ \ , \\ \left(F^n_{1,2} - F^p_{1,2}\right) & \text{if } W^- \ . \end{cases} \tag{5.67}$$

Axial form factors

Having related the weak vector form factors to the electromagnetic ones, we now focus on the axial parts A^α_{NC} and A^α_{CC} that appear in the neutral and charged weak interactions.

For the neutral weak interaction, we have shown that the axial current consists of an isovector and a strangeness part

$$A^\alpha_{NC} = -A^\alpha_3 + \frac{1}{2}\overline{s}\gamma^\alpha\gamma_5 s \ . \tag{5.68}$$

Therefore, we obtain

$$A^\alpha_{NC} = \left(F_A\gamma^\alpha\gamma_5 + \frac{1}{2M_N}G_P q^\alpha\gamma_5\right)\frac{-t_3}{2} \tag{5.69}$$

$$+ \ \left(F^s_A\gamma^\alpha\gamma_5\right)\frac{1}{2} \ . \tag{5.70}$$

In literature, the Q^2 dependence of the axial form factors F_A and F^s_A is usually described in terms of a dipole parametrization

$$F_A(Q^2) = g_A G(Q^2) \ , \qquad F^s_A(Q^2) = g^s_A G(Q^2) \ , \tag{5.71}$$

where g_A=1.262, $G(Q^2) = (1 + Q^2/M^2)^{-2}$ with $M = 1.032$ GeV. The axial strange-quark contribution is quantified by g^s_A. Accordingly, for neutral weak interactions we can parametrize the axial form factor that enters Eq. (5.38) as

$$G_A(Q^2) = -\frac{(\tau_3 g_A - g^s_A)}{2}G(Q^2) \ . \tag{5.72}$$

For the time being, we will neglect possible contributions from the sea-quarks ($g^s_A = F^s_1 = F^s_2 = 0$).

For the charged weak interaction, we again assume that the matrix elements of A^α_{CC} and A^α_3 are the same. Therefore, we obtain

$$A^\alpha_{CC} = \left(F_A\gamma^\alpha\gamma_5 + \frac{1}{2M_N}G_P q^\alpha\gamma_5\right)\frac{-t_\pm}{2} \ . \tag{5.73}$$

Accordingly, for charged weak interactions the axial form factor can be parametrized as

$$G_A(Q^2) = \begin{cases} g_A G(Q^2) & \text{if } W^+ \ , \\ -g_A G(Q^2) & \text{if } W^- \ . \end{cases} \tag{5.74}$$

It can be shown that the divergence of the axial current is proportional to the square of the pion mass m_π and vanishes in the chiral limit $m_\pi \to 0$. This is known as the partially conserved axial current hypothesis (PCAC). The Goldberger-Treiman relation allows then to write the pseudoscalar form factor as

$$G_P(Q^2) = \frac{2M_N}{Q^2 + m_\pi^2} G_A(Q^2). \tag{5.75}$$

The pseudoscalar form factor, however, appears with a factor proportional to the mass of the scattered lepton, and hence, vanishes for NC reactions.

The direct relationship between the electromagnetic and the weak vector form factors implies that the Q^2 dependence of the weak vector form factors is susceptible to the uncertainties which arise due to possible higher-order photon-exchange corrections. In Fig. 5.2, the upper panel displays the neutral current proton form factors of Eqs. (5.64) and (5.72). The lower panel shows the charged current "W^+" form factors of Eqs. (5.67) and (5.73). The predictions obtained with the dipole parametrization for the underlying electromagnetic form factors are compared to the ones employing the BBA-2003 parametrization of Refs. [54, 55]. The BBA-2003 parametrization accounts for improved fits implementing new $p(\vec{e}, e')p$ data and still uses the dipole form of Eq. (5.71) for the axial form factor, but predicts a slightly reduced axial mass of M=1.00 GeV. As can be inferred, the differences between both parametrizations are minor for $Q^2 \leq 3$ (GeV/c)^2.

5.3 Cross-section results

The RDWIA and RMSGA models were initially developed for the description of exclusive $A(e, e'p)$ processes. It is clear that inclusive neutrino scattering cross sections include contributions which fall beyond the scope of the RDWIA and RMSGA models. Both the RDWIA and RMSGA are confined to those processes where the scattering of a neutrino from a nucleus causes a single nucleon to escape, thereby

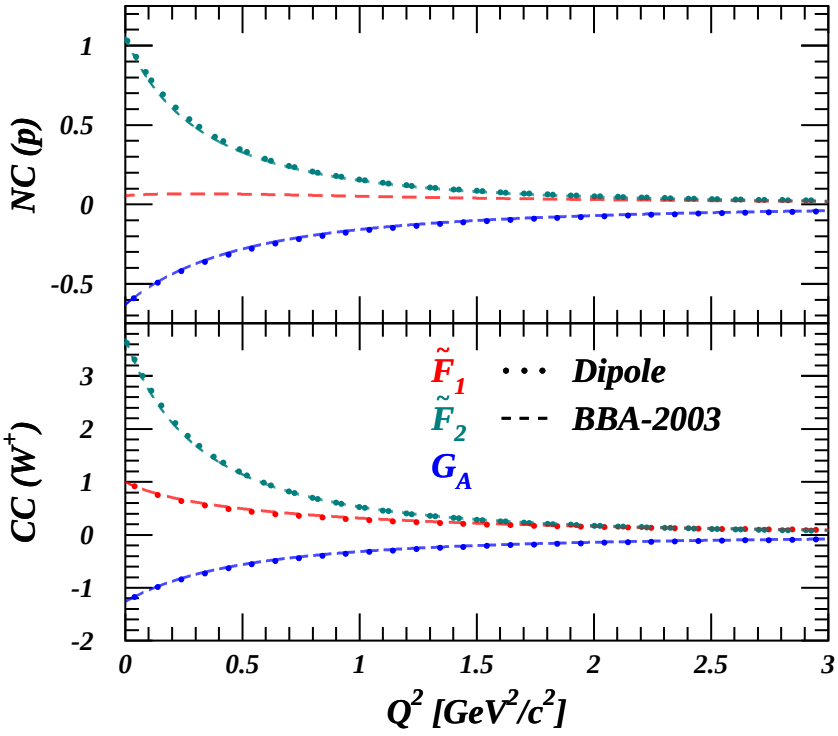

Figure 5.2 The weak vector form factors and the axial form factor in the dipole (dotted) and BBA-2003 (dashed) parametrization. The upper panel corresponds to neutral current interactions on protons, while the lower one displays the charged current results for W^+.

exciting the residual nucleus to a state with missing energies below 80 MeV and a predominant single-hole nuclear structure with respect to the ground state of the target nucleus. We refer to such processes as "elastic" ones and wish to stress that they include proton and neutron knockout from the deepest lying $1s$ up to the Fermi level. Inelastic single-nucleon knockout channels populating more complex states in the residual A-1 nucleus are excluded from our calculations. So are multi-nucleon knockout channels and channels involving a pion. In that sense, the RDWIA and RMSGA predictions for the inclusive neutrino-nucleus cross sections

should be interpreted as a lower limit of the single-nucleon knockout contribution.

We present results for QE neutrino scattering from ^{12}C and ^{56}Fe, which are nuclei well suited for neutrino detection. The calculations span incident neutrino energies from 150 MeV up to 5 GeV. From about 200 MeV to 1 GeV, the quasi-elastic nucleon knockout is expected to be the dominant contribution to the neutrino-nucleus cross section. At higher energies, the relative contribution of the inelastic channels, mainly those involving an intermediate delta resonance and pion production, is expected to become increasingly dominant in the inclusive process [186, 187]. Ref. [186] indicates that in the neutrino energy range from 0.7 to 5 GeV reaction channels involving a pion contribute for 15% to the total cross section.

Again, in order to make the comparison between the RDWIA and RMSGA calculations as meaningful as possible, all the ingredients in the calculations not related to FSI, as those concerning the implementation of relativistic dynamics and nuclear recoil effects, are kept identical. In particular, both pictures adopt the W1 parametrization [62] for the different field strengths in determining the bound-state wave functions and employ the $CC2$ form for the current operator. The integrations in Eq. (5.37) require a tremendous numerical effort in the RMSGA framework. Accordingly, we employ the thickness averaging procedure of Eq. (2.93) for the numerical evaluation of the Glauber phase.

It speaks for itself that before embarking on the study of effects like FSI and the strangeness content of the nucleon, it is absolutely essential to possess reliable baseline RPWIA cross sections with a numerical accuracy of a few percent. To this purpose, before turning to the study of the role of FSI mechanisms, we first investigate the RPWIA limit of the RMSGA and RDWIA models. These predictions will be compared and confronted with other RPWIA results which made their way to literature recently [171, 173].

5.3.1 Limit of vanishing FSI

Fig. 5.3 shows the results of various RPWIA calculations for $^{12}\mathrm{C}(\nu,\nu')$ at 150, 500 and 1000 MeV. We observe that the plane-wave limits of our RMSGA and RDWIA formalisms are in excellent agreement. The remaining differences, smaller than 2-3$\%$, can be attributed to the distinctive numerical techniques. This comparison lends us confidence about the consistency of the two types of calculations and the

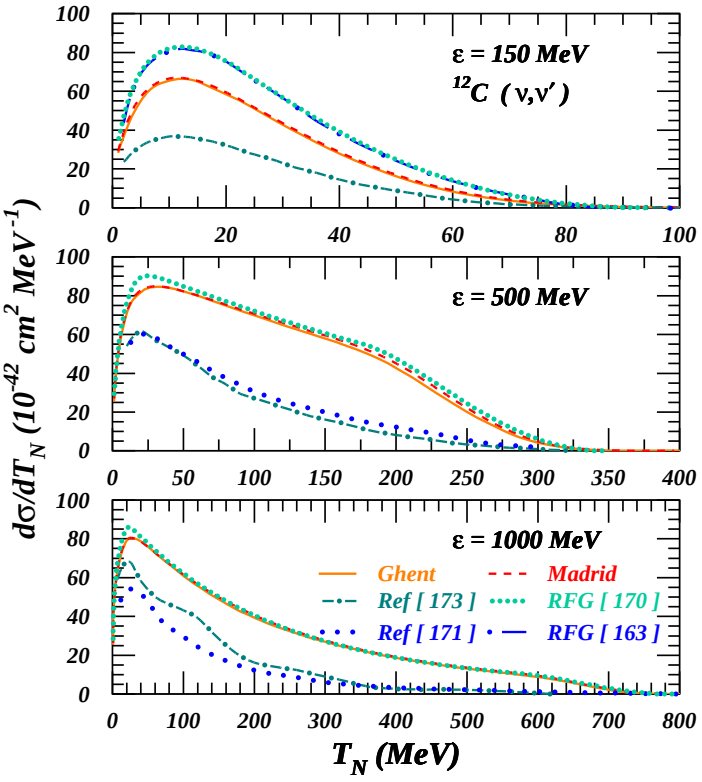

Figure 5.3 Neutral current $^{12}\mathrm{C}(\nu,\nu')$ cross sections as a function of the outgoing nucleon kinetic energy T_N at different incoming neutrino energies. The solid (dashed) lines represent the RPWIA results of the Ghent (Madrid) group. The short-dot-dashed lines show the RPWIA results of Ref. [173], and the long-dotted lines those of Ref. [171]. The short-dotted (long-dot-dashed) line shows the predictions of the RFG model of Ref. [170] (Ref. [163]) with a binding-energy correction of 27 MeV.

reliability of the adopted numerical techniques.

The fact that our models provide almost identical RPWIA results may seem trivial. As can be appreciated via Fig. 5.3, however, our RPWIA predictions disagree with the ones of Refs. [171] and [173]. Although the RPWIA calculations of Refs. [171] and [173] are mutually consistent at $\varepsilon = 500$ MeV, this is no longer the case at $\varepsilon = 1$ GeV. In the search for the origin of the discrepancies between

our and other RPWIA calculations, differences in the nuclear current can be ruled out. The current operator of Eq. (5.38) used along this work is formally identical to the one mentioned in Refs. [171] and [173], and the same holds for the form-factor parametrization. Only the bound-state wave functions used in Refs. [171] and [173] differ from ours. We have performed cross-section calculations with various parametrizations for the bound-state wave functions, and found almost negligible differences.

The role of the various terms $\tilde{F}_1$, $\tilde{F}_2$ and G_A in Eq. (5.38) in the NC differential cross section was investigated in Ref. [173]. The results were illustrated for proton knockout from the $1p_{3/2}$ orbital of ^{12}C, at incident neutrino energies of 150, 500 and 1000 MeV. In Fig. 5.4, we analyse the contribution of the $\tilde{F}_1$, $\tilde{F}_2$ and G_A form factors in our cross sections under the same circumstances. As can be inferred, the calculations performed by nullifying $\tilde{F}_1$ (long-dot-dashed lines) almost reproduce the full cross sections (solid lines). This illustrates, in agreement with the outcomes of Ref. [173] and Fig. 5.2, that the contribution of the Dirac form factor is very small. Accordingly, one can approximate the full cross section as a sum of three terms: one proportional to $(G_A)^2$, a second to $(\tilde{F}_2)^2$, and a third to the interference of G_A and $\tilde{F}_2$ contributions. The term proportional to $(G_A)^2$ (dashed lines) is very similar to the corresponding one in Fig. 11 of Ref. [173]. The same holds for the cross sections obtained by nullifying G_A (short-dot-dashed lines). Accordingly, the differences between our results and the ones of Ref. [173] can be mainly attributed to the $G_A\tilde{F}_2$ interference term. Furthermore, switching the sign of the $G_A\tilde{F}_2$ term in our calculations yields cross sections that closely follow the ones of Ref. [173]. At 500 and 1000 MeV the differential cross sections of Ref. [173] display some oscillations as a function of T_N. As can be appreciated from Figs. 5.3 and 5.4, we find no indications for these oscillations. Recently, the authors of Ref. [173] have extended their work to calculate CC neutrino cross sections [188]. We remark that for this type of neutrino reactions the magnitude of the cross sections is in agreement with the RPWIA limit of the models presented here. Moreover, the authors of Ref. [171] have recently revised their calculations [189], and eliminated some inconsistencies. The new results are consistent with our RPWIA calculations.

It is well known that binding-energy effects tend to vanish with increasing energies. Accordingly, a description of the ν-nucleus scattering process in terms of

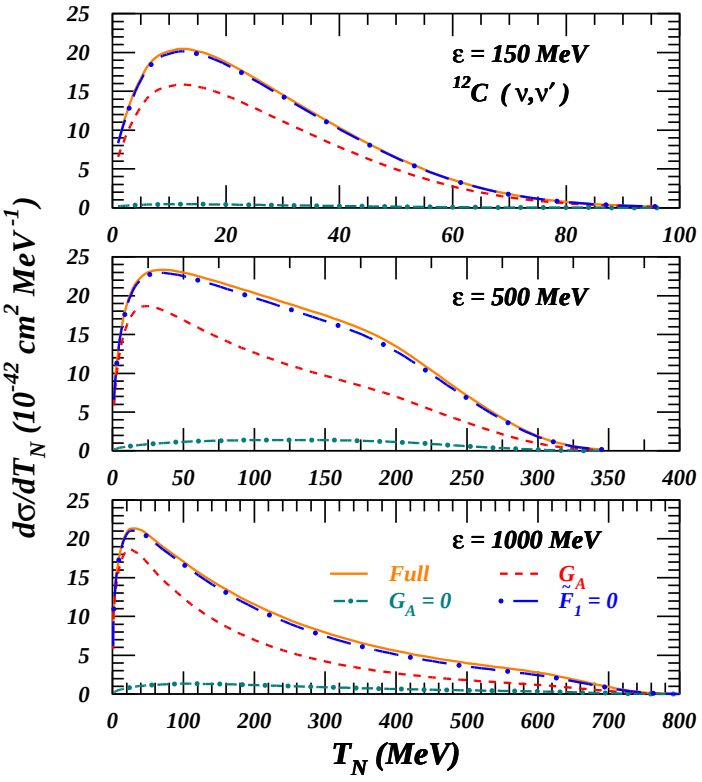

Figure 5.4 Effect of the different form factors on the neutral current $^{12}\mathrm{C}(\nu,\nu')$ cross sections as a function of T_N at different incoming neutrino energies. The results correspond to proton knockout from the $1p_{3/2}$ orbital of ^{12}C. The solid lines represent the full RPWIA results. The long-dot-dashed (short-dot-dashed) lines show the results with $\tilde{F}_1 = 0$ ($G_A = 0$). The dashed lines show the cross section when only G_A is considered.

a RFG model is expected to approach the RPWIA predictions at high incoming neutrino energies. This is observed in Fig. 5.3, when comparing the RFG results of Refs. [163, 168, 170] with our RPWIA predictions. At $\varepsilon = 150$ MeV, our RPWIA cross sections are approximately 15% smaller than the RFG ones, that include a non-zero binding-energy correction of 27 MeV. The RPWIA prediction of Ref. [173] is about a factor of two smaller. The RFG results from Refs. [168, 170]

closely follows our RPWIA results at 500 MeV, the agreement at 1 GeV being remarkably good. The observed similarity between the independent RFG predictions of Refs. [163, 168, 170] and our RPWIA results lends us additional confidence that the RPWIA results presented here can serve as benchmark calculations.

5.3.2 The effect of FSI: RMSGA and RDWIA approaches

Let us now turn our attention to the effect of FSI. NC ν-nucleus cross sections obtained within RDWIA and RMSGA are displayed in Fig. 5.5. The calculations correspond to ^{12}C and ^{56}Fe targets, and incoming energies of 500, 1000, and 5000 MeV. Focusing on the results of the RDWIA model, the inclusion of the complex optical potential reduces the RPWIA results by nearly $40-50\%$ for ^{12}C. As expected, the global effect of FSI increases with growing atomic number, and reductions of over 60% are obtained for ^{56}Fe. The presence of the imaginary term in the optical potential is likely to lead to an underestimation of the single-nucleon knockout contribution to the inclusive cross section. Indeed, in inclusive measurements all possible final channels are included, whilst the RDWIA and RMSGA calculations are confined to "elastic" single-nucleon knockout.

As previously stated, Glauber-inspired models have been esteemed to provide reliable results at high energies, due to the underlying approximations. In line with the results of the former chapters, however, the RMSGA predictions for integrated quantities (as the ones involved in neutrino experiments) compare very well with the RDWIA ones down to remarkably low ejectile kinetic energies of about 200 MeV.

For the sake of completeness, in Fig. 5.6 we show our predictions for CC ν-nucleus cross sections. The effects of FSI are of the same order as for NC, and similar conclusions can be drawn for the mutual RDWIA-RMSGA behaviour.

5.3.3 Using $A(e,e'p)$ transparencies to estimate FSI

As outlined in chapter 3, the nuclear transparency is a quantity routinely used to estimate the overall effect of FSI in nucleon-emission processes. Intuitively, it provides a measure for the probability that a nucleon of a certain energy - above the particle-emission threshold - can escape from the nucleus without being subject to any further interaction. From this 'definition', one can expect that the nuclear trans-

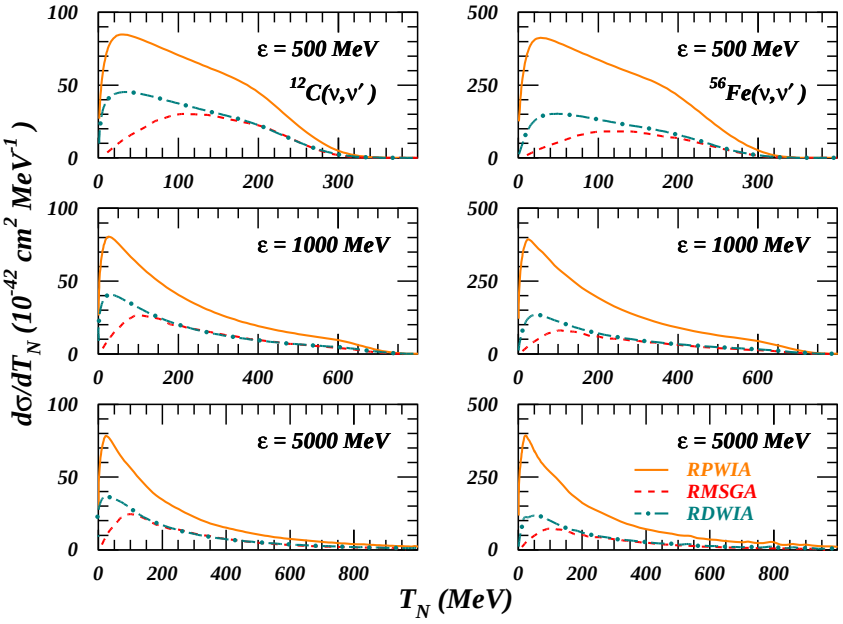

Figure 5.5 Neutral current $^{12}\mathrm{C}(\nu,\nu')$ (left panels) and $^{56}\mathrm{Fe}(\nu,\nu')$ (right panels) cross sections as a function of T_N at different incoming neutrino energies. The solid lines represent the RPWIA predictions of the Madrid group, in agreement with those of the Ghent one. The dashed (dot-dashed) lines implement the effect of FSI within the RMSGA (RDWIA) framework.

parency is identical for neutrino and electron induced nucleon knockout. Once the nucleon is traversing the nuclear medium, only its energy is expected to determine the way it propagates. In addition, neutrinos and electrons can be expected to probe equal amounts of bulk and surface parts of the target nucleus.

In Fig. 5.7, the transparencies predicted by the RMSGA and the RDWIA models are displayed as a function of Q^2 for ^{12}C and ^{56}Fe, together with the world $A(e,e'p)$-data. Solid (dot-dashed) lines show the $A(e,e'p)$ results within RMSGA (RDWIA). For an elaborated discussion on the calculation and the extraction of the nuclear transparency in $A(e,e'p)$ reactions in the QE regime, the reader is referred to chapter 3. The dashed (RMSGA) and dotted (RDWIA) curves correspond to the

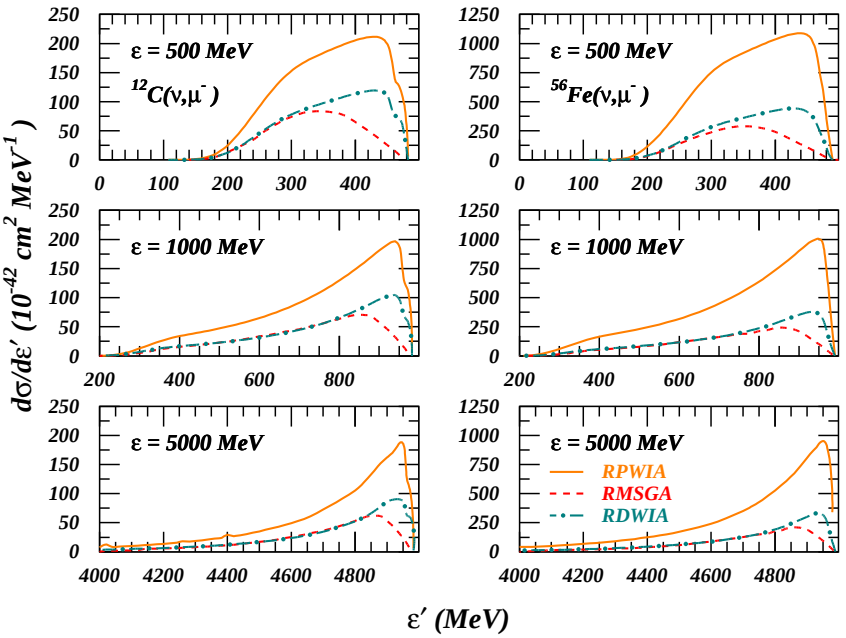

Figure 5.6 Charged current $^{12}\mathrm{C}(\nu_\mu, \mu^-)$ (left panels) and $^{56}\mathrm{Fe}(\nu_\mu, \mu^-)$ (right panels) cross sections as a function of the outgoing lepton energy ε' at different incoming energies. The labeling is the same as in Fig. 5.5.

computed $A(\nu, \nu' p)$ transparencies, obtained using the same procedure as for electron scattering. This procedure includes the computation of RDWIA and RPWIA cross sections at $x \approx 1$, averaged over the same phase space used in Eq. (3.4). As can be seen, within each model the neutrino transparencies agree quite well with their electron counterparts. This result clearly illustrates the fact that *in our models* the average attenuation effect of the nuclear medium on the emerging nucleon is rather independent of the nature of the leptonic probe.

Adopting the idea that the nuclear transparency for electrons equals the one for neutrinos, the information obtained about nucleon propagation via $A(e, e' p)$ can be used to predict the effects of FSI mechanisms in inclusive QE ν-nucleus cross sections. As the transparency is essentially the ratio of cross sections including FSI

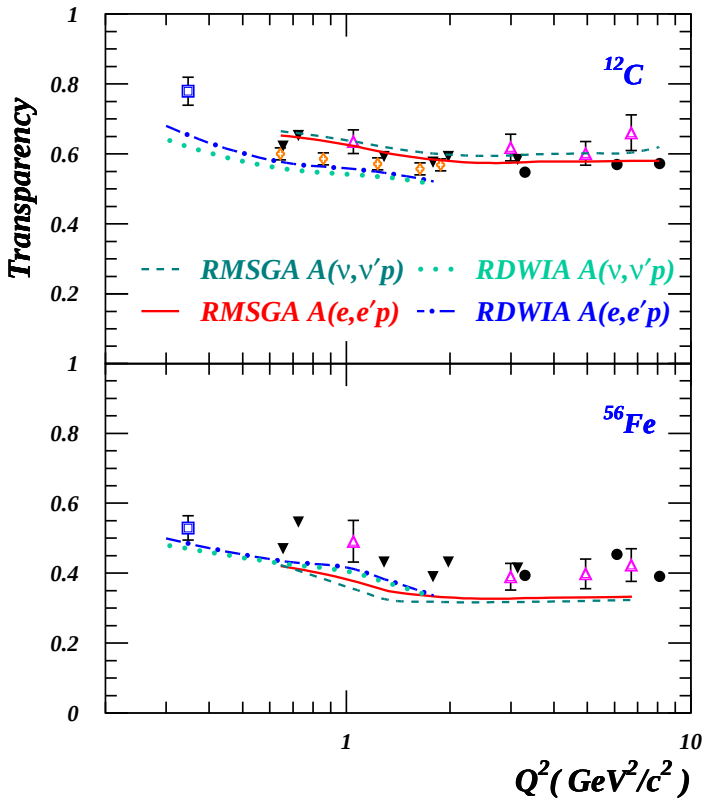

Figure 5.7 Nuclear transparencies versus Q^2 for different nuclei in quasi-elastic kinematics. The solid (dot-dashed) lines shows the results of a RMSGA (RDWIA) $A(e,e'p)$ calculation [190]. The dashed (dotted) lines represent the results for $A(\nu,\nu'p)$ within RMSGA (RDWIA). Data are from Refs. [93] (open squares), [94, 95] (open triangles), [96](solid circles), [7, 97](solid triangles) and [98](open diamonds).

to the ones in the plane-wave limit, this will be done by multiplying the RPWIA results for neutrino-nucleus cross sections with the measured transparency factors extracted from $A(e,e'p)$. In this scenario, the benchmark RPWIA neutrino-nucleus cross sections are crucial. It is important to realize that we use transparency factors that are confined to $x \approx 1$, while the computation of the inclusive neutrino-nucleus cross section include the full phase-space.

In Fig. 5.8, the dashed and dot-dashed lines represent the inclusive CC ν-nucleus cross section within RMSGA and RDWIA, respectively. The solid curve displays

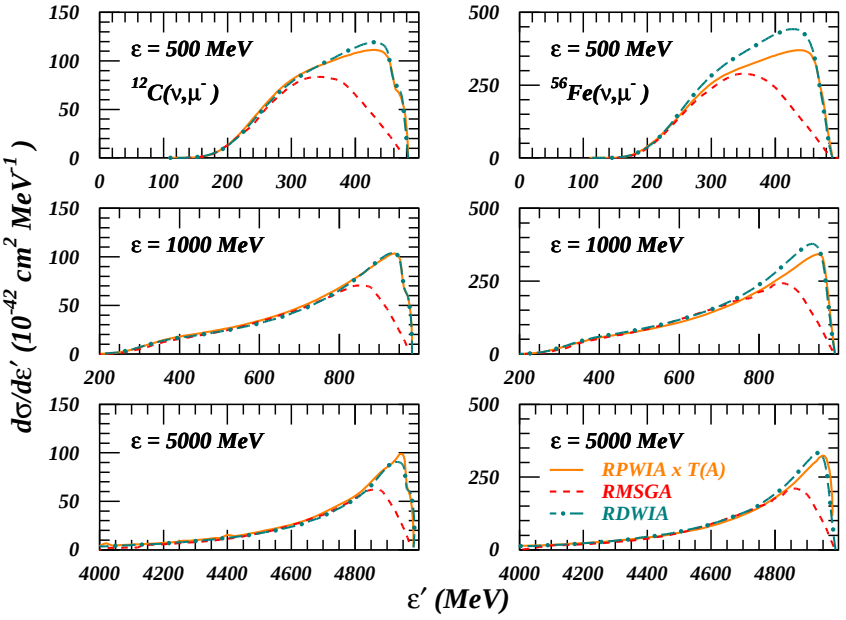

Figure 5.8 Charged current ^{12}C(ν_μ, μ^-) (left panels) and ^{56}Fe(ν_μ, μ^-) (right panels) cross sections as a function of ε' at different incoming energies. The dashed (dot-dashed) lines represent the RMSGA (RDWIA) prediction. The solid lines show the RPWIA results, scaled with a transparency factor $T(^{12}C) \approx 0.52$ and $T(^{56}Fe) \approx 0.34$.

our corresponding RPWIA calculation, scaled with a constant factor taken as a representative value for the experimental $A(e, e'p)$ transparency for the nucleus. For ^{12}C (^{56}Fe) we take $T \approx 0.52$ (≈ 0.34). In extracting these values, we have corrected the measured transparencies from Fig. 5.7 with the factor $c(A)$, appearing in the denominator of Eq. (3.2). A very good agreement is observed between the rescaled RPWIA and the full RDWIA/RMSGA curves in the case of ^{12}C. This finding supports the idea that a simple scaling of the RPWIA results with a transparency factor obtained from electron scattering data allows one to reliably estimate the FSI effects for the quasi-elastic contribution to the inclusive neutrino cross section. For ^{56}Fe the agreement is less satisfactory, reflecting the fact that our models slightly underestimate the ^{56}Fe transparency data.

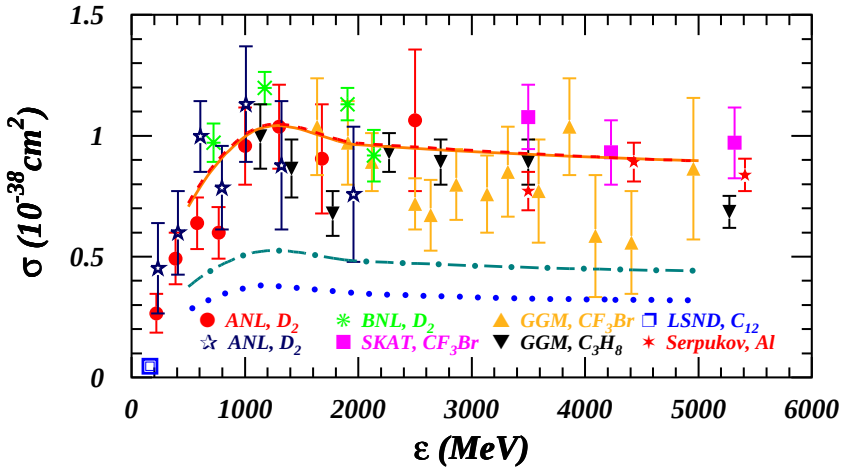

Figure 5.9 Total CC (ν_μ, μ^-) neutrino cross sections as a function of the incoming neutrino energy. The solid (dashed) line shows the RPWIA calculations on ^{12}C (^{56}Fe). The dot-dashed (long-dotted) curves implement the effect of FSI on ^{12}C (^{56}Fe) within RDWIA. All results are scaled with the number of neutrons in the target. Data points are from Refs. [191, 192, 193, 194, 195, 196, 197, 198].

Finally, Fig. 5.9 displays the total cross section $\sigma = \int d\varepsilon' (d\sigma/d\varepsilon')$ for $^{12}\mathrm{C}(\nu_\mu, \mu^-)$ and $^{56}\mathrm{Fe}(\nu_\mu, \mu^-)$ reactions, scaled with the number of neutrons in the target. Results are shown within RPWIA and RDWIA using a complex optical potential. The figure clearly shows that the difference between RPWIA and RDWIA cross sections is approximately given by the experimental transparency factor extracted from $A(e, e'p)$ at QE kinematics. Furthermore, other important features can be extracted from this figure. First, the RPWIA cross sections scale with the target mass-number. In this way, when RPWIA cross sections are required for a heavy nucleus, a very good approximation consists in multiplying this cross section per nucleon by its mass number. Second, the cross sections do not appreciably change from neutrino energies above 2 GeV, i.e. the cross sections saturate at high incoming neutrino energies.

To conclude, we compare our relativistic calculations with data from various experiments. The RPWIA calculations give a fair account of the neutrino-energy and magnitude of the data. The RPWIA is confined to single-nucleon knockout thereby not including FSI. The RDWIA calculations, on the other hand, including FSI effects via the introduction of an optical potential, considerably underestimate the data. The results contained in Fig. 5.9 indicate that at least 50% of the measured (ν_μ, μ^-) strength can be attributed to single-step ("elastic") nucleon knockout to missing energies below 80 MeV in the residual A-1 nucleus. The remaining fraction of about 50% could be attributed to multi-nucleon knockout, pion production, single-nucleon knockout to more complex states, ... Adding all these contributions would move the calculations closer to the data.

5.4 Strangeness of the nucleon

Parity-violating scattering reactions can be used to probe specific nucleonic properties which remain concealed in parity-conserving processes. A subject that has gained wide interest concerns the contribution of the sea quarks to the nucleon properties such as spin, charge and magnetic moment. From the late 1990's on, parity-violating electron scattering (PVES) has become a tool for hadron physics research at electron accelerator facilities. Mirror measurements such as SAMPLE [199, 200] at MIT-Bates, HAPPEX [201, 202, 203] and G0 [204] at JLAB, A4 [205, 206] at MAMI and E158 [207] at SLAC aim at probing the strange-quark effects in proton structure. In the first place, these collaborations focus on the strange electric and magnetic form factors. So far, the collected data point towards an electric strange form factor consistent with zero while the magnetic strange form factor seems to prefer positive values. Radiative corrections heavily complicate the extraction of the strange axial form factor g_A^s from the data. In the analysis of the parity-violating asymmetry observed in the PVES experiments, one estimates the effect of g_A^s relying on results of deep-inelastic double-polarized scattering experiments [208, 209, 210, 211]. The abovementioned PVES programs triggered many theoretical studies of the strangeness magnetic moment and charge radius. These calculations are performed in a rich variety of hadron models, yielding predictions for the strangeness parameters covering a wide range of values [176, 212, 213, 214, 215, 216, 217, 218, 219, 220]. A recent review of the theoretical and experimental

status can be found in Ref. [221].

An alternative method of addressing the strangeness content of the nucleon is by means of neutrino-nucleus scattering. In contrast to PVES experiments, in extracting g_A^s no radiative corrections need to be applied. Data for $(\nu, \nu' N)$ and $(\overline{\nu}, \overline{\nu}' N)$ elastic scattering cross sections were collected at BNL [186]. As carbon was used as target material, an accurate understanding of nuclear corrections is a prerequisite for reliably extracting the strange-quark matrix elements from the data. Examples of relativistic studies which address the issue of computing the nuclear corrections, are the RFG model of Ref. [163] and the RDWIA models of Refs. [168, 169, 171, 189, 222]. As absolute cross-section measurements involving neutrinos are challenging, a lot of effort has been devoted to the study of cross-section ratios. Examples include the ratio of proton-to-neutron knockout NC neutrino-nucleus interactions [169, 171, 173, 189, 222, 223, 224], the ratio of NC to CC cross sections [188, 189, 225] and the ratio of NC to CC neutrino-antineutrino asymmetries [189, 222, 226]. For these ratios, the effects of nuclear corrections nearly cancel, facilitating the extraction of possible strange-quark contributions. Other observables which do not require absolute cross-section measurements are polarization asymmetries. Recently, the nucleon helicity asymmetry A_l was put forward as a potential tool to discriminate between neutrinos and antineutrinos in NC neutrino-induced nucleon-knockout reactions off nuclei [166, 167]. In this section, we wish to show that the quantity A_l for antineutrinos is also very sensitive to sea-quark contributions to the vector form factors. We should point out that measuring polarization asymmetries at current neutrino facilities is extremely challenging. Still, we consider our findings as a valuable theoretical insight, since the ratios discussed in Refs. [171, 173, 188, 222, 224, 225] mainly focus on effects stemming from g_A^s. Often, the extraction of physical information from observables involving nuclei suffer from an incomplete knowledge of medium effects. Here, we employ the RMSGA formalism to describe the nucleon helicity asymmetry within NC neutrino-nucleus scattering processes. It will be shown that A_l remains relatively free of medium-related ambiguities.

First, we briefly shed light on the strangeness form factors entering Eqs. (5.72) and (5.64). Next, we present our results for the cross-section ratios which are usually employed to extract information on the axial strangeness contribution. Finally,

we scrutinize the nucleon helicity asymmetry A_l.

5.4.1 Strangeness form factors

So far, we neglected strangeness contributions to the weak vector and axial form factors of Eqs. (5.64) and (5.72) ($F_1^s = F_2^s = g_A^s = 0$). To quantify the impact of the axial strangeness contribution on G_A, we adopt the value g_A^s= $-$ 0.19, which we consider as an upper limit. Indeed, g_A^s= $-$ 0.19 was extracted from an $SU(3)$-based analysis of deep inelastic double-polarized scattering experiments [208]. Recent neutrino and parity-violating electron scattering experiments point towards smaller values for g_A^s [186, 209, 210, 211].

Model	Ref.	$\mu_s(\mu_N)$	r_s^2(fm^2)
VMD	[212]	-0.31	0.16
$K\Lambda$	[213]	-0.35	-0.007
CBM	[214]	-0.1	-0.011
Hybrid	[215]	-0.3	-0.025
Chiral Quark	[216]	-0.09	-0.035
NJL	[176, 217]	-0.45	-0.17
Skyrme	[218]	-0.13 – -0.57	-0.1 – -0.15
Disp. Rel.	[219]	-0.28	0.42
CQS (π)	[220]	0.074	-0.22
CQS (K)	[220]	0.115	-0.095

Table 5.2 Predictions for r_s^2 and μ_s in various hadron models.

In addition to sea-quark effects in the axial current, there can be contributions to the Dirac and Pauli vector form factors. A three-pole ansatz of Forkel *et al.* [227] resulted in the following parametrization

$$F_1^s = \frac{1}{6}\frac{-r_s^2 Q^2}{(1+Q^2/M_1^2)^2} \ , \tag{5.76}$$

$$F_2^s = \frac{\mu_s}{(1+Q^2/M_2^2)^2} \ , \tag{5.77}$$

with M_1=1.3 GeV and M_2=1.26 GeV [227]. The r_s^2 and μ_s predicted by various hadronic structure models are summarized in Table 5.2. The list is not exhaustive. There is a tendency towards a mildly negative strangeness magnetic moment

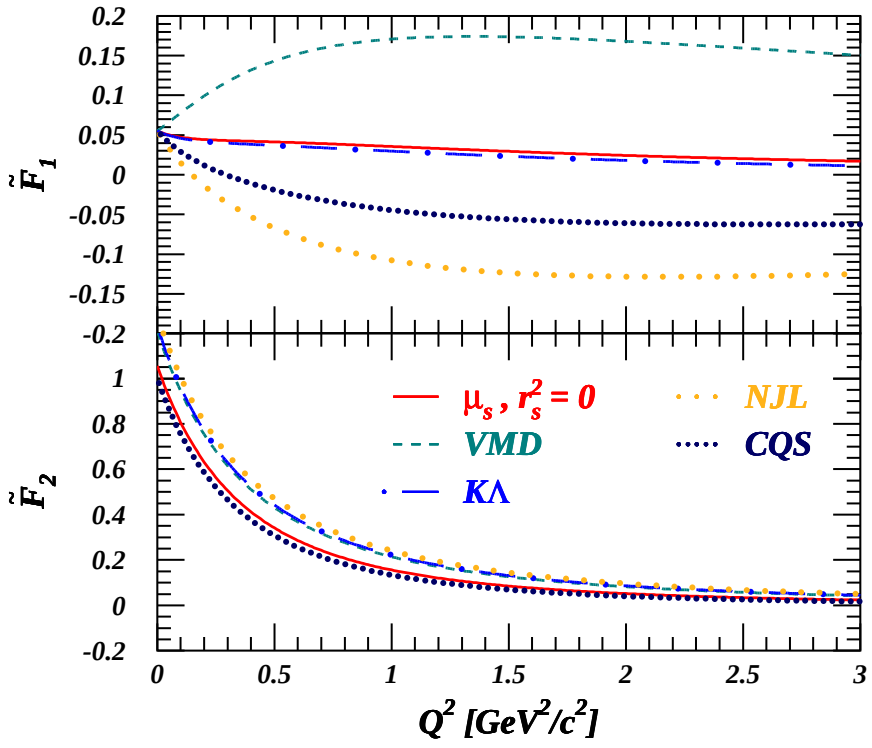

Figure 5.10 Sensitivity of the proton Dirac (upper panel) and Pauli (lower panel) neutral-current vector form factors to strange-quark contributions. The solid line represents the form factors in the absence of any strangeness contribution. The dashed, dot-dashed, long-dotted and short-dotted curves include non-zero strangeness contributions in the parametrization of Eqs. (5.76) and (5.77). The adopted values for r_s^2 and μ_s are those of four different hadron models (VMD [212], KΛ [213], NJL [176] and CQS(K) model [220]) and can be found in Table 5.2.

($\mu_s \approx -0.3\ \mu_N$), and a small negative strangeness radius ($r_s^2 \approx -0.01\ fm^2$). All PVES experiments performed so far, however, hint at a positive value for μ_s. In our investigations we will use the predictions for r_s^2 and μ_s from the vector meson dominance (VMD), the KΛ, the Nambu-Jona-Lasinio (NJL) and the chiral quark soliton (CQS(K)) model. These values are selected as we find them representative for the full range of values regarding the strangeness parameters. We wish to stress that

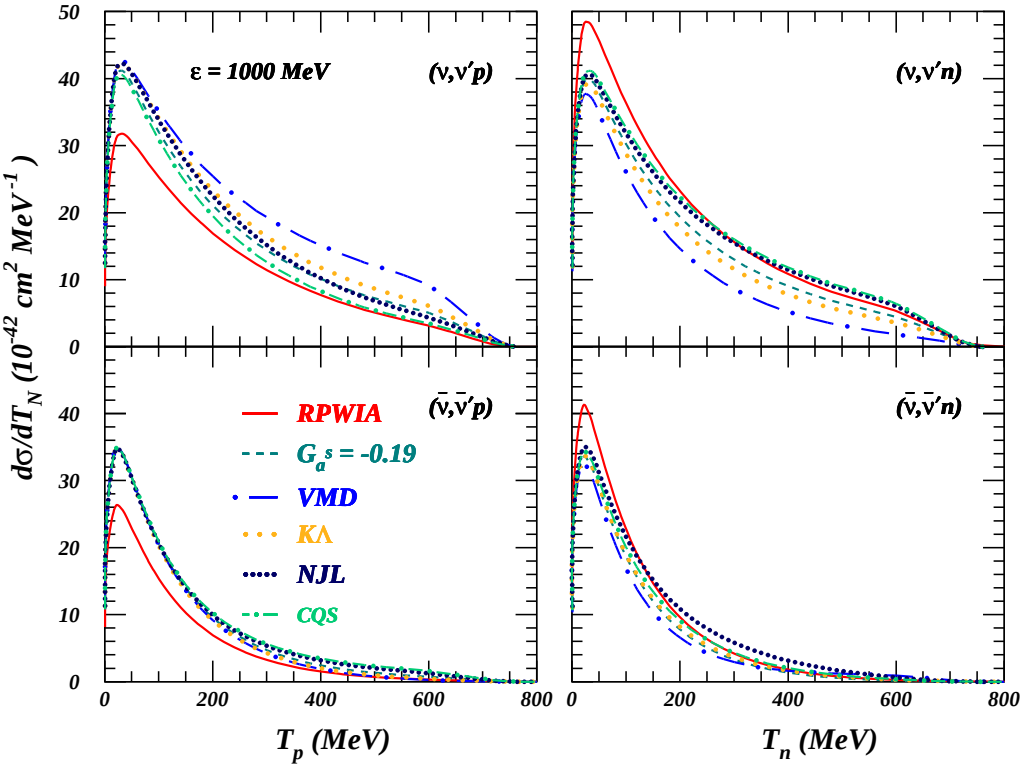

Figure 5.11 Influence of sea-quarks on the NC cross sections for ^{12}C as a function of the outgoing nucleon kinetic energy T_N at ε=1000 MeV. The left (right) panel corresponds to proton (neutron) ejectiles. The solid curve represents the RPWIA results without strangeness. The other curves adopt $g_A^s = -0.19$ and correspond to different values for r_s^2 and μ_s : $(r_s^2{=}0, \mu_s{=}0)$ (dashed), VMD (long dot-dashed) [212], KΛ (long-dotted)[213], NJL (short-dotted)[176] and CQS(K) (short dot-dashed)[220].

all forthcoming results for the effect of strangeness in the weak vector form factors on A_l, account for sea-quark effects in the axial current. Hence, the interference between the axial and magnetic strange form factors is always present.

In Fig. 5.10, the proton Dirac F_1^Z and Pauli F_2^Z NC form factors are shown for various parametrizations for F_1^s and F_2^s. The solid line provides the value in the absence of strangeness contributions. This figure reveals that mainly F_1^Z is affected. The VMD model predicts that strangeness mechanisms increase F_1^Z by

about a factor of three. All other models lead to less spectacular modifications in the absolute magnitude. The relatively large and negative r_s^2 values from the NJL and CQS(K) nucleon models make the strangeness parts to change the sign of F_1^Z. Strangeness effects for the Pauli form factor F_2^Z are far less pronounced due to its large absolute value. Thus, one can expect that mainly variations in r_s^2 will be reflected in the helicity asymmetry.

The effect of a non-zero strange-quark contribution to the axial and vector form factors on the NC cross sections for ^{12}C is shown in Fig. 5.11. Results are displayed for proton and neutron emission at ε=1000 MeV. As expected from Eq. (5.72), possible axial strangeness contributions work in opposite directions for proton and neutron knockout. Indeed, the introduction of $g_A^s = -0.19$ induces an enhancement (proton knockout) or a reduction (neutron knockout) by $\approx 20\%$. The VMD amplifies this opposite behaviour, whereas the effects of the KΛ, the NJL and the CQS(K) models are rather modest. This clearly illustrates the well-known feature that in hunting sea-quarks in neutrino or PVES reactions, it is essential to discriminate between protons and neutrons. Indeed, the effects stemming from the sea tend to cancel when summing over the proton and neutron cross sections.

As stated above, measuring absolute cross sections is a rather hard experimental task, and a lot of effort has been devoted to ratios. Before scrutinizing the nucleon helicity asymmetry, we first focus on the ratios which are commonly adopted in literature to extract information on the axial strangeness contributions [171, 173, 188, 222, 224, 225].

5.4.2 Cross-section ratios

One of the interesting quantities proposed to study strangeness effects is the ratio of proton-to-neutron knockout NC neutrino-nucleus interactions [169, 171, 173, 189, 222, 223, 224]

$$R_{p/n} = \left(\frac{d\sigma}{dT_N}\right)^{NC}_{(\nu,p)} \Big/ \left(\frac{d\sigma}{dT_N}\right)^{NC}_{(\nu,n)} . \tag{5.78}$$

This ratio is very sensitive to axial strangeness contributions, since a non-zero value for g_A^s will pull the denominator and the numerator into opposite directions, due to the τ_3 factor in Eq. (5.72). Fig. 5.12 displays $R_{p/n}$ for both neutrino and antineutrino NC interactions on ^{12}C at ε=1000 MeV. As can be inferred, the impact of FSI is

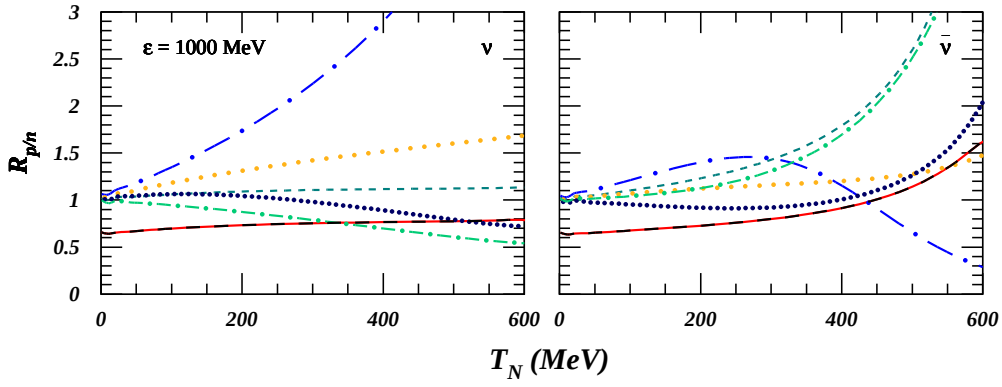

Figure 5.12 Ratio of the proton-to-neutron NC cross sections for quasi-elastic scattering on ^{12}C. The left and right panels correspond to neutrinos and antineutrinos, respectively. Line convention as in Fig. 5.11. The black dashed line shows the impact of FSI in the RMSGA formalism.

indeed marginal for this kind of observables. The ratio is enhanced by $\approx 40\%$ when $g_A^s = -0.19$. The VMD and KΛ models tend to amplify this enhancement, whereas the NJL predictions nearly cancel it. Our results comply with the ones of [169, 189, 222, 223].

The accurate measurement of $R_{p/n}$, however, is problematic in neutrino scattering experiments due to the intrinsic difficulties and uncertainties involved with neutron detection. For this reason, FINeSSE will focus on a measurement of the ratio of NC to CC cross sections

$$R_\nu = \left(\frac{d\sigma}{dT_N}\right)^{NC}_{(\nu,p)} \Big/ \left(\frac{d\sigma}{dT_N}\right)^{CC}_{(\nu,p)} , \tag{5.79}$$

$$R_{\overline{\nu}} = \left(\frac{d\sigma}{dT_N}\right)^{NC}_{(\overline{\nu},p)} \Big/ \left(\frac{d\sigma}{dT_N}\right)^{CC}_{(\overline{\nu},n)} . \tag{5.80}$$

The CC reaction, being purely isovector, is insensitive to g_A^s. Accordingly, R_ν and $R_{\overline{\nu}}$ are about a factor two less sensitive to g_A^s than $R_{p/n}$. Nevertheless, they are more suitable to extract experimental information about g_A^s. Fig. 5.13 shows our RMSGA results for R_ν and $R_{\overline{\nu}}$ for ^{12}C at ε=1000 MeV. The enhancement at large ejectile ki-

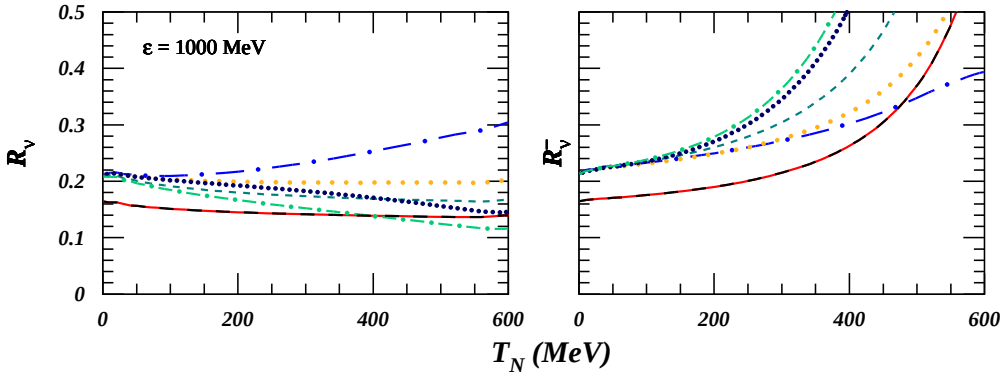

Figure 5.13 Ratio of neutral-to-charged current cross sections for quasi-elastic scattering on ^{12}C. Left (right) panel corresponds to neutrinos (antineutrinos). Line convention as in Fig. 5.12.

netic energies is due to the fact that the CC cross section goes to zero more rapidly than the corresponding NC one. The impact of FSI can be safely neglected. The axial strangeness induces for both neutrinos and antineutrinos an enhancement. The increase is more outspoken for antineutrinos. The vector strangeness contributions affect R_ν and $R_{\overline{\nu}}$ in opposite directions, and might cancel effects stemming from g_A^s. Our results are in line with the ones of Ref. [189], but substantially differ from the ones of Ref. [188]. These differences are mainly due to deviations in the calculations for NC cross sections (see Sec. 5.3).

In Ref. [226] it is proposed to employ the asymmetry

$$A_p = \frac{\left(\frac{d\sigma}{dT_N}\right)^{NC}_{(\nu,p)} - \left(\frac{d\sigma}{dT_N}\right)^{NC}_{(\overline{\nu},p)}}{\left(\frac{d\sigma}{dT_N}\right)^{CC}_{(\nu,p)} - \left(\frac{d\sigma}{dT_N}\right)^{CC}_{(\overline{\nu},n)}} \,, \tag{5.81}$$

in order to investigate the impact of strange-quark contributions. For the sake of completeness, we show in Fig. 5.14 our RMSGA results for this asymmetry for proton knockout on ^{12}C at ε=1000 MeV. Once again, FSI can be disregarded for this kind of observable, and the axial strangeness induces an enhancement of A_p. At

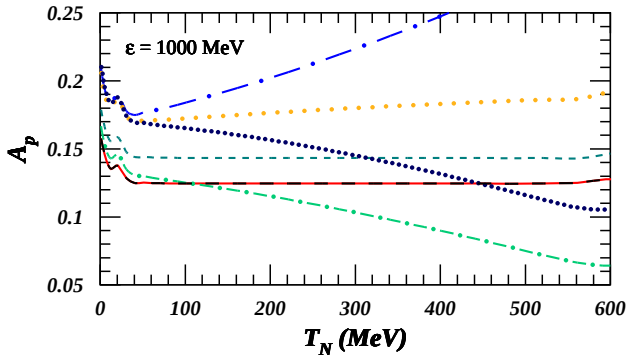

Figure 5.14 The asymmetry of Eq. (5.81) for ^{12}C at ε=1000 MeV. Line convention as in Fig. 5.12.

$T_N \rightarrow 0 (Q^2 \rightarrow 0)$, the hadron models that predict a negative μ_s (VMD,KΛ,NJL) amplify this enhancement, whereas the CQS(K) (positive μ_s) slightly extinguish the increase. Depending on the sign of r_s^2, this enhancement becomes more or less pronounced with increasing ejectile kinetic energies. To be perfectly clear, the effect of varying r_s^2 and μ_s separately is studied in Fig. 5.15. Our results are once more in very well agreement with the ones of Refs. [189, 222, 226].

5.4.3 Nucleon helicity asymmetries

The expression for the differential cross section in Eq. (5.37) involves an averaging over the ejectile's spin. Fixing the helicity $h_N = \frac{\vec{\sigma}_N \cdot \vec{k}_N}{|\vec{k}_N|}$ of the ejectile, yields

$$\frac{d\sigma}{dT_N}(h_N) = \frac{M_N M_{A-1}}{(2\pi)^3 M_A} 4\pi^2 \int \sin\theta_l d\theta_l \int \sin\theta_N d\theta_N k_N f_{rec}^{-1} \sigma_M$$
$$\times \left[v_L (R_L^o + h_N R_L^l) + v_T (R_T^o + h_N R_T^l) + h v_{T'} (R_{T'}^o + h_N R_{T'}^l) \right] , \quad (5.82)$$

where the indices o and l refer to the unpolarized and longitudinally polarized responses, respectively.

The longitudinal polarization asymmetry A_l is then defined as the difference in yield for the two possible helicity states of the ejected nucleon N, normalized to the

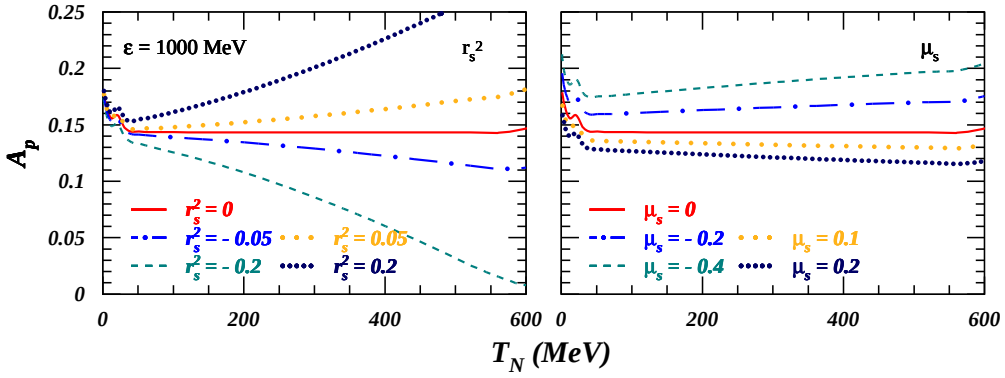

Figure 5.15 The asymmetry of Eq. (5.81) for ^{12}C at ε=1000 MeV.The solid line shows the RPWIA predictions with $g_A^s = -0.19$. The left (right) panel gives the influence of varying strangeness radius (magnetic moment).

total differential nucleon knockout cross section:

$$A_l(T_N) = \frac{\frac{d\sigma}{dT_N}(h_N = +1) - \frac{d\sigma}{dT_N}(h_N = -1)}{\frac{d\sigma}{dT_N}(h_N = +1) + \frac{d\sigma}{dT_N}(h_N = -1)}\,, \tag{5.83}$$

Before embarking on the study of possible strangeness effects, we wish to determine the degree to which A_l is affected by variations in the parametrizations for the electromagnetic form factors and typical medium effects like FSI and off-shell ambiguities. We consider the ^{12}C target as a test case. We take RPWIA calculations as baseline results, with dipole form factors and the current operator in the $CC2$ form of Eq. (5.38).

As mentioned earlier, in Ref. [166] the helicity asymmetry A_l was put forward as a lever to discriminate between neutrinos and antineutrinos in NC reactions on nuclei. Predictions for this asymmetry were obtained in a non-relativistic plane-wave impulse approximation framework and results up to beam energies of 500 MeV were presented. At impinging (anti)neutrino energies of the order of GeV's, any realistic model for describing the reaction processes requires the inclusion of relativistic effects. In Fig. 5.16, we show the RPWIA predictions for A_l for beam energies ranging from 200 to 5000 MeV. Clearly, up to lepton energies of 1 GeV, the

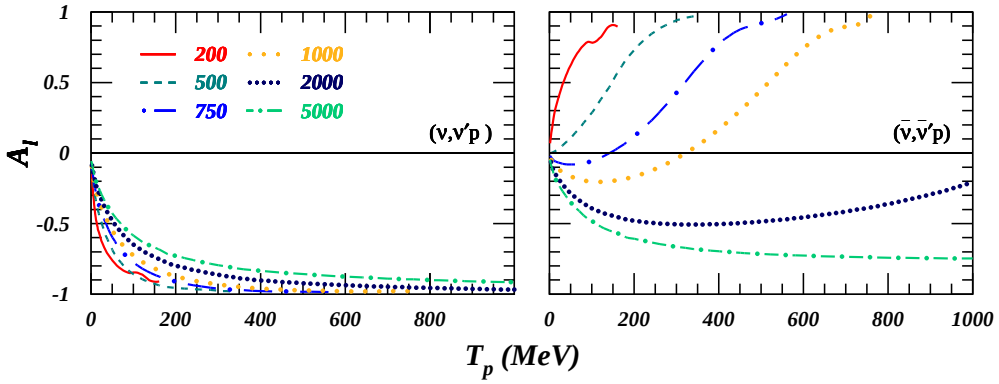

Figure 5.16 The helicity asymmetry as a function of T_p for proton knockout from ^{12}C at six beam energies. The left (right) panel is for neutrinos (antineutrinos).

A_l has an opposite sign for $A(\nu, \nu' N)$ and $A(\overline{\nu}, \overline{\nu}' N)$. Apparently, the discriminative power of A_l dwindles when higher beam energies are considered. The antineutrino proton asymmetry $A_l(T_p)$ evolves from a dominance of $h_N = +1$ contributions at beam energies below 1 GeV to a supremacy of $h_N = -1$ ones at higher energies. This can be attributed to the role played by the $G_A F_2^Z$ interference contribution, which gains in importance as the neutrino energy grows. The transverse response function R_T in the cross section of Eq. (5.37) becomes increasingly dominant when higher energies are probed, thereby extinguishing the distinction between left- and right-handed neutrino fields in the differential cross sections $d\sigma/dT_N$.

None of the results for A_l shown so far, including those of Refs. [166, 167], did account for the effects of FSI. As already stated in the introduction, it is a common outcome of model calculations of various sorts that FSI do not play a major role in ratios of cross sections, albeit being important in the corresponding inclusive cross sections [184]. Fig. 5.17 displays the effect of FSI mechanisms on A_l as computed in the RMSGA model at impinging beam energies of 500 and 1000 MeV. As can be appreciated, the global influence of FSI mechanisms on A_l is indeed almost negligible. In the ratio A_l, a strong cancellation of FSI is noticed, even at relatively low ejectile kinetic energies. Henceforth, we will concentrate on results for an imping-

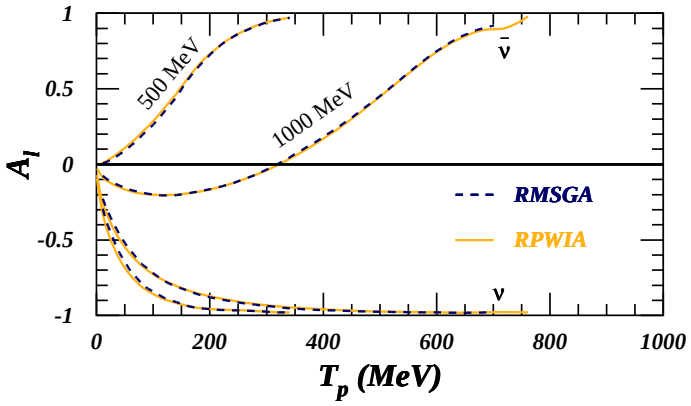

Figure 5.17 The effect of FSI mechanisms on the helicity asymmetry at 500 MeV and 1000 MeV beam energies. The solid (dashed) line shows the RPWIA (RMSGA) predictions.

ing (anti)neutrino energy of ε=1000 MeV. At this energy, the neutrino scattering process can be expected to be dominated by the quasi-elastic contribution.

Another possible source of uncertainty when determining A_l may be the insufficient knowledge regarding the electromagnetic form factors of the proton. To this end, we performed calculations with two parametrizations: the standard dipole form and the recent BBA-2003 parametrization of Ref. [54]. As becomes clear from the left panel of Fig. 5.18, both produce comparable results. Therefore, all forthcoming results use the traditional dipole for G_E and G_M. We also wish to estimate the role of off-shell ambiguities on the computed A_l values. To that purpose we performed calculations with the current operators of Eqs. (5.38) and (5.39). As Fig. 5.18 shows that all these current operators produce more or less equivalent results, the sensitivity of A_l to off-shell ambiguities is minor.

The nucleon helicity asymmetry A_l emerges as a robust observable, which is not burdened by a large sensitivity to medium corrections. Accordingly, we are tempted to study variations in A_l due to strange-quark contributions. The results contained in Figs. 5.16, 5.17 and 5.18 reveal that neutrinos are extremely selective with respect to the helicity of the ejectile. As a consequence, one can expect that

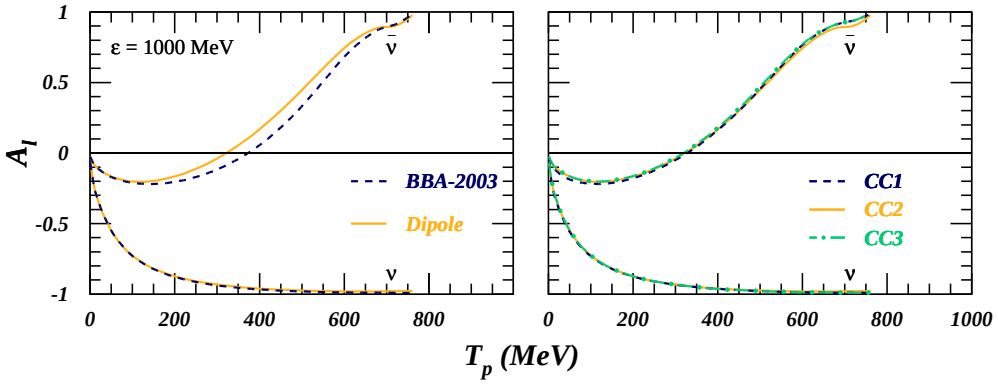

Figure 5.18 The helicity asymmetry A_l as a function of the proton kinetic energy at ε=1000 MeV as computed in an RPWIA approach. The left panel illustrates the effects stemming from the ambiguities in the electromagnetic form factors: the solid (dashed) line shows the RPWIA results obtained with the dipole (BBA-2003) parametrization. In the right panel the role of the off-shell ambiguities is studied. The solid, dashed, dot-dashed curves are obtained with the CC2, CC1 and CC3 prescription, respectively.

any strangeness contribution will nearly cancel in the ratio of Eq. (5.83). The helicity selectivity is not so pronounced antineutrinos. Hence, antineutrinos represent a better lever than neutrinos when it comes to probing strange-quark contributions through the observable A_l. Fig. 5.19 shows our predictions for the helicity asymmetry at ε=1000 MeV for both proton and neutron knockout in $\overline{\nu}$-^{12}C reactions. For both protons and neutrons, the introduction of a non-zero g_A^s does not substantially alter the baseline results (denoted as RPWIA in the figure). The introduction of non-zero strangeness radius and magnetic moment, on the other hand, seriously affects the ratio between $h_N = +1$ and $h_N = -1$ ejectiles. The largest deviations emerge using the predictions of the VMD model ($r_s^2 > 0$). In any case, the overall impact of F_1^s and F_2^s on the helicity asymmetry is substantially larger than the effect caused by FSI mechanisms, off-shell ambiguities and g_A^s, even when for the value of the latter an upper limit is adopted. As can be inferred from Fig. 5.19, the strange contribution to the weak vector form factors has a comparable impact on the A_l for protons and neutrons, but acts in opposite directions. Once again, this

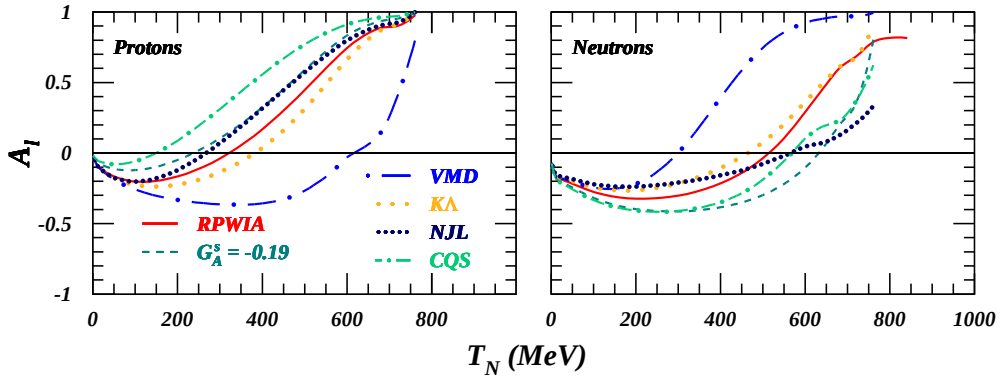

Figure 5.19 Influence of sea-quarks on the helicity asymmetry at ε=1000 MeV. The left panel shows the asymmetry for antineutrino-induced proton knockout on ^{12}C, whilst the right one shows the asymmetry for antineutrino-induced neutron knockout. The solid curve represents the RPWIA results without strangeness. The other curves adopt $g_A^s = -0.19$ and correspond to different values for r_s^2 and μ_s : $(r_s^2{=}0, \mu_s{=}0)$ (dashed), VMD (long dot-dashed) [212], KΛ (long-dotted)[213], NJL (short-dotted)[176] and CQS(K) (short dot-dashed)[220].

confirms that one is obliged to discriminate between protons and neutrons in order to probe sea-quark effects.

The effect of varying r_s^2 and μ_s independently is studied in Fig. 5.20. In the right panel, we investigate the effect of varying μ_s at r_s=0. The left panel, on the other hand, displays the effect of varying r_s^2 at μ_s=0. From the theoretical predictions listed in Table 5.2 one infers a range of values $-0.4 \lesssim \mu_s \lesssim 0.2$ and $-0.22 \lesssim r_s^2 \lesssim 0.42$. Fig. 5.20 illustrates that the largest changes in A_l are induced by variations in the strangeness radius r_s^2.

Fig. 5.16 revealed that the helicity asymmetry is very sensitive to the energy of the (anti)neutrino beam. Any experiment involving neutrinos has limited capabilities to precisely determine the initial (anti)neutrino energies. Therefore, we investigated to what extent the sensitivity of A_l to strangeness effects persists, when it is folded over a realistic antineutrino spectrum. To this end, we have computed A_l as a function of the proton energy as it could be determined at an experiment like FINeSSE, provided that it possesses the capabilities to determine outgoing nucleon

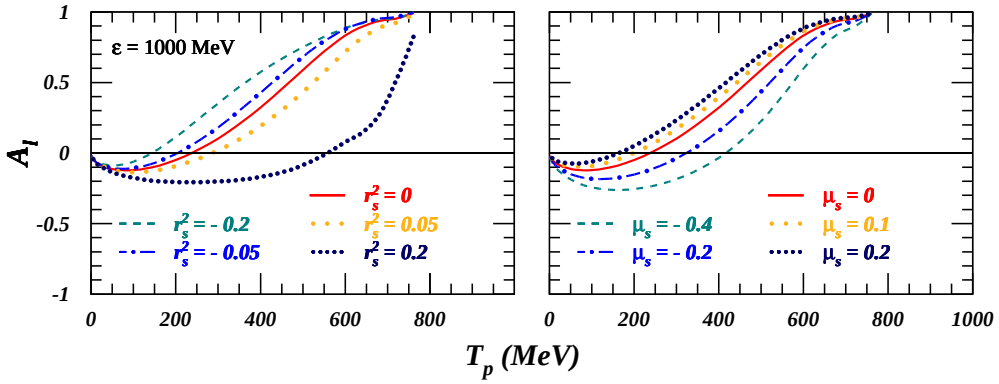

Figure 5.20 The helicity asymmetry for antineutrino-induced proton knockout at ε=1000 MeV. The solid line shows the RPWIA predictions with $g_A^s = -0.19$. The left (right) panel gives the influence of varying strangeness radius (magnetic moment).

helicities. A typical beam spectrum of FINeSSE is displayed in Fig. 5.21 [228]. The average beam energy corresponds to $\langle\varepsilon\rangle \approx 600$ MeV. The flux-averaged differential cross section is defined as

$$\left\langle \frac{d\sigma}{dT_N}(h_N) \right\rangle = \frac{\int_{\varepsilon_{min}}^{\varepsilon_{max}} \Phi(\varepsilon) \frac{d\sigma}{dT_N}(\varepsilon, h_N) d\varepsilon}{\int_{\varepsilon_{min}}^{\varepsilon_{max}} \Phi(\varepsilon) d\varepsilon} \ , \tag{5.84}$$

with $\Phi(\varepsilon)$ the typical FINeSSE antineutrino spectrum of Fig. 5.21, ε_{min}=75 MeV and ε_{max}=2375 MeV.

Fig. 5.22 shows the flux-averaged helicity asymmetry for antineutrino-induced proton knockout from ^{12}C. The strange-quark effects remain substantial for the flux-averaged A_l and similar trends emerge as those observed in Fig. 5.19 which refers to a well-defined impinging antineutrino energy.

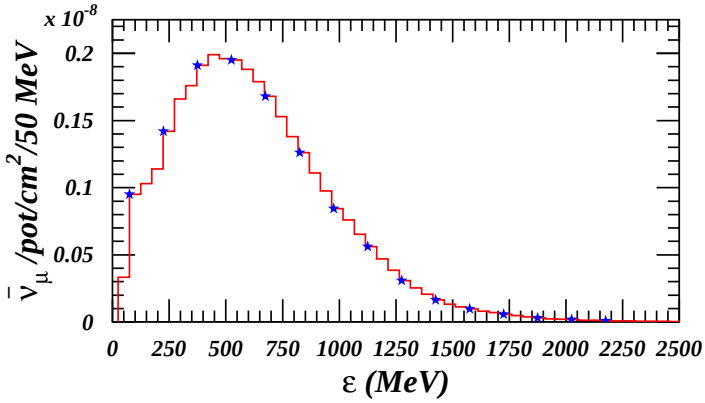

Figure 5.21 A typical FINeSSE antineutrino-flux on the FNAL booster Neutrino beamline [228]. The average beam energy corresponds to $\langle\varepsilon\rangle \approx 600$ MeV. The blue stars indicate the energies for which calculations were performed.

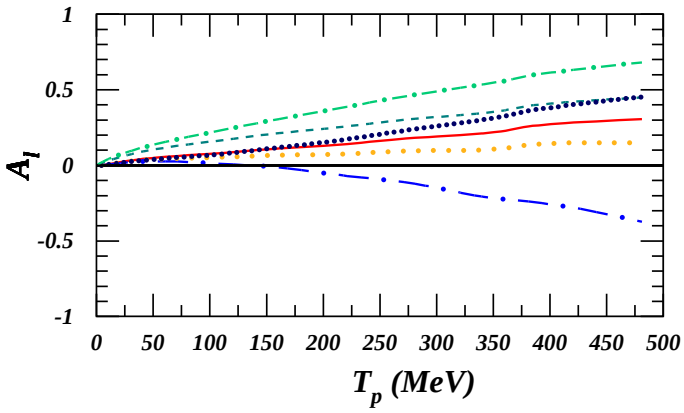

Figure 5.22 The flux-averaged helicity asymmetry for antineutrino-induced proton knock-out at $\langle\varepsilon\rangle$=600 MeV. Line convention as in Fig. 5.19.

Chapter 6

Conclusions

In this work we have outlined a fully unfactorized relativistic eikonal framework for modeling quasi-elastic electron- and neutrino-nucleus scattering processes. Our framework is a very flexible one as it can be used in conjunction with relativistic optical potentials (ROMEA) or within a Glauber multiple-scattering approach (RMSGA) to deal with final-state interactions (FSI). To our knowledge, all Glauber calculations reported in literature are performed within a non-relativistic and factorized scheme. Formally, the model bears a strong resemblance with the RDWIA approaches which have been developed over the last number of decades. In particular, it relies on the impulse approximation to establish the lepton-nucleus coupling, and the bound-state wave functions are obtained within the Hartree approximation to the $\sigma - \omega$ model.

The major differences between the various approaches arise in the description of the propagation of the struck nucleon. The ROMEA and RDWIA frameworks are similar in the sense that both of them incorporate FSI in terms of optical potentials, obtained from proton-nucleus elastic scattering experiments. Whereas the RDWIA adopts exact solutions of the Dirac equation, the ROMEA framework relies on the eikonal approach (EA) to calculate the scattering wave function. The EA finds its origin in optics and is expected to be a valid one for proton emission in a cone with a relatively small opening angle about the direction of the virtual photon's momentum. The EA is particularly convenient at high proton kinetic energies, where approaches relying on partial-wave expansions become impractical.

Given the highly inelastic character and diffractive nature of the nucleon-nucleon

cross sections for proton lab momenta exceeding 1 GeV, the use of optical potentials for modeling FSI processes does not seem natural. Here, our RMSGA framework, which is a multiple-scattering extension of the EA, offers a valid and economical alternative. In this framework, the effects of FSI are computed directly from the elementary nucleon-nucleon scattering data through the introduction of a profile function.

One of the primary goals of this thesis was to put the various approximations underlying the presented ROMEA and RMSGA formalisms to stringent tests. Nuclear transparencies in $A(e,e'p)$ reactions revealed that the eikonal approximation is adequate down to remarkably low ejectile kinetic energies. Moreover, the comparison of the ROMEA and RDWIA predictions for the normal induced polarization confirmed this finding and implied that one can rely on the EA down to proton kinetic energies of $T_p \approx 200$ MeV. The same nuclear transparency was employed to focus on the differences between "nucleon-nucleus" (RDWIA) and "nucleon-nucleon" (RMSGA) models. Comparable predictions were obtained for kinematic regimes where both models are applicable, giving us confidence that the "low-energy" and "high-energy" regime can be bridged in a smooth manner. The normal induced polarization, however, revealed that the RMSGA in its present form, i.e. relying on spin-independent nucleon-nucleon scattering amplitudes , is still open for improvement concerning the description of certain polarization observables.

In conjunction with probing the mutual consistency of the RDWIA,ROMEA and RMSGA frameworks, this work aimed at studying issues which attract a lot of attention in intermediate-energy physics. In particular, the measured $A(e,e'p)$ nuclear transparencies for ^{12}C, ^{56}Fe and ^{208}Pb received a satisfying description in our theoretical frameworks, providing no sound evidence for the onset of the color transparency phenomenon up to $Q^2 \approx 8.1$ (GeV/c)^2. In addition, we paid attention to the delicate question whether or not nucleons are modified when they are embedded in the nuclear medium. To that purpose, we performed RMSGA calculations for the transferred polarization components for the target nuclei ^{4}He and ^{16}O, and compared them to the world data. The numerical calculations employed both free and medium-modified electromagnetic form factors, using the predictions of a quark-meson coupling (QMC) model, a chiral-quark soliton (CQS) model and a

modified Skyrme model. For ^{4}He , substantial deviations between the RMSGA predictions and the data were observed. The implementation of the in-medium form factors from the QMC and CQS nucleon models made the RMSGA calculations to go in the right direction and induced changes in the ratio of the polarization-transfer components, which were of the right order of magnitude to explain the discrepancies. The ^{16}O data, however, were well described adopting free-proton electromagnetic form factors. A recently approved experiment will need to clarify this controversial issue.

Finally, we extended the RMSGA formalism in order to deal with quasi-elastic inclusive neutrino-nucleus interactions. The extension was straightforward since the electromagnetic and the weak interaction are closely intertwined in the standard model. In addition, the propagation of the struck nucleon can be readily assumed to be independent of the nature of the leptonic probe. Excellent agreement with the RDWIA framework was reached in the relativistic plane-wave limit (RPWIA), lending us support that our RPWIA results can serve as benchmark calculations. These are crucial since we argued that one can estimate the effect of FSI mechanisms on the quasi-elastic inclusive neutrino-nucleus cross sections by a scaling of the RPWIA results with the transparency factors extracted from $A(e, e'p)$ measurements. To finish, we studied the influence of strange-quark contributions to the weak form factors, employing the predictions of a range of hadronic structure models. We performed calculations for the ratio proposed by the FINeSSE program. In addition, we suggested an alternative way of exploring the strangeness content of the nucleon. The helicity asymmetry, that gives a measure of the difference in yield for the two possible ejectile helicity states, turned out to be heavily sensitive to sea-quark contributions in the weak vector form factors.

Appendix A

Notations and conventions

A.1 Glossary

OPEA	One-Photon Exchange Approximation
IA	Impulse Approximation
FSI	Final-State Interactions
(R)DWIA	(Relativistic) Distorted-wave Impulse Approximation
EA	Eikonal Approximation
ROMEA	Relativistic Optical-Model Eikonal Approximation
EMA	Effective Momentum Approach
RMSGA	Relativistic Multiple-Scattering Glauber Approximation
CT	Color Transparency
(R)PWIA	(Relativistic) Plane-Wave Impulse Approximation
PLC	Point-Like Configuration
CSR	Coulomb Sum Rule
MEC	Meson-Exchange Currents
IC	Isobar Currents
QMC	Quark-Meson Coupling
CQS	Chiral-Quark Soliton
CBM	Cloudy Bag Model
SRC	Short-Range Correlations
RFG	Relativistic Fermi Gas
QE	Quasi-Elastic

NC	Neutral-Current
CC	Charged-Current
CVC	Conserved Vector Current hypothesis
PCAC	Partially Conserved Axial Current hypothesis
PVES	Parity-Violating Electron Scattering
VMD	Vector Meson Dominance
NJL	Nambu-Jona-Lasinio

A.2 Isospin and Gell-Mann matrices

The Pauli spin and isospin operators are defined as

$$t_1 = \begin{pmatrix} 0 & 1 \\ 1 & 0 \end{pmatrix} , \qquad t_2 = \begin{pmatrix} 0 & -i \\ i & 0 \end{pmatrix} , \qquad t_3 = \begin{pmatrix} 1 & 0 \\ 0 & -1 \end{pmatrix} , \tag{A.1}$$

and $t_\pm = (t_1 \pm i t_2)$.

The standard Gell-Mann representation of $SU(3)$ generators is given by

$$\begin{aligned} \lambda_1 &= \begin{pmatrix} 0 & 1 & 0 \\ 1 & 0 & 0 \\ 0 & 0 & 0 \end{pmatrix} , \qquad \lambda_2 = \begin{pmatrix} 0 & -i & 0 \\ i & 0 & 0 \\ 0 & 0 & 0 \end{pmatrix} , \qquad \lambda_3 = \begin{pmatrix} 1 & 0 & 0 \\ 0 & -1 & 0 \\ 0 & 0 & 0 \end{pmatrix} \\ \lambda_4 &= \begin{pmatrix} 0 & 0 & 1 \\ 0 & 0 & 0 \\ 1 & 0 & 0 \end{pmatrix} , \qquad \lambda_5 = \begin{pmatrix} 0 & 0 & -i \\ 0 & 0 & 0 \\ i & 0 & 0 \end{pmatrix} , \qquad \lambda_6 = \begin{pmatrix} 0 & 0 & 0 \\ 0 & 0 & 1 \\ 0 & 1 & 0 \end{pmatrix} \\ \lambda_7 &= \begin{pmatrix} 0 & 0 & 0 \\ 0 & 0 & -i \\ 0 & i & 0 \end{pmatrix} , \qquad \lambda_8 = \frac{1}{\sqrt{3}} \begin{pmatrix} 1 & 0 & 0 \\ 0 & 1 & 0 \\ 0 & 0 & -2 \end{pmatrix} , \end{aligned} \tag{A.2}$$

with $\lambda_\pm = (\lambda_1 \pm i\lambda_2)$.

Bibliography

[1] G. Jacob and T. Maris, Nucl. Phys. **32,** 139 (1962).

[2] U. Amaldi *et al.*, Phys. Rev. Lett. **13,** 341 (1964).

[3] V. Pandharipande, I. Sick, and P. deWitt Huberts, Rev. Mod. Phys. **69,** 981 (1997).

[4] H. Müther and A. Polls, Prog. Part. Nucl. Phys. **45,** 243 (2000).

[5] D. Rohe *et al.*, Phys. Rev. Lett. **93,** 182501 (2004).

[6] J. Gao *et al.*, Phys. Rev. Lett. **84,** 3265 (2000).

[7] D. Dutta *et al.*, Phys. Rev. C **68,** 064603 (2003).

[8] S. Dieterich *et al.*, Phys. Lett. B **500,** 47 (2001).

[9] S. Strauch *et al.*, Phys. Rev. Lett. **91,** 052301 (2003).

[10] S. Boffi, C. Giusti, and F. Pacati, Phys. Rep. **226,** 1 (1993).

[11] J. Kelly, Adv. Nucl. Phys. **23,** 75 (1996).

[12] A. Picklesimer, J. Van Orden, and S. Wallace, Phys. Rev. C **32,** 1312 (1985).

[13] Y. Yin, D. Onley, and L. Wright, Phys. Rev. C **45,** 1311 (1992).

[14] J. Johansson, H. Sherif, and G. Lotz, Nucl. Phys. A **605,** 517 (1996).

[15] J. Udias, P. Sarriguren, E. Moya de Guerra, E. Garrido, and J. Caballero, Phys. Rev. C **48,** 2731 (1993).

[16] A. Meucci, C. Giusti, and F. Pacati, Phys. Rev. C **64,** 64014605 (2000).

[17] B. Serot and J. Walecka, Adv. Nucl. Phys. **16,** 1 (1986).

[18] R. Glauber and G. Matthiae, Nucl. Phys. B **21,** 135 (1970).

[19] D. Yennie, *Hadronic Interactions of Electrons and Photons* (J. Cummings and D. Osborn (Eds) Academic Press, New York, 1971), p. 321.

[20] E. Moniz and G. Nixon, Ann. Phys. **67,** 58 (1971).

[21] C. C. degli Atti, L. Kaptari, and D. Treleani, Phys. Rev. C **63,** 044601 (2001).

[22] S. Jeschonnek and T. Donnelly, Phys. Rev. C **59,** 2676 (1999).

[23] O. Benhar, N. Nikolaev, J. Speth, A. Usmani, and B. Zakharov, Nucl. Phys. A **673,** 241 (2000).

[24] A. Kohama, K. Yazaki, and R. Seki, Nucl. Phys. A **662,** 175 (2000).

[25] L. Frankfurt, E. Moniz, M. Sargsyan, and M. Strikman, Phys. Rev. C **51,** 3435 (1995).

[26] N. Nikolaev, A. Szcurek, J. Speth, J. Wambach, B. Zakharov, and V. Zoller, Nucl. Phys. A **582,** 665 (1995).

[27] M. Petraki, E. Mavrommatis, O. Benhar, J. Clark, A. Fabrocini, and S. Fantoni, Phys. Rev. C **67,** 014605 (2003).

[28] The Super-Kamiokande Collaboration, Phys. Rev. Lett. **81,** 1562 (1998).

[29] S. Freedman and B. Kayser, physics/0411216 .

[30] Minerνa Collaboration , "http://www.pas.rochester.edu/ ksmcf/minerva,".

[31] J. Bahcall, A. Serenelli, and S. Basu, Astrophys. J. **621,** L85 (2005).

[32] A. Aprahamian, K. Langanke, and M. Wiescher, Prog. Part. Nucl. Phys. **54,** 535 (2005).

[33] Finesse, "http://www-finesse.fnal.gov/,".

[34] D. Ravenhall and R. Mercer, Phys. Rev. C **13,** 2324 (1976).

[35] S. Tuan, L. Wright, and D. Onley, Nucl. Instrum. Meth. **60,** 70 (1968).

[36] R. Mercer, Phys. Rev. C **15,** 1786 (1977).

[37] L. Cardman, D. Dowell, R. Gulbranson, D. Ravenhall, and R. Mercer, Phys. Rev. C **18,** 1388 (1978).

[38] J. Heisenberg, Adv. Nucl. Phys. **12,** 61 (1981).

[39] J. Arrington, Phys. Rev. C **69,** 032201 (2004).

[40] V. Van der Sluys, K. Heyde, J. Ryckebusch, and M. Waroquier, Phys. Rev. C **55,** 1982 (1997).

[41] T. Donnelly and A. Raskin, Ann. Phys. **169,** 247 (1986).

[42] A. Raskin and T. Donnelly, Ann. Phys. **191,** 78 (1989).

[43] J. Bjorken and S. Drell, *Relativistic Quantum Mechanics* (Mc-Graw-Hill, New York, 1964).

[44] W. Kleppinger and J. Walecka, Ann. Phys. **146,** 349 (1983).

[45] S. Malov *et al.*, Phys. Rev. C **62,** 057302 (2000).

[46] A. Picklesimer and J. Van Orden, Phys. Rev. C **35,** 266 (1987).

[47] A. Picklesimer and J. Van Orden, Phys. Rev. C **40,** 290 (1989).

[48] T. de Forest, Nucl. Phys. A **392,** 232 (1983).

[49] S. Pollock, H. Naus, and J. Koch, Phys. Rev. C **53,** 2304 (1996).

[50] J. Kelly, Phys. Rev. C **56,** 2672 (1997).

[51] S. Galster *et al.*, Nucl. Phys. B **32,** 221 (1971).

[52] M. Jones *et al.*, Phys. Rev. Lett. **84,** 1398 (2000).

[53] O. Gayou *et al.*, Phys. Rev. Lett. **88,** 092301 (2002).

[54] H. Budd, A. Bodek, and J. Arrington, hep-ex/0308005 .

[55] J. Arrington, Phys. Rev. C **69,** 022201(R) (2004).

[56] P. Guichon and M. Vanderhaeghen, Phys. Rev. Lett. **91,** 142303 (2003).

[57] P. Blunden, W. Melnitchouk, and J. Tjon, Phys. Rev. Lett. **91,** 142304 (2003).

[58] J. Walecka, Ann. Phys. **83,** 491 (1974).

[59] C. Horowitz and B. Serot, Nucl. Phys. A **368,** 503 (1981).

[60] B. Serot, Phys. Lett. B **86,** 146 (1979).

[61] R. Furnstahl, H.-B. Tang, and B. Serot, Phys. Rev. C **52,** 1368 (1996).

[62] R. Furnstahl, B. Serot, and H.-B. Tang, Nucl. Phys. A **615,** 441 (1997).

[63] L. Miller and A. Green, Phys. Rev. C **5,** 241 (1971).

[64] J. Walecka, *Electron Scattering for Nuclear and Nucleon Structure* (Cambridge University Press, Cambridge, 2001).

[65] R. Frosch, J. McCarthy, R. Rand, and M. Yearian, Phys. Rev. **160,** 874 (1967).

[66] J. McCarthy, I. Sick, , and R. Whitney, Phys. Rev. C **15,** 1396 (1977).

[67] J. Carlson and R. Schiavilla, Rev. Mod. Phys. **70,** 743 (1998).

[68] D. Debruyne, J. Ryckebusch, W. Van Nespen, and S. Janssen, Phys. Rev. C **62,** 024611 (2000).

[69] J. Ryckebusch, D. Debruyne, P. Lava, S. Janssen, B. Van Overmeire, and T. Van Cauteren, Nucl. Phys. A **728,** 226 (2003).

[70] E. Cooper, S. Hama, B. Clarck, and R. Mercer, Phys. Rev. C **47,** 297 (1993).

[71] R. Amado, J. Piekarewicz, D. Sparrow, and J. McNeil, Phys. Rev. C **28,** 1663 (1983).

[72] W. Greenberg and G. Miller, Phys. Rev. C **49,** 2747 (1994).

[73] H. Ito, S. Koonin, and R. Seki, Phys. Rev. C **56,** 3231 (1997).

[74] R. J. Glauber, In *Lectures in Theoretical Physics*, W. Brittin and L. Bunhamm, eds., (Interscience, New York, 1959).

[75] A. Bianconi and M. Radici, Phys. Lett. B **363,** 24 (1995).

[76] A. Bianconi and M. Radici, Phys. Rev. C **54,** 3117 (1996).

[77] G. Alkhazov, S. Belostotsky, and A. Voroboyov, Phys. Rep. **42,** 89 (1978).

[78] F. Bauer *et al.*, Phys. Rev. Lett. **90,** 142301 (2003).

[79] K. Eyser, R. Machleidt, W. Scobel, and the EDDA Collaboration, Eur. Phys. J. A **22,** 105 (2004).

[80] S. Wallace, Adv. Nucl. Phys. **12,** 135 (1981).

[81] S. Jeschonnek and T. Donnelly, Phys. Rev. C **59,** 2676 (1998).

[82] R. Schiavilla, O. Benhar, A. Kievsky, L. Marcucci, and M. Viviani, Phys. Rev. C **72,** 064003 (2005).

[83] H. Frauenfelder and E. Henley, *Subatomic Physics second edition* (Prentice-Hall, New Jersey, 1991).

[84] K. Varga, S. Pieper, Y. Suzuki, and R. Wiringa, Phys. Rev. C **66,** 034611 (2002).

[85] P. D. Group, "http://pdg.lbl.gov,".

[86] B. Silverman *et al.*, Nucl. Phys. A **499,** 763 (1989).

[87] A. Dobrovolsky *et al.*, Nucl. Phys. B **214,** 1 (1983).

[88] H. Morita, C. C. degli Atti, and D. Treleani, Phys. Rev. C **60,** 034603 (1999).

[89] J. Udias and J. Vignote, Phys. Rev. C **62,** 034302 (2000).

[90] M. Martinez, J. Caballero, and T. Donnelly, Nucl. Phys. A **707,** 83 (2002).

[91] A. Mueller, In *Proceedings of the XVII Rencontre de Moriond*, J. T. T. Van, ed., p. 13 (Editions Fronti, Gif-sur-Yvette, 1982).

[92] S. Brodsky, In *Proceedings of the XIII International Symposium on Multiparticle Dynamics*, W. Kittel, W. Metzger, and A. Stergiou, eds., p. 963 (World Scientific, Singapore, 1982).

[93] G. Garino *et al.*, Phys. Rev. C **45,** 780 (1992).

[94] T. O'Neill *et al.*, Phys. Lett. B **351,** 87 (1995).

[95] N. Makins *et al.*, Phys. Rev. Lett. **72,** 1986 (1994).

[96] K. Garrow *et al.*, Phys. Rev. C **66,** 044613 (2002).

[97] D. Abbott *et al.*, Phys. Rev. Lett. **80,** 5072 (1998).

[98] D. Rohe *et al.*, Phys. Rev. C **72,** 054602 (2005).

[99] S. Frankel, W. Frati, and N. Walet, Nucl. Phys. A **580,** 595 (1994).

[100] N. Nikolaev, A. Szcurek, J. Speth, J. Wambach, B. Zakharov, and V. Zoller, Phys. Rev. C **50,** R1296 (1994).

[101] Y. Golubeva, L. Kondratyuk, A. Bianconi, S. Boffi, and M. Radici, Phys. Rev. C **57,** 2618 (1998).

[102] L. Frankfurt, M. Strikman, and M. Zhalov, Phys. Rev. C. **50,** 2189 (1994).

[103] L. Frankfurt, M. Strikman, and M. Zhalov, Phys. Lett. B **503,** 73 (2001).

[104] V. Pandharipande and S. Pieper, Phys. Rev. C **45,** 791 (1992).

[105] A. Kohama, K. Yazaki, and R. Seki, Nucl. Phys. A **551,** 687 (1993).

[106] J. Kelly, Phys. Rev. C **54,** 2547 (1996).

[107] A. Meucci, Phys. Rev. C **65,** 044601 (2002).

[108] J. Udias, P. Sarriguren, E. Moya de Guerra, E. Garrido, and J. Caballero, Phys. Rev. C **51,** 3246 (1995).

[109] J. Udias, J. Caballero, E. Moya de Guerra, J. Amaro, and T. Donnelly, Phys. Rev. Lett. **83,** 5451 (1999).

[110] J. Udias, J. Caballero, E. Moya de Guerra, J. R. Vignote, and A. Escuderos, Phys. Rev. C **64,** 024614 (2001).

[111] J. Caballero, T. Donnelly, E. M. de Guerra, and J. Udias, Nucl. Phys. A **632,** 323 (1998).

[112] J. Ryckebusch, Phys. Rev. C **64,** 044606 (2001).

[113] J. Amaro, M. Barbaro, J. Caballero, and F. K. Tabatabaei, Phys. Rev. C **68,** 014604 (2003).

[114] L. Frankfurt and M. Strikman, Phys. Rep. **76,** 215 (1981).

[115] L. Frankfurt and M. Strikman, Prog. Part. Nucl. Phys. **27,** 135 (1991).

[116] L. Frankfurt, G. Miller, and M. Strikman, Annu. Rev. Nucl. Part. Sci. **45,** 501 (1994).

[117] G. Farrar *et al.*, Phys. Rev. Lett. **61,** 686 (1988).

[118] B. Kundu *et al.*, Phys. Rev. D **62,** 113009 (2000).

[119] J. Smith and G. Miller, Phys. Rev. Lett. **91,** 212301 (2003).

[120] J. Carlson, J. Jourdan, R. Schiavilla, and I. Sick, Phys. Lett. B **553,** 191 (2003).

[121] J. Morgenstern and Z.-E. Meziani, Eur. Phys. J. A **17,** 451 (2003).

[122] I. Sick, Phys. Lett. B **157,** 13 (1985).

[123] E. Henley and G. Krein, Phys. Lett. B **231,** 213 (1989).

[124] G. van der Steenhoven *et al.*, Phys. Rev. Lett. **57,** 182 (1986).

[125] D. Reffay-Pikeroen *et al.*, Phys. Rev. Lett. **60,** 776 (1988).

[126] J. Ryckebusch, K. Heyde, D. Van Neck, and M. Waroquier, Phys. Lett. B **222,** 183 (1989).

[127] M. Buballa, S. Drozdz, S. Krewald, and A. Szczurek, Phys. Rev. C **44,** 810 (1991).

[128] T. Warmann and K. Langanke, Phys. Lett. B **273,** 193 (1991).

[129] J. Ducret *et al.*, Nucl. Phys. A **556,** 373 (1993).

[130] R. Arnold, C. Carlson, and F. Gross, Phys. Rev. C **23,** 363 (1981).

[131] J.-M. Laget, Nucl. Phys. A **579,** 333 (1994).

[132] J. Kelly, Phys. Rev. C **59,** 3256 (1999).

[133] J. Kelly, Phys. Rev. C **60,** 044609 (1999).

[134] J. Ryckebusch, D. Debruyne, W. Van Nespen, and S. Janssen, Phys. Rev. C **60,** 034604 (1999).

[135] A. Meucci, C. Giusti, and F. Pacati, Phys. Rev. C **64,** 014604 (2001).

[136] M. Radici, A. Meucci, and W. Dickhoff, Eur. Phys. J. A **17,** 65 (2003).

[137] F. Tabatabaei, J. Amaro, and J. Caballero, Phys. Rev. C **68,** 034611 (2003).

[138] M. Martinez, J. Vignote, J. Caballero, T. Donnelly, E. Moya de Guerra, and J. Udias, Phys. Rev. C **69,** 034604 (2004).

[139] P. Guichon, Phys. Lett. B **200,** 235 (1988).

[140] D. Lu, A. Thomas, K. Tsushima, A. Williams, and K. Saito, Phys. Lett. B **417,** 217 (1998).

[141] D. Lu, K. Tsushima, A. Thomas, A. Williams, and K. Saito, Phys. Rev. C **60,** 068201 (1999).

[142] C. Christov, A. Gorski, K. Goeke, and P. Pobylitsa, Nucl. Phys. A **592,** 513 (1995).

[143] J. Smith and G. Miller, Phys. Rev. C **70,** 065205 (2005).

[144] U. Yakhshiev, M. Musakhanov, A. Rakhimov, U.-G. Meißner, and A. Wirzba, Nuc. Phys. A **700,** 403 (2002).

[145] U. Yakhshiev, U.-G. Meißner, and A. Wirzba, Eur. Phys. J. A **16,** 569 (2003).

[146] L. Celenza, A. Rosenthal, and C. Shakin, Phys. Rev. C **31,** 232 (1985).

[147] I. Cheon and M. Jeong, J. Phys. Soc. Jpn. **61,** 2726 (1992).

[148] M. Frank, B. Jennings, and G. Miller, Phys. Rev. C **54,** 920 (1996).

[149] D. Alde *et al.*, Phys. Rev. Lett. **64,** 2479 (1990).

[150] D. Lu, A. Thomas, and A. Williams, Phys. Rev. C **57,** 2628 (1998).

[151] C. Gearheart, Ph.D. thesis, Washington University, St. Louis, 1994.

[152] J. Ryckebusch and W. Van Nespen, Eur. Phys. J. A **20,** 435 (2004).

[153] P. Ulmer, "MCEEP , Monte Carlo for Electro-Nuclear Coincidence Experiments, Program Version 3.4," (2000).

[154] M. Martinez, Private communication.

[155] R. Schiavilla, O. Benhar, A. Kievsky, L. Marcucci, and M.Viviani, Phys. Rev. Lett. **94,** 072303 (2005).

[156] Jefferson Lab Experiment E03-104, Probing the Limits of the Standard Model of Nuclear Physics with ^{4}He$(\vec{e}, e'\vec{p})^3$H Reaction, R. Ent, R. Ransome, S. Strauch, and P.E. Ulmer, spokespeople.

[157] R. Woo *et al.*, Phys. Rev. Lett. **80,** 456 (1998).

[158] S. Gardner and J. Piekarewicz, Phys. Rev. C **50,** 2822 (1994).

[159] S. Jeschonnek and T. Donnelly, Phys. Rev. C **57,** 2438 (1998).

[160] J. Vignote, M. Martinez, J. Caballero, E. Moya de Guerra, and J. Udias, Phys. Rev. C **70,** 044608 (2004).

[161] K. Fissum *et al.*, Phys. Rev. C **70,** 034606 (2004).

[162] J. Kelly, Phys. Rev. C **72,** 014602 (2005).

[163] C. Horowitz, H. Kim, P. Murdock, and S. Pollock, Phys. Rev. C **48,** 3078 (1993).

[164] Y. Umino and J. Udias, Phys. Rev. C **52,** 3399 (1995).

[165] Y. Umino, J. Udias, and P. Mulders, Phys. Rev. Lett. **74,** 4993 (1995).

[166] N. Jachowicz, K. Vantournhout, J. Ryckebusch, and K. Heyde, Phys. Rev. Lett. **93,** 082501 (2004).

[167] N. Jachowicz, K. Vantournhout, J. Ryckebusch, and K. Heyde, Phys. Rev. C **71,** 034604 (2005).

[168] W. Alberico *et al.*, Nucl. Phys. A **623,** 471 (1997).

[169] W. Alberico *et al.*, Phys. Lett. B **438,** 9 (1998).

[170] C. Maieron, M. Martínez, J. Caballero, and J. Udías, Phys. Rev. C **68,** 048501 (2003).

[171] A. Meucci, C. Giusti, and F. Pacati, Nucl. Phys. A **744,** 307 (2004).

[172] A. Meucci, C. Giusti, and F. Pacati, Nucl. Phys. A **739,** 277 (2004).

[173] B. van der Ventel and J. Piekarewicz, Phys. Rev. C **69,** 035501 (2004).

[174] M. Barbaro, A. De pace, T. Donnelly, A. Molinari, and M. Musolf, Phys. Rev. C **54,** 1954 (1996).

[175] C. Bleve, G. Co, I. De Mitri, P. Bernardini, G. Mancarella, D. Martello, and A. Surdo, Astropart. Phys. **16,** 145 (2001).

[176] H. Kim, J. Piekarewicz, and C. Horowitz, Phys. Rev. C **51,** 2739 (1995).

[177] H. Kim, S. Schramm, and C. Horowitz, Phys. Rev. C **53,** 2468 (1996).

[178] H. Kim, S. Schramm, and C. Horowitz, Phys. Rev. C **53,** 3131 (1996).

[179] T. Leitner, N. Alvarez-Russo, and U. Mosel, nucl-th/0511058 (2005).

[180] N. Alvarez-Russo, T. Leitner, and U. Mosel, nucl-th/0601021 (2006).

[181] J. Nieves, J. Amaro, and M. Valverde, Phys. Rev. C **70,** 055503 (2004).

[182] J. Amaro, M. Barbaro, J. Caballero, T. Donnelly, A.Molinari, and I. Sick, Phys. Rev. C **71,** 015501 (2005).

[183] Boone, "http://www-boone.fnal.gov/,".

[184] M. Martinez, P. Lava, N. Jachowicz, J. Ryckebusch, K. Vantournhout, and J. Udias, Phys. Rev. C **73,** 024607 (2006).

[185] P. Lava, N. Jachowicz, M. Martinez, and J. Ryckebusch, nucl-th/0509103 (2005).

[186] L. Ahrens *et al.*, Phys. Rev. D **35,** 785 (1987).

[187] O. Lalakulich and E. Paschos, Phys. Rev. D **71,** 074003 (2005).

[188] B. van der Ventel and J. Piekarewicz, Phys. Rev. C **73,** 025501 (2006).

[189] A. Meucci, C. Giusti, and F. Pacati, nucl-th/0601052 (2006).

[190] P. Lava, M. Martínez, J. Ryckebusch, J. Caballero, and J. Udías, Phys. Lett. B **595,** 177 (2004).

[191] S. Barish *et al.*, Phys. Rev. D **16,** 3103 (1977).

[192] N. Baker *et al.*, Phys. Rev. D **23,** 2499 (1977).

[193] W. Mann *et al.*, Phys. Rev. Lett. **31,** 844 (1973).

[194] J. Brunner *et al.*, Z. Phys. C **45,** 551 (1990).

[195] M. Pohl *et al.*, Lett. Nuovo Cim. **26,** 332 (1979).

[196] L. Auerbach *et al.*, Phys. Rev. C **66,** 015501 (2002).

[197] S. Belikov *et al.*, Z. Phys. A **320,** 625 (1985).

[198] S. Bonetti *et al.*, Nuovo Cimento A **38,** 260 (1977).

[199] B. Mueller *et al.*, Phys. Rev. Lett. **78,** 3824 (1997).

[200] D. Spayde, Phys. Lett. B **583,** 79 (2004).

[201] K. Aniol *et al.*, Phys. Rev. Lett. **82,** 1096 (1999).

[202] K. Aniol *et al.*, Phys. Rev. C **69,** 065501 (2004).

[203] K. Aniol *et al.*, Phys. Rev. Lett. **96,** 022003 (2006).

[204] D. Armstrong *et al.*, Phys. Rev. Lett. **95,** 092001 (2005).

[205] F. Maas *et al.*, Phys. Rev. Lett. **93,** 022002 (2004).

[206] F. Maas *et al.*, Phys. Rev. Lett. **94,** 152001 (2005).

[207] P. Anthony *et al.*, Phys. Rev. Lett. **92,** 181602 (2004).

[208] J. Ashman *et al.*, Nucl. Phys. B **328,** 1 (1989).

[209] B. Adeva *et al.*, Phys. Rev. D **58,** 112002 (1998).

[210] P. Anthony *et al.*, Phys. Lett. B **493,** 19 (2000).

[211] A. Airapetian *et al.*, Phys. Rev. Lett. **92,** 012005 (2004).

[212] R. Jaffe, Phys. Lett. B **229,** 275 (1989).

[213] M. Ramsey-Musolf and M. Burkardt, Z. Phys. C **61,** 433 (1994).

[214] W. Koepf, S. Pollock, and E. Henley, Phys. Lett. B **288,** 11 (1992).

[215] T. Cohen, H. Forkel, and M. Nielsen, Phys. Lett. B **316,** 1 (1993).

[216] M. Ramsey-Musolf and H. Ito, Phys. Rev. C **55,** 3066 (1997).

[217] H. Weigel, A. Abada, R. Alkofer, and H. Reinhardt, Phys. Lett. B **353,** 20 (1995).

[218] N. Park, J. Schechter, and H. Weigel, Phys. Rev. D **43,** 869 (1991).

[219] M. Ramsey-Musolf, H.-W. Hammer, and D. Drechsel, Phys. Rev. D **55,** 2741 (1997).

[220] A. Silva, H. Kim, and K. Goeke, Phys. Rev. D **65,** 014016 (2001).

[221] M. Ramsey-Musolf, nucl-th/0501023 .

[222] W. Alberico, S. Bilenky, and C. Maieron, Phys. Rept. **358,** 227 (2002).

[223] W. Alberico, M. Barbaro, S. Bilenky, J. Caballero, C. Giunti, C. Maieron, E. Moya de Guerra, and J. Udias, Nucl. Phys. A **651,** 277 (1999).

[224] G. Garvey, E. Kolbe, K. Langanke, and S. Krewald, Phys. Rev. C **48,** 1919 (1993).

[225] S. Pate, Eur. Phys. J. A **24S2,** 67 (2005).

[226] W. Alberico, S. Bilenky, C. Giunti, and C. Maieron, Z. Phys. C **70,** 463 (1996).

[227] H. Forkel, Phys. Rev. C **56,** 510 (1997).

[228] S. Pate, private communication .

Nederlandstalige Samenvatting

1 Inleiding

De voorbije eeuw mocht de geboorte en de ongelooflijke evolutie van kern- en deeltjesfysica aanschouwen, startend bij de ontdekking van de kern tot de erkenning van kwantumchromodynamica (QCD) als de fundamentele theorie van de sterke interactie. Maar wat maakt kernfysica nu precies interessant? De kern is samengesteld uit verschillende baryonen (protonen en neutronen) en levert ons een uniek microscopisch kader om de structuur van de fundamentele interacties te onderzoeken. Tevens is het gros van de massa en de energie in het universum afkomstig van kernen en nucleaire reacties. Bijgevolg is kernfysica van cruciaal belang als we het ontstaan van *alles* willen begrijpen.

Verstrooiingsprocessen aan kernen zijn van onschatbare waarde bij het aftasten van nucleaire systemen. Inderdaad, het *antwoord* van hadronische materie op externe projectielen levert dé sleutel tot een grondige kennis van de kernstructuur en -dynamica. Hadronische projectielen brengen de grootste werkzame doorsnedes met zich mee, maar verstoren de kernstructuur in grote mate. Leptonen daarentegen vragen een grotere experimentele inspanning, maar kunnen dankzij hun relatief zwakke interactie het ganse nucleaire volume aftasten. Doorheen dit werk concentreren we ons hoofdzakelijk op elektromagnetische en zwakke interacties in de quasi-elastische regio. In dit gebied verwacht men dat het leptonisch projectiel de quasi-elastische uitstoot van één enkel nucleon veroorzaakt.

2 Elektromagnetische interacties

In het verleden werden quasi-elastische elektromagnetische verstrooiingsprocessen vooral aangewend om het schillenmodel experimenteel te verifiëren. Exclusieve $A(e, e'p)$ reacties, waarbij de restkern achtergelaten wordt in het discrete deel van zijn energiespectrum, onthulden dat de impulsdistributies van gebonden laag-energetische protonen overeenstemmen met de voorspellingen van de gemiddeld-veldtheorie. De bezetting van de eendeeltjesniveaus viel echter heel wat kleiner uit dan kon verwacht worden op basis van een naïef gemiddeld-veldmodel. Dit leverde het onomstotelijk bewijs voor het bestaan van korte- en langedrachtscorrelaties.

De komst van continue-golf elektronenversnellers heeft de aandacht van exclusieve $A(e, e'p)$ metingen verschoven naar hogere energieën en andere doelstellingen. Zo werd de rol van relativiteit in kernen grondig onderzocht. Tevens zijn exclusieve processen van cruciaal belang in het bepalen van de overgang van hadronische naar partonische vrijheidsgraden. Hiertoe onderzoekt men of er aanwijzingen zijn voor het optreden van kleurtransparantie. Dit authentiek QCD-effect suggereert dat bij voldoende hoge energieën het aangestoten proton op een abnormaal zwakke manier zal interageren met de restkern. Een ander belangrijk onderwerp betreft de vraag of nucleonen vervormen wanneer ze ondergedompeld worden in een medium met een hoge hadronendichtheid. Op die manier kunnen $A(e, e'p)$ reacties hadronische structuurmodellen zwaar op de proef stellen.

2.1 Theoretische modellering

Het bekomen van fysische informatie impliceert de interpretatie van de data aan de hand van een zeker theoretisch kader. Vermits relativistische effecten van belang worden in het GeV energiegebied, leggen we er ons in dit werk op toe een relativistisch model aan te bieden voor de beschrijving van $A(e, e'p)$ reacties. Het modelleren van deze reacties is gekruid met drie ingrediënten:

- De elektromagnetische elektron-kern koppeling.
- De structuur van de kern.
- De interactie van het ejectiel met de nucleonen in de restkern.

De elektromagnetische koppeling, die gekarakteriseerd wordt door de fijnstructuurconstante $\alpha \approx 1/137$, is relatief zwak en geeft aanleiding tot een laagste orde behandeling van het probleem. Deze procedure staat algemeen bekend onder de noemer "één-foton-uitwisseling benadering". Vrij recente vormfactor resultaten van dubbele polarisatie experimenten duiden echter op het belang van hogere orde termen. Toch zullen we ons beperken tot eerste-orde termen, vermits deze procedure wijdverspreid is en leidt tot vrij makkelijk te interpreteren resultaten.

Tevens beschrijven we in dit werk de foton-kern koppeling in termen van de impuls benadering. Hierbij veronderstelt men dat de interactie gebeurt via de individuele nucleonen. De elektromagnetische koppeling met een gebonden (of "off-shell") nucleon is echter niet vrij van dubbelzinnigheden. De elektromagnetische vertices voor gebonden nucleonen hebben immers een complexere structuur dan voor vrije nucleonen. Dit staat bekend als de Gordon ambiguïteit. Een ander belangrijk probleem betreft de ijkinvariantie van de elektromagnetische stroom in veeldeeltjessystemen. Stroombehoud wordt a priori opgelegd door de longitudinale component van de stroom te elimineren ten voordele van de lading. Dit is de zogenaamde Coulombijk.

Voor het in kaart brengen van de kernstructuur beroepen we ons op het schillenmodel waar men veronderstelt dat de nucleonen onafhankelijk van elkaar bewegen in een gemiddeld-veldpotentiaal die de interacties met de omringende nucleonen in rekening brengt (onafhankelijk-deeltjesmodel). De initiële en finale A-nucleon golffuncties nemen hierbij de Slater-determinantvorm aan en zijn samengesteld uit de relativistische gebonden-toestand eendeeltjesgolffuncties, die bepaald worden via de Hartreebenadering van het $\sigma - \omega$ model.

Het resterende ingrediënt betreft de propagatie van het aangestoten nucleon door de kern en zijn interactie met de nucleonen in de restkern. Het includeren van nucleon-kern finale toestandsinteracties (FSI) kent reeds een grote geschiedenis in theoretische $A(e, e'p)$ reacties. Op dit moment is er echter nog steeds geen uniform en realistisch model waarin proton-kern FSI kunnen berekend worden voor proton kinetische energieën (T_p) gaande van lage energieën tot enkele GeV.

Voor kinetische energieën lager dan 1 GeV worden de meeste theoretische $A(e, e'p)$ studies verricht binnen de context van de (relativistische) verstoorde-golf impulsbenadering ((R)DWIA). Hier brengt men de FSI in rekening met behulp van proton-

kern optische potentialen. Parametrisaties voor deze optische potentialen steunen op empirische gegevens van elastische proton-kern verstrooiingsprocessen. Bij hogere energieën wordt de beschrijving van FSI in een (R)DWIA model problematisch omwille van drie redenen. Eerst en vooral streven de (R)DWIA berekeningen exacte oplossingen van de Diracvergelijking na met behulp van partiële-golfexpansies. Deze techniek wordt echter uitermate onpraktisch bij hoge energieën vermits het aantal partiële golven, die nodig zijn om convergentie te bereiken, steeds groter wordt. Uiteindelijk verliest men de controle over de numerieke stabiliteit. Ten tweede zijn optische potentialen gewoonlijk niet beschikbaar voor proton kinetische energieën groter dan 1 GeV. Ten laatste lijkt bij hoge energieën het optisch potentiaalmodel onnatuurlijk voor de modellering van FSI wegens het sterk inelastisch, absorberend en diffractief karakter van de onderliggende elementaire nucleon-nucleon interactie.

Het eerste probleem kan deels opgelost worden met behulp van de eikonale benadering (EA). Deze benadering vindt zijn oorsprong in optica en behoort tot de groep van semi-klassieke benaderingen die nuttig worden wanneer de de Broglie-golflengte van het invallend deeltje voldoende kort is in vergelijking met de afstand waarover de potentiaal varieert. Tevens veronderstelt men dat de sterkte van de potentiaal veel kleiner is dan de energie van het invallend deeltje. De eikonale benadering is ook nog gekend onder de noemer "kleine-hoek benadering" vermits men verwacht dat ze accuraat is voor kleine-hoek verstrooiingen, of equivalent hiermee wanneer de grootte van de impulstransfer $|\vec{q}|$ voldoende groot is in vergelijking met het "missing momentum" van het ejectiel. De $A(e, e'p)$ - berekeningen bekomen aan de hand van optische potentialen en de eikonale benadering, bestempelen we als ROMEA resultaten.

Voor problemen twee en drie levert de Glauber veelvuldige-verstrooiingstheorie een waardig en economisch alternatief. Deze theorie is een veeldeeltjesveralgemening van de eikonale benadering. In een Glaubermodel wordt de link met de fundamentele nucleon-nucleon processen hersteld via de introductie van een profielfunctie. Deze wordt volledig bepaald door empirische gegevens van elementaire proton-proton en proton-neutron verstrooingsprocessen. Glaubertheorie postuleert lineaire banen en bevroren toeschouwersnucleonen. Wij presenteren in dit werk een relativische versie van de Glauber veelvuldige-verstrooiingstheorie

(RMSGA). In ons model worden enkel centrale FSI in rekening gebracht, vermits de elastische verstrooiing van protonen met impuls groter dan 1 GeV wordt gedomineerd door de centrale, spin-onafhakelijke amplitude. Hierdoor levert de schaling van een vlakke golf met de *Dirac-Glauber fase* alle FSI effecten in het RMSGA formalisme.

2.2 Resultaten

Eén van de hoofddoelen van deze thesis bestaat erin de onderliggende benaderingen in de ROMEA en RMSGA modellen grondig te testen. Dit zal gebeuren aan de hand van een uitvoerige vergelijking met de resultaten van een onafhankelijk RDWIA model, geïmplementeerd door de Madrid-Sevilla groep. Om de vergelijking zo consistent mogelijk te maken, veronderstellen we identieke parametrisaties voor de relativistische gebonden-toestand golffuncties, de stroomoperator en de ijk. Enkel de manier waarop de drie modellen FSI beschrijven, verschilt. Tevens confronteren we onze berekeningen met experimentele resultaten. Hiertoe bestuderen we verschillende onderwerpen die tegenwoordig relevant zijn in $A(e,e'p)$ intermediaire energiefysica.

Nucleaire transparanties in $A(e,e'p)$ reacties

In hoofdstuk 3 bestuderen we de nucleaire transparantie in $A(e,e'p)$ reacties. De nucleaire transparantie is een maat voor de kans dat een nucleon, met een zekere energie, "vrij" kan ontsnappen uit de kern en is uitermate geschikt in de zoektocht naar het kleurtransparantiefenomeen. De voorspelling van de nucleaire transparantie tot protonen stelt theoretische $A(e,e'p)$ -modellen voor een grote uitdaging omwille van de brede waaier van proton energieën in de huidige experimenten.

In het "lage energiegebied", d.w.z. voor $T_p <= 1$ GeV, willen we eerst de eikonale benadering testen. Hiertoe vergelijken we de voorspellingen van de ROMEA code met die van het RDWIA formalisme. We vinden dat de ROMEA en RDWIA berekeningen bijna identiek zijn voor zowel ^{12}C als ^{208}Pb. Heel merkwaardig is dat dit ook geldt voor de laagste energieën, waar men het gebruik van de eikonale benadering in vraag kan stellen. Dit laat ons toe voldoende vertrouwen te stellen in de eikonale benadering wat betreft nucleaire transparanties, en bijgevolg kunnen we ons oog richten op een confronterende studie van "nucleon-kern" (RDWIA) en

"nucleon-nucleon" (RMSGA) modellen. We bestuderen zowel de energie- als de A-afhankelijkheid van de nucleaire transparantie. Beide modellen blijken de gemeten nucleaire transparanties lichtjes te onderschatten. In het overlappend energiegebied, waar beide modellen toepasbaar zijn, stemmen alle RDWIA- en RMSGA-resultaten opmerkelijk overeen, zelfs wanneer we naar de bijdragen van de verschillende eendeeltjesniveaus kijken. Dit laat ons toe te concluderen dat men op een veilige manier het "lage" en het "hoge energiegebied" kan overbruggen.

Observabelen in $A(\vec{e}, e'\vec{p})$ reacties

Wat betreft nucleaire transparanties geven de ROMEA, RMSGA en RDWIA modellen dus vergelijkbare resultaten. Maar transparanties zijn geïntegreerde (of inclusieve) grootheden en kunnen sommige subtiliteiten in het behandelen van FSI verbergen. In hoofdstuk 4 leggen we ons expliciet toe op puur exclusieve grootheden. We vergelijken de voorspellingen van de verschillende modellen met dubbel gepolariseerde $A(\vec{e}, e'\vec{p})$ data die verzameld zijn in een waaier van elektronenverstrooiingsfaciliteiten.

De getransfereerde polarisatiecomponenten P'_l en P'_t werd de laatste jaren veel aandacht toebedeeld. De verhouding P'_l/P'_t staat immers in direct verband met de verhouding van de elektrische tot de magnetische vormfactor. Deze betrekking geldt echter enkel voor verstrooiing aan vrije nucleonen in de vlakke golflimiet. Wanneer het nucleon gebonden is, kunnen afwijkingen in deze betrekking dan ook wijzen op een wijziging van zijn elektromagnetische eigenschappen. Recent verschenen $(\vec{e}, e'\vec{p})$ meetresultaten voor de trefkernen ^{16}O en ^{4}He. Deze vergelijken we met de voorspellingen van het RMSGA model. Om zo nauw mogelijk bij het experiment aan te sluiten worden de antwoordfuncties van de RMSGA berekeningen via een Monte-Carlo simulatie verwerkt. We doen zowel berekeningen met vrije als met *medium-gemodificeerde* vormfactoren. Wat de laatste betreft, gebruiken we de parameters van o.a. het quark-meson koppelingsmodel (QMC) en van het chiraal-quark soliton model (CQS). De scalaire en vectorvelden, die in kwantumhadrodynamica de krachten tussen nucleonen dragen, koppelen in deze modellen direct aan de quarks in het nucleon. Bijgevolg worden de intrinsieke eigenschappen van een gebonden nucleon beïnvloed door het medium. Het CQS model brengt,

in tegenstelling tot het QMC model, ook bijdragen van de zee in rekening. De mediummodificaties zijn in beide hadron structuurmodellen van dezelfde grootteorde.

Onze voorspellingen volgen de trends van de eerder verschenen RDWIA resultaten. De ^{16}O data worden goed beschreven aan de hand van vrije elektromagnetische vormfactoren. Hetzelfde geldt voor ^{4}He bij de hoogste energieën. Voor ^{4}He en lagere energieën, lijkt de implementatie van QMC en CQS vormfactoren echter noodzakelijk voor een goede overeenkomst tussen theorie en experiment. Men hoopt dat nieuwe experimenten, met een betere statistiek, duidelijkheid zullen scheppen in dit controversieel probleem.

Terwijl de getransfereerde polarisatiecomponenten vooral bestudeerd worden met het oog op het waarnemen van mediummodificaties, treedt de geïnduceerde polarisatie component P_n voornamelijk op als scheidsrechter tussen verschillende modellen die FSI willen beschrijven. In de vlakke golflimiet is deze observabele immers identiek nul. Enkele jaren terug werden P_n-data gepubliceerd voor een ^{12}C trefkern. De energie in dit experiment is echter aan de lage kant. Toch worden de data heel goed beschreven door het ROMEA formalisme. Tevens tonen deze een grote overeenkomst met de resultaten van het RDWIA model. Dit illustreert dat de eikonale benadering opmerkelijk accuraat is, zelfs voor exclusieve grootheden en kinetische energieën van ongeveer 250 MeV. De RMSGA code voorspelt echter een bijzonder kleine P_n over de hele missing-momentum regio. Vermits de EA adequaat blijkt, moet de oorzaak van het falen van RMSGA elders gezocht worden. Het blijkt dat voornamelijk het ontbreken van spin-baaninteracties in RMSGA ons de das omdoet. Inderdaad, zoals hoger aangehaald, weerhouden we in ons Glauber model enkel centrale nucleon-nucleon interacties. Maar bovendien onthullen onze resultaten dat spineffecten uitdoven wanneer steeds hogere kinetische energieën bereikt worden. We kunnen dus concluderen dat het RMSGA model voor verbetering vatbaar is, althans voor de beschrijving van sommige polarisatie observabelen bij intermediaire energieën.

Een laatste punt van aandacht in exclusieve $A(e,e'p)$ reacties gaat naar de links-rechts asymmetrie A_{LT}. Vanuit theoretisch standpunt is dit een uitermate

interessante grootheid omdat men geen spectroscopische factoren moet invoeren. Bovendien blijkt deze observabele uiterst gevoelig te zijn voor veranderingen in de stroomoperator, dynamische en kinematische relativistische effecten, factorisatie-eigenschappen, ... Opnieuw geven onze ROMEA resultaten een bijzonder goede beschrijving van de data voor een ^{16}O trefkern en is de overeenkomst met RDWIA treffend. De RMSGA resultaten bevestigen ons vermoeden dat spineffecten in het onderliggend nucleon-nucleon proces moeten in rekening gebracht worden, al is hun bijdrage wel opvallend kleiner dan voor de geïnduceerde polarisatiecomponent. Tevens vinden we dat in de niet-relativistische vlakke golflimiet inderdaad factorisatie optreedt. Dit illustreert dat ons formalisme consistent is.

3 Zwakke interacties

De neutrale leden van de leptonfamilie worden neutrino's genoemd en werden in 1938 gepostuleerd door Pauli. In het standaardmodel worden neutrino's beschreven als massaloze, neutraal stabiele deeltjes en linkshandige velden. De massa van het neutrino blijft echter één van dé enigma's in de elementaire deeltjesfysica. Recente experimenten zoals SNO and SK hebben de wereld overtuigd dat neutrino's oscilleren tussen hun verschillende smaaktoestanden. Dit levert een onomstotelijk bewijs dat neutrino's wel een massa hebben en een verbetering van het standaardmodel zich opdringt.

In hadronen- en kernfysica staat het gebruik van neutrino projectielen nog in de kinderschoenen. Ondanks het feit dat neutrino's alomtegenwoordig zijn, drijven ze experimentatoren tot het uiterste vermits ze extreem zwak interageren. Met de komst van een hoge-intensiteit neutrinobundel in Fermilab dient zich echter een unieke gelegenheid aan om nieuwe informatie te winnen over de structuur van het nucleon en baryonresonanties. Experimenten zoals MINERνA en FINeSSE zullen zich wenden tot relevante problemen zoals de extractie van de elektrozwakke vormfactoren, de vreemde-quarkinhoud van het nucleon en neutrino-geïnduceerde pion-productie. Kernen zullen gebruikt worden als neutrino detectoren, vermits ze relatief grote werkzame doorsneden opleveren die een schat aan informatie bieden.

3.1 Theoretische modellering

Theoretische berekeningen zijn opnieuw onmisbaar bij het ontrafelen van informatie uit gemeten neutrino-kern interacties. Net als elektronen kunnen neutrino's gans de kern aftasten. Een belangrijk verschilpunt is echter dat neutrino's intrinsiek gepolariseerd zijn en interageren via de zwakke interactie. De drie basisingrediënten voor een theoretische modellering zijn echter identiek aan het $A(e, e'p)$ geval. In hoofdstuk 5 passen we ons RMSGA model aan om quasi-elastische inclusieve neutrino-kern interacties te beschrijven. Deze uitbreiding is vrij eenvoudig vermits de zwakke en de elektromagnetische interactie geünificeerd worden in het standaardmodel. Bovendien is in ons model de propagatie van het aangeschoten nucleon onafhankelijk van de aard van het leptonisch projectiel. Logischerwijs geldt dit ook voor de beschrijving van de kernstructuur.

3.2 Resultaten

Recent kwamen een aantal modellen op de markt om de FSI in quasi-elastische neutrino-kern interacties te beschrijven. In de vlakke golflimiet zouden deze modellen allen identieke resultaten moeten leveren. Toch was dit niet het geval. Een eerste doel is dan ook om de vlakke golflimiet van het RMSGA formalisme te vergelijken met die van het RDWIA model. De overeenkomst is treffend, en dit voor alle energieën en kernen. Meer nog, bij hogere energieën - waar bindingseffecten verwaarloosbaar zijn- reproduceren we de voorspellingen van twee onafhankelijke relativistische Fermi gas modellen. Dit geeft ons vertrouwen dat men onze vlakke golfresultaten als referentie-resultaten kan beschouwen.

Nu we zeker zijn over de vlakke golflimiet, kunnen we de effecten van FSI bekijken in de RDWIA en RMSGA modellen. Net zoals bij de $A(e, e'p)$ reactie levert het Glauber model al goed werk af vanaf $T_p \geq 250$ MeV. Vermits neutrino-kern berekeningen een inclusief karakter hebben, drijven zij de computerkracht echter tot het uiterste. Wij stellen een manier voor om FSI effecten in quasi-elastische neutrino-kern interacties af te schatten door het herschalen van de vlakke golfresultaten met een transparantiefactor bekomen uit $A(e, e'p)$ experimenten. In dit opzicht is de referentie vlakke golflimiet natuurlijk van cruciaal belang. Dit alles is natuurlijk enkel mogelijk in de veronderstelling dat de propagatie van het nucleon door de kern onafhankelijk is van de aard van het leptonische projectiel.

Nu we over een model beschikken om FSI te beschrijven in quasi-elastische neutrino-kern interacties, kunnen we ons buigen over meer exotische effecten. Pariteitsbrekende verstrooiingsprocessen kunnen immers specifieke eigenschappen van het nucleon onthullen die in pariteitsbehoudende processen verborgen blijven. Eén van hen betreft de mogelijke bijdrage van zee-quarks tot de spin, lading en magnetisch moment van het nucleon. We gebruiken de parameterisaties van verschillend hadron structuurmodellen om het effect van "vreemdheid" in rekening te brengen. We tonen aan dat de heliciteitsasymmetrie A_l ongevoelig is voor FSI en variaties in de stroomoperator, maar een manifeste gevoeligheid vertoont voor vreemdheidscontributies in de vector vormfactoren. Recent werd deze heliciteitsasymmetrie A_l naar voor geschoven als een mogelijke manier om het onderscheid te maken tussen neutrino's en anti-neutrino's.

4 Conclusies

We hebben een volledig ongefactoriseerd eikonaal kader gepresenteerd voor de modellering van quasi-elastische elektron- en neutrino-kern interacties. Ons model is flexibel daar het zowel gebruikt kan worden in combinatie met optische potentialen (ROMEA) of in een Glauber veelvuldige-verstrooiingsbenadering (RMSGA) om FSI te beschrijven. We hebben de onderliggende veronderstellingen uitvoerig getest door een vergelijking met de voorspellingen van het RDWIA formalisme geïmplementeerd door de Madrid-Sevilla groep. Tevens hebben we hierbij aandacht besteed aan verschillende discussiepunten in het huidige intermediaire energie-landschap. Vooral de eikonale benadering levert voortreffelijk werk en dit tot extreem lage kinetische energieën. Het RMSGA model is voor sommige observabelen nog voor verbetering vatbaar. In het bijzonder dient het includeren van spineffecten in de onderliggende nucleon-nucleon processen in de toekomst nader bekeken te worden.